

**PHYSICAL PROPERTIES OF MAGNETIC MACROMOLECULE-
METAL AND MACROMOLECULE-METAL OXIDE
NANOPARTICLE COMPLEXES**

Michael Andrew Zalich

Dissertation submitted to the faculty of the Virginia Polytechnic Institute and State
University in partial fulfillment of the requirements for the degree of

**Doctor of Philosophy
In
Chemistry**

Approved by:

Judy S. Riffle, Co-Chair
Timothy G. St. Pierre, Co-Chair
James E. McGrath
Richey M. Davis
Timothy E. Long

April 29, 2005
Blacksburg, Virginia

Keywords: cobalt, magnetite, nanoparticle, transmission electron microscopy, electron
diffraction, x-ray diffraction, SQUID, magnetic susceptometry

Copyright 2005, Michael A. Zalich

PHYSICAL PROPERTIES OF MAGNETIC MACROMOLECULE-METAL AND MACROMOLECULE-METAL OXIDE NANOPARTICLE COMPLEXES

Michael A. Zalich

ABSTRACT

Magnetic nanoparticles are of considerable interest owing to their potential applications in biotechnology and the magnetic recording industry. Iron oxides have received much attention owing to their oxidative stability and biocompatibility; however, other transition metals and their alloys are also under investigation. Cobalt has one of the largest magnetic susceptibilities of these materials, but it readily oxidizes upon exposure to air resulting in antiferromagnetic oxide. Hence, coating cobalt nanoparticles with an oxygen-impermeable sheath would confer numerous benefits. Cobalt nanoparticles were prepared by the thermolysis of dicobalt octacarbonyl in two block copolymer micellar systems, wherein the copolymers were precursors to graphite or silica. Subsequent heat treatment of the samples at 600-700°C was conducted to condense the polymer coating around the cobalt nanoparticles and form oxygen impervious graphite or silica sheaths.

Magnetic and structural characterization of these novel materials afforded pertinent information about their physical properties. Magnetic susceptometry indicated that the graphite coated cobalt nanoparticles resisted oxidation for over one year. The silica coated cobalt nanoparticles had high saturated specific magnetic moments, but the coatings were brittle and grinding the particles resulted in oxidation over time. Transmission electron microscopy (TEM), high-resolution TEM (HRTEM) and energy-filtered TEM (EFTEM) were employed to study particle size and structural differences of the cobalt nanoparticles before and after heat treatment. The mean particle size and size distribution increased for the graphite coated cobalt particles, due to particle sintering at 700°C. In the silica coated cobalt nanoparticle system, the mean particle size increased when the sample was heat-treated at 600°C leading to a bimodal distribution. This bimodal distribution was explained by a fraction of the particles sintering, while others remained discrete. When the silica system was heat treated at 700°C, the particle size and size distribution remained similar to those of the pre-heat-treated sample, indicating that no sintering had taken place. The rapid pyrolysis of the polymer at 700°C may serve to lock the cobalt nanoparticles into a silica matrix, thus preventing them from coming into contact with one another and sintering. Several diffraction techniques (selected area electron diffraction (SAD), nano-beam

electron diffraction (NBD) and x-ray diffraction (XRD)) were used to probe the crystal structure of graphite and silica coated cobalt nanoparticles, which was determined to be predominantly face-centered cubic.

Anisotropic magnetic nanoparticles (nanorods) have an increased magnetophoretic mobility over spherical magnetic nanoparticles with the same equatorial radius. This property makes them attractive candidates for *in vivo* biological applications. Anisotropic mixed ferrite nanoparticles were coated with a biocompatible hydrophilic block copolymer to render them dispersible in aqueous media. Polymer coated mixed ferrite particles exhibited magnetic properties similar to that of pure magnetite, as the total level of other transition metals in the nanoparticulate system was less than 5%. Electron energy loss spectroscopy (EELS) and (EFTEM) confirmed that the dominant elements in the mixed ferrite nanoparticles were iron and oxygen. Furthermore, HRTEM, SAD and XRD analyses indicated that the crystal structure for the mixed ferrite nanoparticles was inverse spinel. X-ray diffraction peaks at low angles for the coated mixed ferrite rods corresponded to poly(ethylene oxide) peaks, suggesting that the block copolymer employed as a dispersant was associated with the particles.

Acknowledgements

I would like to begin by expressing my deepest gratitude to my advisors, Dr. Judy Riffle (Virginia Tech) and Dr. Tim St. Pierre (The University of Western Australia), for their guidance and encouragement during my graduate career. I would also like to thank the members of my committee, Dr. James E. McGrath, Dr. Timothy E. Long, Dr. Richey M. Davis and Dr. Allan R. Shultz for their insight and support.

I would like to express my sincere appreciation to the Australian-American Fulbright Commission (Mark Darby, Judith Gamble, Melinda Hunt and Sandra Lambert) based in Canberra, Australia, the Fulbright selection committee and Barbara Cowles from the University Honors program at Virginia Tech for helping to make my experience in Australia possible. I would like to acknowledge and thank the past and present members of the Biophysics group at UWA (Wanida Chua-Anusorn, Eliza Bovell, Nicole Gorham, Heath Pardoe, Sara Hackett, Beau Pontre, Paul Clark, Adam Fleming, Jana Wittorff, Ralph James and Joan Connolly) for making me feel at home while in Perth for almost 2 years. In addition, I would like to thank Dr. Ian McArthur, Lydia Brazzale and Ede Lappel from the School of Physics at UWA for all of their administrative help and great conversations. Thanks to Dr. Rob Woodward and Dr. David Crew for educating (and entertaining) me during our magnetism discussions. Thanks also to the workshop crew at UWA (Dave, Craig, Steve, Gazza and Pete). Thanks to the Center for Microscopy and Microanalysis at UWA (Dr. Brendan Griffen, Steve Parry, John Murphy, Jeannette Hatch, Dr. Alexandra Suvorova and Dr. Peta Clode) for administrative help, educating me on microscopy and sample preparation techniques and ‘allowing’ me to do all of my microscopy in thongs. I express my gratitude to Dr. Martin Saunders from the Center for Microscopy and Microanalysis at UWA for taking me under his wing and teaching me everything that I know about transmission electron microscopy.

On the North American side, I would like to thank Linda Harris for putting up with me as a lab/office/house-mate at Virginia Tech and at UWA. We had some great times in both hemispheres. I would like to thank Jonathan Goff, Michael Vadala, Shane Thompson and Vince Baranauskas for their collaborative efforts while I was in Perth. Thanks to Angie Flynn for all of her help throughout the past five years. I would also like to thank my professors from Virginia Tech (Dr. Judy Riffle, Dr. James McGrath, Dr. Tim Long, Dr. James Tanko, Dr. Harry Gibson,

Dr. Brian Hanson, Dr. Harold McNair, Dr. William Ducker, Dr. Garth Wilkes and Dr. Felicia Etzkorn) for sharing their knowledge over the past few years.

I would like to thank my friends and colleagues from Virginia Tech (Matt and Stephanie Hunter, Jason Harmon, Jonathan Goff, Linda Harris, Kristen Wilson, Casey and Doug Elkins, Shauntrece Hardrict, Yin Lin, Shane Thompson, Jody Roberts and Alan Esker) for making graduate school an exciting and memorable experience. Thanks to the Canadians for their hospitality last summer and the multiple bbq's/parties, to Jason for the internet and burnin', to Jon for having the most far-out conversations regardless of location, to Linda for El Gelato, to Kristen for all of our conversations, to Casey (woo-woo) for the water battles and review sessions, to Doug for knowing so much about everything, to Yin Lin for his friendship and advice in lab, to Shane for playing pool, to Jody for throwing disc and to Alan for letting me stay at his house when I first visited VT.

I would like to thank my mates from Perth (Tim St. Pierre, Wanida Chua-Anusorn, Eliza Bovell, Peter Gibbons, Nicole Gorham, Jana Wittorff, Ralph James and Mel, Cara Weisbrod, Ben Corry, Nathan Harding, Helen Mortimer, Dermot Woods, Sam Dawkins, Milan Maric and Holly Rose) for all the good times we had while I was in Australia. I'll never forget Christmas at the beach, New Years Eve beach parties, random barbies...just because, Nando burgers (that didn't get taken from Eliza's mouth by a greedy Kookaburra), trips down south involving massive meat-pies and RISK, drinks at the UWA tavern, the Cott Hotel, the OBH and the Leftbank, watching rugby at the Albion, playing tennis at Cott and UWA, having the piss taken out of me on multiple occasions, watching and playing cricket, the beautiful sunsets and most importantly, the true friends that I made while living in Perth. I would like to thank my lifelong friend, Michael Sobota, for his unconditional friendship, motivational support and for being there when the seas were rough. I would also like to thank my friends Ryan Purvis, Case Donchez, Michael Oliver, Jim and Hailey Reddy, Autumn (Coleman) Purdy, Paul Kolesar, Chris Verardi, Beth Furar, Albrecht and Christa Stuber, Doris Mayer and Meghan Ritz for their support throughout the years.

Finally and most importantly, I would like to thank my parents John and Sandra Zalich, my younger brother Nicholas, my older brother John, sister-in-law Angela, my nieces Kayla, Lauren and Meghan, my grandmother Sue Cohen and all of my aunts and uncles for their love and support throughout my life and educational career.

List of Abbreviations

AFM	Antiferromagnet
AOT	Sodium bis(2-ethylhexyl) sulfosuccinate
Co	Cobalt
Co ₂ (CO) ₈	Dicobalt octacarbonyl
CoFe ₂ O ₄	Cobalt ferrite
CTAB	Cetyltrimethylammonium bromide
DCD	<i>dc</i> -demagnetization
DDAB	Didodecyldimethylammonium bromide
DLS	Dynamic light scattering
EDX	Energy dispersive x-ray spectroscopy
EELS	Electron energy loss spectroscopy
EFTEM	Energy-filtered transmission electron microscopy
ELNES	Energy loss near edge structure
EXELFS	Extended energy loss fine structure
FC	Field-cooled
fcc	face-centered cubic
Fe	Iron
Fe ₃ O ₄	Magnetite
γ-Fe ₂ O ₃	Maghemite
Fe(CO) ₅	Iron pentacarbonyl
FM	Ferromagnet
FTIR	Fourier transform infrared spectroscopy
GIF	Gatan image filter
hcp	hexagonal close packed
HRTEM	High-resolution transmission electron microscopy
IRM	Isothermal remanence magnetization
NBD	Nano-beam diffraction
NH ₄ OH	Ammonium hydroxide
OM	Optical microscopy
PAA	Poly(acrylic acid)

PCEMA	Poly(2-cinnamoylethylmethacrylate)
PCPMS	Poly((3-cyanopropyl)methylsiloxane)
PDMS	Poly(dimethylsiloxane)
PHI	Poly(2,3-dihydroxyisoprene)
PI	Poly(isoprene)
PMAA	Poly(methacrylic acid)
PMMA	Poly(methyl methacrylate)
PMTEOS	Poly(methyltriethoxysilethylsiloxane)
<i>Pt</i> BA	Poly(<i>tert</i> -butylacrylate)
PVA	Poly(vinyl alcohol)
SAD	Selected area diffraction
SAXS	Small angle x-ray scattering
SQUID	Superconducting QUantum Interference Device
TEM	Transmission electron microscopy
TOPO	Trioctylphosphine oxide
XRD	X-ray diffraction
ZFC	Zero field-cooled
χ	Magnetic susceptibility
H	Magnetic field strength
H_C	Coercivity
H_E	Exchange bias field
M	Mass magnetization
M_R	Remanent magnetization
M_S	Saturation magnetization
σ_R	Specific remanent magnetization
σ_S	Specific saturation magnetization
θ_C	Curie temperature
θ_N	Néel temperature

Table of Contents

ABSTRACT	ii
Acknowledgements	iv
List of Abbreviations	vi
CHAPTER 1. Introduction	1
1.1 Background on magnetic nanoparticles.....	1
1.2 Background on Ferrofluids and Colloidal Stabilization.....	3
1.2.1 Colloidal stability.....	3
1.2.2 Block copolymer stabilizers as dispersants for magnetic nanoparticles.....	7
1.3 Synthesis and stabilization of magnetic nanoparticles.....	9
1.3.1. Controlled size iron oxide nanoparticles.....	9
1.3.1.1. Magnetite.....	9
1.3.1.2. Maghemite.....	11
1.3.2 Controlled size cobalt nanoparticles.....	12
1.3.3. Controlled size cobalt ferrite nanoparticles.....	14
1.4 Magnetism overview.....	16
1.4.1 Fundamentals of magnetism.....	16
1.4.2 The Six Classes of Magnetic Materials.....	17
1.4.2.1 Diamagnetism.....	19
1.4.2.2. Paramagnetism.....	20
1.4.2.3. Ferromagnetism.....	21
1.4.2.4. Antiferromagnetism.....	23
1.4.2.5. Ferrimagnetism.....	24
1.4.2.6. Superparamagnetism.....	25
CHAPTER 2. Physical Characterization of Magnetic Nanoparticles	26
2.1. Transmission Electron Microscopy.....	26
2.1.1. Fundamentals.....	29
2.1.1.1. Electron Sources.....	29
2.1.1.2. Electromagnetic Lenses.....	31
2.1.1.2.1. Condenser Lens System.....	32
2.1.1.2.2. Objective Lens System.....	32
2.1.1.2.3. Intermediate Lens System.....	33
2.1.1.2.4. Projector Lens System.....	34
2.1.2. Electron-sample interactions.....	34
2.1.3. Limitations and difficulties with TEM.....	35
2.1.3.1. Specimen Limitations.....	35
2.1.3.2. Sampling Limitations.....	36
2.1.4. Data Acquisition with TEM.....	36
2.1.4.1. Imaging.....	37
2.1.4.1.1. Bright field imaging.....	38
2.1.4.1.2. High-resolution imaging.....	38
2.1.4.2. Spectroscopy.....	39
2.1.4.2.1. Electron Energy Loss Spectroscopy (EELS).....	39
2.1.4.2.1.1. Energy filtered imaging.....	41
2.1.4.2.1.2. Energy Dispersive X-ray Spectroscopy (EDX).....	42

2.1.4.3. Electron Diffraction	42
2.1.4.3.1. Selected area electron diffraction.....	43
2.1.4.3.2. Convergent beam electron diffraction (Nanodiffraction)	45
2.2 X-ray diffraction	46
2.3. Magnetometry	49
2.3.1. Superconducting Quantum Interference Device (SQUID) Based Magnetometer ...	50
2.3.2. Types of Experiments	51
2.3.2.1. Zero Field-Cooled/Field-Cooled Magnetization vs. Temperature Measurements	51
2.3.2.2. Room Temperature Magnetization vs. Applied Magnetic Field Measurements	52
2.3.2.3. Zero Field-Cooled/Field-Cooled Magnetization vs. Applied Magnetic Field Measurements	53
2.3.2.4. Henkel plot experiments	56
2.4. Small Angle X-ray Scattering.....	56
CHAPTER 3. Structural and Magnetic Properties of Oxidatively Stable Cobalt Nanoparticles Encapsulated in Graphite Shells	59
3.1 Abstract.....	59
3.2 Introduction.....	60
3.3 Experimental Section.....	61
3.3.1 Synthesis of poly(styrene- <i>b</i> -4-vinylphenoxyphthalonitrile).....	61
3.3.2 Cobalt nanoparticle synthesis.	61
3.3.3 Elevated heat treatment of polymer coated cobalt nanoparticles.....	61
3.3.4 Transmission electron microscopy.	62
3.3.5 Small angle x-ray scattering.....	62
3.3.6 X-ray Diffraction.	62
3.3.7 Magnetic Susceptometry.....	63
3.3.8 Elemental analysis.	63
3.4 Results and Discussion	64
3.4.1 Particle size analysis.	64
3.4.2 Small angle x-ray scattering.....	64
3.4.3 Transmission Electron Microscopy.	65
3.4.4 X-ray Diffraction.	66
3.4.5 Magnetic Susceptometry.....	67
3.5 Conclusions.....	69
3.6 Acknowledgements.....	69
CHAPTER 4. Structural and magnetic properties of as-prepared and heat treated cobalt nanoparticles stabilized with a siloxane-based block copolymer system	79
4.1 Abstract.....	79
4.2 Introduction.....	80
4.3 Experimental	81
4.3.1. Synthesis of poly(dimethylsiloxane- <i>b</i> -(methylvinylsiloxane- <i>co</i> -methyl(2-trimethoxysilyl) siloxane)) (PDMS- <i>b</i> -(PMVS- <i>co</i> -PMTMS).	81
4.3.2 Synthesis of a cobalt nanoparticles.	82
4.3.3 Heat treatment of PDMS- <i>b</i> -(PMVS- <i>co</i> -PMTMS) coated cobalt nanoparticles.	82
4.3.4 Exposure of samples to ambient conditions.....	82

4.3.5	Transmission Electron Microscopy.....	82
4.3.6	X-ray Diffraction.....	83
4.3.7	Magnetic Susceptometry.....	83
4.3.8	Elemental Analysis.....	84
4.4	Results and Discussion.....	84
4.4.1	Transmission Electron Microscopy.....	84
4.4.2	X-ray diffraction.....	86
4.4.3	Magnetic Susceptometry.....	86
4.5	Conclusions.....	89
4.6	Acknowledgements.....	89
CHAPTER 5. Structural and magnetic properties of anisotropic cobalt ferrite nanoparticles with and without a hydrophilic block copolymer coating.....		98
5.1	Abstract.....	98
5.2	Introduction.....	98
5.3	Experimental.....	101
5.3.1	Synthesis of Triblock Copolymer Dispersant.....	101
5.3.2	Preparation of Polymer Coated Nanoparticles.....	101
5.3.3	Elemental Analysis.....	101
5.3.4	Transmission Electron Microscopy.....	101
5.3.5	X-ray Powder Diffraction.....	102
5.3.6	Magnetic Susceptometry.....	102
5.4	Results and Discussion.....	103
5.4.1	Elemental Analysis.....	103
5.4.2	Transmission Electron Microscopy.....	103
5.4.3	X-ray Powder Diffraction.....	104
5.4.4	Magnetic Susceptometry.....	105
5.5	Conclusions.....	106
5.6	Acknowledgements.....	107
CHAPTER 7. Recommendations for Future Work.....		117
REFERENCES.....		119
VITAE.....		127

List of Figures

Figure 1.2.1 A) Electrostatically stabilized particles and B) potential energy vs. interparticle distance diagram.	6
Figure 1.2.2 Schematics of A) depletion stabilization and B) steric stabilization	7
Figure 1.2.3 Proposed stabilization of magnetite by carboxylate groups	8
Figure 1.4.1 Schematic of magnetic dipole moment alignments in zero applied-field at room temperature for: A) paramagnetic or superparamagnetic material, B) ferromagnetic material, C) antiferromagnetic material and D) ferrimagnetic material.	18
Figure 1.4.2 Room temperature M vs. H plot for a diamagnetic Teflon sample holder	19
Figure 1.4.3 Magnetization vs. Magnetic Field plots for a material with a paramagnetic impurity at: 300 K (—) and 5 K (---).....	21
Figure 1.4.4 A) material with two domains has energy decreased by $\frac{1}{2}$, B) material with four domains has energy decreased by $\frac{1}{4}$, C) material in zero applied field and D) material in strong applied field	23
Figure 2.1.1 Schematic of a transmission electron microscope with the source, lenses and apertures labeled.	28
Figure 2.1.2 Diagram of thermionic emission gun. A) cathode or emission source, B) Wehnelt cap, C) anode and D) electron beam.	30
Figure 2.1.3 Diagram of field-emission gun: A) emission source or cathode, B) extraction anode, C) acceleration anode and D) electron beam.	31
Figure 2.1.4 Schematic of electrons from primary beam of TEM interacting with sample	35
Figure 2.1.5 A) high-resolution image and B) corresponding Fourier transform indicating the repeating frequencies in the image.	39
Figure 2.1.6 Electron energy-loss spectrum indicating energy ranges where energy-filtered images are acquired.....	42
Figure 2.1.7 Schematic of incident electrons diffracting from lattice planes	43
Figure 2.1.8 A) Selected area diffraction spot pattern and B) Nano-beam electron diffraction pattern	46
Figure 2.2.1 Schematic of electronic shells	48
Figure 2.3.1 Diagram of SQUID sensing device	51
Figure 2.3.2 Hysteresis loop indicating locations of points of interest.....	53
Figure 2.3.3 Schematic showing the behavior of magnetic dipoles of ferromagnetic (FM) and antiferromagnetic (AFM) components of a material undergoing a field-cooled hysteresis loop measurement	55
Figure 2.4.1 Vector diagram of incident radiation (S_0) and radiation scattered from X (S).....	57
Figure 2.4.2 Diagram of small angle x-ray scattering instrument	58
Figure 3.1 Poly(styrene- <i>b</i> -4-vinylphenoxyphthalonitrile)	72
Figure 3.2 Particle size histograms for: A) pre-heat-treated and B) heat-treated samples	72
Figure 3.3 A) Bright-field image of pre-heat-treated sample, B) corresponding cobalt distribution image of (A), C) bright-field image of heat-treated sample and D) corresponding cobalt distribution image of (C). Scale bars = 100 nm	73
Figure 3.4 A) HRTEM of pre-heat-treated sample, B) HRTEM of heat-treated sample showing multiple twinning within a single crystal, C) indexed nano-beam electron diffraction pattern of $\langle 011 \rangle$ zone axis of fcc cobalt.....	74

Figure 3.5 A) High-resolution image of hcp cobalt particle and B) Fourier transform of “A” showing graphite and hcp spacings. Inset in A is a magnified region of graphitic layers...	75
Figure 3.6 X-ray diffraction pattern for pre-heat-treated sample. Vertical lines are peak matches provided by the JCPDS software database.	76
Figure 3.7 X-ray diffraction pattern for heat-treated sample. Vertical lines are peak matches provided by the JCPDS software database.	76
Figure 3.8 σ vs. H measurements conducted at A) 300 K and B) 5 K (zero-field cooled hysteresis loop —, field-cooled hysteresis loop •••) on pre-heat-treated cobalt-polymer complexes that had been aged under ambient conditions for three months. C) shows enlarged region around the origin for 5 K hysteresis loops showing the asymmetric field-cooled hysteresis loop shift.	77
Figure 3.9 σ vs. H measurements conducted on a cobalt-copolymer sample that had been thermally treated at 700°C at A) 300 K (4 day acid digestion (•••) and 13 day acid digestion (—)) and B) 5 K (13 day acid digestion: zero field-cooled (—), field-cooled (•••)). C) shows enlarged region around the origin for 5 K hysteresis loops (13 day acid digestion) and shows minimal field-cooled hysteresis loop shift. The horizontal line at 160 emu g ⁻¹ Co in (A) indicates the maximum reported specific magnetization for cobalt metal.	78
Figure 4.1 PDMS- <i>b</i> -(PMVS- <i>co</i> -PMTMS).....	91
Figure 4.2 Logged particle size histograms for: A) pre-heat-treated sample (N1a), B) sample heated at 600°C (P1a) and C) sample heated at 700°C (P2a). Insets show particle size histograms in nm. Note: The raw data was logged and re-binned to generate the logged particle size histograms.....	91
Figure 4.3 A) bright field image of N1a, B) corresponding Co elemental map of A, C) bright field image of P1a, D) corresponding Co elemental map of C, E) bright field image of P2a and F) corresponding Co elemental map of E.	92
Figure 4.4 A) HRTEM image of pre-heat-treated sample (N1a), B) HRTEM image of sample heat-treated at 600°C (P1a) showing lattice planes consistent with hcp cobalt structure (arrows normal to denoted lattice planes) and C) nano-beam electron diffraction of P1a showing <011> zone axis of fcc cobalt.	93
Figure 4.5 A) HRTEM image of multi-twinned P2a particle showing lattice planes consistent with fcc cobalt structure, B) Fourier transform of lower twin in image A and C) Fourier transform of upper twin in image A.....	93
Figure 4.6 X-ray powder diffraction patterns for A) N1a, B) P1a and C) P2a.....	94
Figure 4.7 σ vs. H measurements conducted on N1 at A) 300 K (— N1a; — N1b) and B) 5 K (N1a: zero-field cooled hysteresis loop —, field cooled hysteresis loop ---; N1b: zero-field cooled hysteresis loop —, field cooled hysteresis loop ---). C) shows enlarged region around the origin for 5K hysteresis loops showing asymmetric field-cooled hysteresis loop shift.	95
Figure 4.8 σ vs. H measurements conducted on P1 at A) 300 K (— P1a; — P1b) and B) 5 K (P1a: zero-field cooled hysteresis loop —, field cooled hysteresis loop ---; P1b: zero-field cooled hysteresis loop —, field cooled hysteresis loop ---). C) shows enlarged region around the origin for 5K hysteresis loops.	96
Figure 4.9 σ vs. H measurements conducted on P2 at A) 300 K (— P2a; — P2b) and B) 5 K (P2a: zero-field cooled hysteresis loop —, field cooled hysteresis loop ---; P2b: zero-field cooled hysteresis loop —, field cooled hysteresis loop ---). C) shows enlarged region around the origin for 5K hysteresis loops.	97

Figure 5.1 TEM images of: A) uncoated nanoparticles and B) coated nanoparticles.	109
Figure 5.2 A) bright field image of uncoated sample, B) corresponding iron elemental map of A, C) corresponding oxygen elemental map of A, D) bright field image of coated sample, E) corresponding iron elemental map of D and F) corresponding oxygen elemental map of D	110
Figure 5.3 EELS spectrum from uncoated sample with edges labeled.....	111
Figure 5.4 High-resolution transmission electron micrographs of: A) uncoated sample and B) coated sample. Insets are Fourier transforms of respective images.....	111
Figure 5.5 Exemplary selected area diffraction pattern for uncoated sample.....	112
Figure 5.6 X-ray diffraction patterns for: A) uncoated sample, B) coated sample and C) pure polymer	113
Figure 5.7 Room temperature σ vs. H curves for uncoated (—) and coated (---) samples.....	114

List of Tables

Table 1.4.1 Table of quantities and units used in magnetism	17
Table 1.4.2 Description of classes of magnetic materials ³⁷	18
Table 3.1 Experimental and literature d-spacings for fcc cobalt for the pre-heat-treated sample.	71
Table 3.2 Experimental and literature d-spacings for fcc cobalt for the heat-treated sample.....	71
Table 4.1 Comparison of Experimental d-spacing ratios from SAD patterns for P1a and P2a with Literature fcc cobalt d-spacing ratios.....	90
Table 5.1 Ratios of experimental electron diffraction rings compared to literature values for magnetite.....	108
Table 5.2 Peak comparisons for experimental uncoated and coated samples with literature values for magnetite and pure polymer	108

CHAPTER 1. Introduction

1.1 Background on magnetic nanoparticles

A magnetic fluid (ferrofluid) based on magnetite (Fe_3O_4) was first prepared in the early 1960's by grinding micron-sized magnetite in a ball mill for weeks and subsequently stabilizing the particles with oleic acid. This seemingly archaic 'synthesis' led to a revolution of preparing synthetic 'nanoscale' magnetic materials in myriad ways. The term ferrofluid is derived from the 'ferromagnetic' behavior of fluids, containing magnetic nanoparticles, when exposed to a magnetic field. Nanoscale magnetic particles with a variety of compositions, sizes and stabilizers have been prepared in the past four decades. Several applications for these materials exist, as ferrofluids and in the solid state, primarily in the biomedical and magnetic recording industries. As the focus of this research is on the development of magnetic materials for biomedical applications, a brief background on nanoscale magnetic materials in biological systems is provided.

Magnetic nanoparticles were first discovered in a biological organism (chitons) in 1962. Some of the teeth of chitons are capped with magnetite (Fe_3O_4), which is proposed to provide the mechanical strength for eating algae from the first few millimeters of marine rocks.³ Magnetic nanoparticles are present in various other biological organisms (bacteria,⁴ rainbow trout,⁵ homing pigeons,⁶ etc.), with the proposition that the magnetic nanoparticles play a role in magnetoreception.^{5,6} More importantly, there exists a detectable quantity of nanoparticulate magnetite in humans, located in the heart and brain.^{7,8} The presence of magnetite in the body suggests that it is biocompatible, which may have implications in the potential *in vivo* administration of synthetic iron oxide based materials for biomedical applications.

Numerous current and potential commercial biomedical applications exist for systems comprised of magnetic nanoparticles. Current applications are focused on *in vitro* applications, such as: 1) cell and cell organelle detection and separation and 2) immobilization, isolation and determination of biologically active compounds.³ One current *in vivo* application for magnetic nanoparticles is as magnetic resonance imaging (MRI) contrast enhancement agents.⁹ Future potential applications focus further on the *in vivo* usage of magnetic nanoparticulate and microsphere systems with magnetic nanoparticle components. Some of these applications include, but are not limited to: 1) drug and radionuclide targeting therapies,³ 2) tumor

hyperthermia,^{10, 11} 3) retinal detachment disorder treatment¹² and 4) artificial muscle.³ Several review articles have been published on the applications of magnetic nanoparticles in biomedicine and the interested reader is referred to^{3, 9, 13, 14}.

Magnetic nanoparticulate systems receiving the most attention in the biomedical arena are the iron oxides (magnetite and maghemite), owing to their ease of preparation and oxidative stability, not to mention their biocompatibility. Other systems that have been under intense general investigation are ground state transition metals of iron, cobalt and nickel. Fe and Co have quite large magnetic susceptibilities compared with the iron oxides; however, the naked metals readily oxidize leading to a decline in their magnetic properties. Alloys of transition metals (FeCo,¹⁵ FePt,¹⁶ CoPt,¹⁷ FeCoNi,^{18, 19} etc.) have also been studied.

To understand the behavior of magnetic nanomaterials, in a fluid or in the solid state, thorough structural and magnetic characterization needs to be conducted. Transmission electron microscopy (TEM), high-resolution TEM (HRTEM), energy-filtered TEM (EFTEM) and electron diffraction are useful techniques for studying the size, morphology, chemical composition and crystallinity of magnetic nanomaterials and are demonstrated in many publications on these types of materials. X-ray diffraction (XRD) is another useful technique used to probe the crystal structure of nanomaterials, with the possibility of determining particle size using peak-broadening analyses. Magnetic susceptometry is critical in elucidating pertinent information on the magnetic behavior of any type of magnetic system. Several types of experiments are used to study the magnetic properties of nanomaterials. These experiments aid in determining the class of magnetic material present at different temperatures as well as the 'purity' of the sample. Impurities can be present as diamagnetic or paramagnetic species. Small angle x-ray scattering (SAXS) experiments can also be conducted, which provide information on the particle size and shape. These data can be correlated with TEM and XRD data on particle size to compare their consistency. This suite of analytical techniques provides the framework for defining material structural and magnetic properties, while assessing their potential for use in biomedical applications.

The objective of this research was to use TEM, HRTEM, EFTEM, electron diffraction, XRD, magnetic susceptometry and SAXS to analyze three different macromolecule-metal and macromolecule-metal oxide complexes: 1) poly(styrene-*b*-4-vinylphenoxyphthalonitrile)-cobalt, 2) poly(dimethylsiloxane-*b*-(methylvinylsiloxane-*co*-methyl(2-trimethoxysilyl)ethyl)siloxane))-

cobalt and 3) a triblock copolymer comprised of a carboxylic acid containing urethane central block and poly(ethylene oxide) end blocks-mixed ferrite. The analysis of each system will be presented in successive chapters, which have been or will be submitted for publication. It is, however, necessary to provide adequate background information prior to the experimental chapters. The following sections in this chapter will discuss: 1) ferrofluid stabilization theory, 2) methodologies for synthesizing and dispersing magnetic nanoparticles and 3) an overview of magnetism. Chapter 2 provides a general overview of the analytical techniques proposed, with most attention focused on TEM and related techniques. Chapters 3-5 are experimental chapters describing the analysis of the three sets of materials previously described. Chapter 6 offers conclusions and suggestions for future research.

1.2 Background on Ferrofluids and Colloidal Stabilization

Ferrofluids are colloidal dispersions of magnetic metallic particles in a liquid medium. A colloid is described as a system where at least one of the components is in the nanometer to micrometer range.²⁰ Dispersants are either surfactants or macromolecules that physically adsorb or chemically react with the magnetic particles rendering them dispersible in a liquid. In a ferrofluid, nanometer to micrometer sized magnetic particles can be dispersed by a variety of methods, the most popular of which is coating the particles with dispersants. Dispersants can be added either prior to particle synthesis, where they additionally serve as nanoreactor templates, or after particle synthesis where they act solely as dispersing agents. To understand the importance of dispersants in colloidal stability, background information on the attractive forces inherent in ferrofluids and mechanisms of colloidal stability is necessary.

1.2.1 Colloidal stability

To obtain a stable ferrofluid, the forces separating particles need to be greater than the attractive forces between particles. The primary attractive forces in a ferrofluid system are: 1) van der Waals forces and 2) magnetostatic forces. Moreover, the force of gravity affects all colloidal systems and can result in sedimentation. Attractive forces can lead to particle agglomeration, which then makes a system more susceptible to sedimentation.

Sedimentation occurs when the gravitational force acting on a particle is greater than the thermal energy (kT) required for keeping the particle suspended indefinitely. Sedimentation is

governed by two forces: the force of gravity and the force of friction. The forces will be equal for particles falling with a constant velocity, expressed in the following equation,

$$6\pi\eta R w = \frac{4}{3}\pi R^3(\rho - \rho_o)g \quad 1.2.1$$

where η is the viscosity of the medium, R is the radius of a particle, w is the sedimentation velocity, ρ is the density of the solid particles, ρ_o is the density of the medium and g is the acceleration due to gravity.²¹ The relationship expressed in equation 1.2.2 shows how particles must be designed to overcome the force of gravity while in solution (V is the particle volume, h is the height of the container, k is Boltzmann's constant and T the temperature in degrees Kelvin).²²

$$(\rho - \rho_o)Vgh \leq kT \quad 1.2.2$$

There is a size limit above which particles will sediment and below which particles will remain suspended indefinitely. The size is dependent upon the density of the colloidal material and is ~ 10 nm for magnetite (Fe₃O₄) particles with a density of 5.2 g cm³.²³ Particle size can increase in solution due to attractive forces, thus increasing the likelihood of sedimentation.

Van der Waals forces arise from a variety of dipole-dipole interactions: permanent dipole-permanent dipole, permanent dipole-induced dipole and induced dipole-induced dipole. The third class of induced dipole-induced dipole forces, also termed London dispersion forces or flickering dipole forces, are the main forces involved in long-range attraction in colloidal systems. The change in polarization of electron clouds is spontaneous and occurs on a time scale of femtoseconds.²⁴ The mutually attractive force is weak between two atoms; however, when considering the numbers of atoms in colloidal particles and the sum of their forces, the resulting attraction is significant. The following equation describes the van der Waals attractive force between two spherical particles:

$$V_{vdW} = -\frac{A}{6} \left(\frac{2R^2}{(2R + D)^2 - 4R^2} + \frac{2R^2}{(2R + D)^2} + \ln \left(\frac{(2R + D)^2 - 4R^2}{(2R + D)^2} \right) \right) \quad 1.2.3$$

where R is the radius of the particles (assumed to be monodisperse), D is the distance between particle centers and A is the Hamaker constant (~ 10⁻²⁰ J for magnetite).²⁵ The van der Waals attractive force between particles scales as R^{-6} . Van der Waals attraction needs to be minimized to prevent particle agglomeration, which can lead to sedimentation.

Magnetostatic interactions arise from the magnetic dipoles of colloidal magnetic particles in solution. These forces are attractive and can be due to the magnetization of a sample when placed in an externally applied magnetic field or any inherent remanent magnetization of individual particles. Only the first case has been considered, and the following expression describes the magnetostatic attraction between two particles:

$$V_M = \frac{\mu_o}{4\pi r^3} [(\mathbf{m}_1 \cdot \mathbf{m}_2) - 3(\mathbf{m}_1 \cdot \hat{\mathbf{r}})(\mathbf{m}_2 \cdot \hat{\mathbf{r}})] \quad 1.2.4$$

where μ_o is the permeability of a vacuum, \mathbf{m}_1 and \mathbf{m}_2 are interacting dipole moments, r is the distance of particle separation and $\hat{\mathbf{r}} \cdot r$ is the vector connecting the particle centers.²⁶⁻²⁸ Magnetostatic interactions, similar to van der Waals interactions, can lead to agglomeration and sedimentation and should also be prevented. The sum of all attractive forces (V_T) is represented by equation 1.2.5.

$$V_T = V_{vdW} + V_M \quad 1.2.5$$

To limit the attractive forces in a ferrofluidic system, repulsive mechanisms need to be introduced, whose forces are greater than the sum of the attractive forces.

Two stabilization mechanisms are commonly employed to overcome van der Waals and magnetostatic attractive forces: 1) electrostatic stabilization and 2) polymeric stabilization. Electrostatic stabilization involves creating a charge on the surface of colloidal particles. When the surface of a particle is charged the counter-ions are also present, which creates an electric double-layer. The potential energy between two similarly charged particles increases upon their approach, leading to repulsion (Figure 1.2.1). This mechanism is not often used in ferrofluid systems; however, the interested reader is referred to a manuscript written by Massert.²⁹

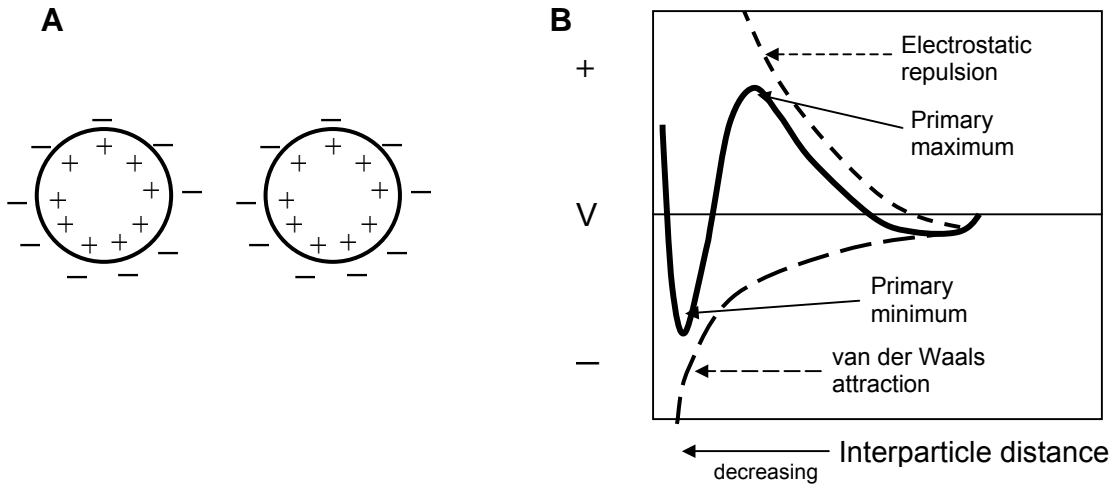


Figure 1.2.1 A) Electrostatically stabilized particles and B) potential energy vs. interparticle distance diagram.

Polymeric stabilization utilizing non-ionic polymers can occur by two different mechanisms: depletion stabilization and steric stabilization. Depletion stabilization, which utilizes dissolved polymers in solution to stabilize colloidal particles, is not commonly used in ferrofluid synthesis (Figure 1.2.2 A). Steric or entropic stabilization, the most common method used in ferrofluid synthesis, occurs when polymers are physically adsorbed or chemically grafted onto the surface of magnetic colloidal particles (Figure 1.2.2 B). When coated colloidal particles are in a good solvent for the polymer molecules, the bound polymer molecules extend away from the particle surfaces to gain configurational entropy. When two coated particles approach one another under good solvent conditions, the polymer molecules from one particle impinge upon the volume occupied by the polymer molecules from another particle. This impingement leads to a decrease in configurational entropy of the polymer molecules and thus an increase in free energy of the system. A repulsive force is generated which leads to particle separation, thereby restoring the configurational entropy of the polymer molecules and decreasing the free energy of the system.^{30,31} The range of the repulsive force is greater than the distance required for van der Waals attractive forces to act and effectively reduces or eliminates the effect of van der Waals attractive forces. Particles need to be completely covered with polymer molecules for the repulsive mechanism to operate. If particles are not entirely covered, polymers can act as bridges between particles leading to particle agglomeration.³⁰ The reader is referred to

Israelachvili, Evans and Wennerstrom and Napper for more information on steric stabilization theory.^{24, 30, 31}

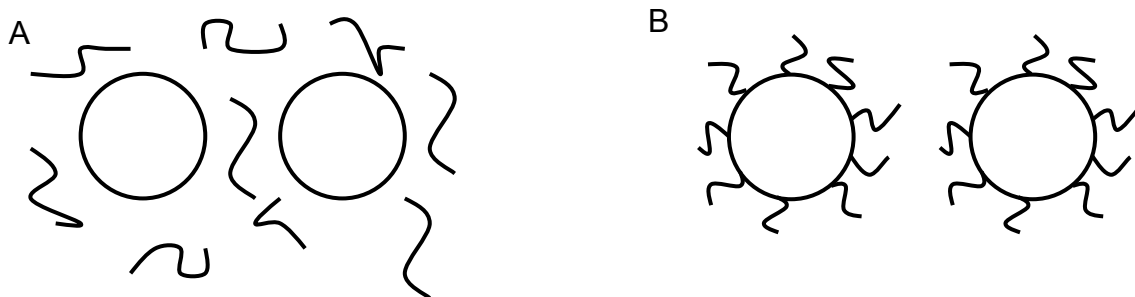


Figure 1.2.2 Schematics of A) depletion stabilization and B) steric stabilization

Surfactants are commonly utilized for sterically stabilizing magnetic nanoparticles; however, they provide less flexibility when designing systems for various applications. Thus, the focus of this section will be on the use of block copolymer dispersants for stabilizing magnetic nanoparticles.

1.2.2 Block copolymer stabilizers as dispersants for magnetic nanoparticles

A block copolymer is a polymer having at least two different blocks, usually with different solubility characteristics. Block copolymers are known to be good steric stabilizers, and they can be designed to perform in a variety of media. The anchor block(s) is the block that adsorbs or binds (physically or chemically) to the colloid and is usually less soluble in the dispersing medium than the stabilizing block. The stabilizing block(s) is soluble in the dispersing medium and serves to sterically stabilize the colloidal particle to which it is attached. Stabilization is imparted by the repulsive nature of the stabilizing blocks projecting into the dispersing medium. Polymers that are anchored to a substrate have less conformational freedom than polymers that are not bound and as a result, display more conformational entropy when solvated. This concept has been demonstrated experimentally, where the root mean square end-to-end distance and characteristic ratio for bound poly(methylene) were greater than for free poly(methylene).²⁴

When using block copolymers as stabilizers in colloidal magnetic nanoparticle systems, the nature of the interaction between the anchor block and the magnetic particle (physical or

chemical) can be controlled. It is known that carboxylates, phosphates and sulfates bind to magnetite (Fe_3O_4),³² so a block copolymer designed to stabilize magnetite nanoparticles can be tailored with these functional groups. Harris *et al.* reported the stabilization of magnetite nanoparticles with a triblock copolymer containing carboxylic acid functional groups that would bind to magnetite. The anchoring is proposed to occur through the carboxylate anions of the carboxylic acid containing central block and positive Fe or protonated water groups on the surface of the magnetite particles. The poly(ethylene oxide) tail blocks serve to sterically stabilize the particles in solution (Figure 1.2.3).³³ The anchoring of polymer blocks to other magnetic nanoparticles (Co, Fe, CoFe, etc.) is less understood; however, block copolymers are proposed to play an active role in particle formation.

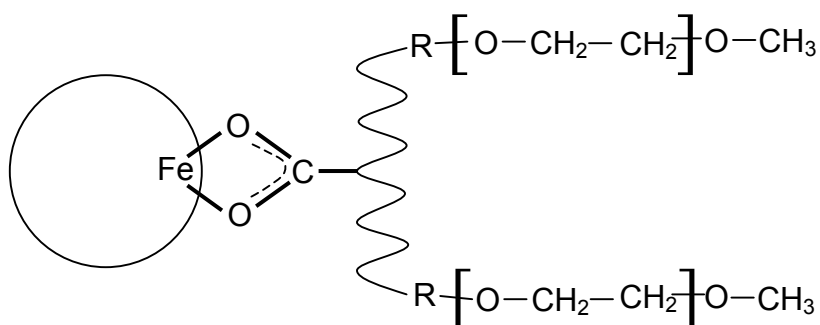


Figure 1.2.3 Proposed stabilization of magnetite by carboxylate groups

In 1966, Thomas suggested that polymers with polar groups promote the growth of cobalt particles ranging from 2-30 nm, using a procedure of thermally decomposing dicobalt octacarbonyl in a solution of a poly(methyl methacrylate-ethyl acrylate-vinyl pyrrolidone) terpolymer and toluene.³⁴ More recently, Wilcoxon *et al.* proposed that iron atoms may form a charge complex with ether groups of a non-ionic polyether surfactant or the polar $\text{R}_3\text{N}^+ \text{Br}^-$ headgroup of a cationic dodecyltrimethylammonium bromide surfactant. Both reactions utilized octane as the solvent, anhydrous $\text{Fe}(\text{BF}_4)_2$ as the iron species and LiBH_4 as a reducing agent. The iron precursor was not dissolved in water; rather, it was incorporated into each surfactant prior to dissolution in octane. Spectroscopic charge-transfer bands shifted in position and energy depending on whether the iron atoms were in the presence of the ether or ammonium groups, suggesting the formation of iron-surfactant complexes.³⁵ It appears likely that the interaction of nucleophilic (electron donating) species with metal atoms may occur before particle formation,

at least in cases where the copolymer surfactants are random copolymers. In such cases, the copolymers typically do not form micelles in the solutions in the absence of the metal complexing agents. This interaction between soluble chains and metal complexing agents may bring multiple metal atoms together in the center of aggregates where they can condense into metallic nanoparticles upon thermal or chemical treatment.

There are several methods for the solution preparation of magnetic nanoparticles. Most methods involve thermally or chemically treating a solution comprised of a metal salt or an organometallic precursor and a dispersant. The dispersants can form micelles in solution without the complexing agents present if their solubility characteristics and copolymer architectures are appropriate, and these may serve as restrictive environments or templates that control the particle size. Magnetic particles can also be synthesized without a dispersant and subsequently coated. The next section will discuss the preparation and steric stabilization of iron oxide, cobalt and cobalt ferrite magnetic nanoparticles.

1.3 Synthesis and stabilization of magnetic nanoparticles

Various synthetic methodologies for preparing magnetic nanoparticles have been reported in the literature. This section will give an overview of research pertinent to this dissertation, namely on the synthesis and stabilization of iron oxide, cobalt and cobalt ferrite magnetic nanoparticles.

1.3.1 Controlled size iron oxide nanoparticles

The most well-known synthetic iron oxides are magnetite (Fe_3O_4) (saturation magnetization (M_S) = 92 emu g^{-1}) and maghemite ($\gamma\text{-Fe}_2\text{O}_3$) (M_S = 74 emu g^{-1}).³⁶ Sections 1.3.1.1 and 1.3.1.2 will focus on the controlled syntheses of magnetite and maghemite nanoparticles respectively, in templates formed from aggregated structures in dispersions.

1.3.1.1 Magnetite

Magnetite (Fe_3O_4) is a mixed iron oxide ($\text{FeO}\cdot\text{Fe}_2\text{O}_3$) with an inverse spinel crystal structure. In the inverse spinel structure, half of the Fe^{+3} ions are tetrahedrally coordinated and the other half of the Fe^{+3} ions and all of the Fe^{+2} ions are octahedrally coordinated. Each octahedral site has six nearest neighbor O^{2-} ions arranged on the corners of an octahedron, while

each tetrahedral site has four nearest neighbor O²⁻ atoms arranged on the corners of a tetrahedron.³⁷

Magnetite nanoparticles can be prepared in a number of ways, the most common of which is the chemical co-precipitation of Fe salts with the addition of a hydroxide base. The co-precipitation procedure can be performed with or without a dispersant. Harris *et al.* demonstrated the post-production coating of Fe₃O₄ nanoparticles prepared sans surfactant. The dispersant employed was a triblock copolymer comprised of poly(ethylene oxide) tail blocks and a carboxylic acid containing urethane central block. The dispersant was dissolved in an organic solvent and stirred with the aqueous suspension of magnetite nanoparticles, which allowed the interfacial interaction of the dispersant with the particles. The interaction between the carboxylic acid groups of the dispersant and the Fe atoms on the particle surfaces led to stabilized magnetite nanoparticles with a mean diameter of 8.8 ± 2.7 nm.³³

Mendenhall *et al.* prepared Fe₃O₄ by the co-precipitation of FeSO₄ and FeCl₃ followed by sonicating the particles in the presence of poly(methacrylic acid) (PMAA). This procedure led to stable ferrofluids with an average particle diameter of ~ 9 nm.³⁸ Lee *et al.* prepared magnetite nanoparticles by co-precipitating FeCl₂ and FeCl₃ with NaOH in the presence of poly(vinyl alcohol) (PVA). The magnetite particles were oxidatively stable with particle sizes ranging from 3.8 nm to 6.6 nm depending on the concentration of PVA used.³⁹

Lee *et al.* used sodium bis(2-ethylhexyl) sulfosuccinate (AOT) to prepare magnetite nanoparticles by a reverse micelle method. In the reverse micelle method, two microemulsions are prepared. The first microemulsion is comprised of AOT micelles containing an aqueous solution of Fe salts as the dispersed phase and isooctane as the continuous phase. The second microemulsion is comprised of AOT micelles containing aqueous NaOH as the dispersed phase and isooctane as the continuous phase. The two microemulsions are mixed together, where the dispersed aqueous phases interact with one another leading to magnetite nanoparticles ranging from ~ 5 to 15 nm in diameter depending on the ratio of water:AOT used.⁴⁰

Wormuth synthesized magnetic iron oxide nanoparticles from an aqueous solution of FeCl₃ and FeCl₂ salts (2:1 molar ratio) and hydrophilic block copolymer (poly(ethylene oxide-*b*-methacrylic acid)). The addition of ammonium hydroxide (NH₄OH) generated well-dispersed magnetic nanoparticles with a size of 5 ± 4 nm.⁴¹ Wormuth was not able to define the iron

oxide as being either magnetite or maghemite; however, the stoichiometry of Fe salts used would produce magnetite in an ideal reaction.

1.3.1.2 Maghemite

Maghemite ($\gamma\text{-Fe}_2\text{O}_3$) has a cubic crystal structure similar to the inverse spinel crystal structure of magnetite and was the most common magnetic material used in magnetic recording media as of 1994, owing to the coercivity values of anisotropic maghemite nanoparticles (~200 to 400 Oe).³⁷ Maghemite is commonly synthesized by the co-precipitation of iron salts in the presence of base. Lopez Perez *et al.* prepared 2 to 8 nm maghemite nanoparticles using a nonionic surfactant (Brij 97), which is comprised of an oleyl block and a poly(ethylene oxide) block (10 repeat units), in a double microemulsion procedure. One microemulsion consisted of 1 M FeSO_4 , 0.5 M FeCl_3 and 0.1 M HCl as the aqueous dispersed phase and cyclohexane and Brij 97 as the organic phase. The other microemulsion had the same organic phase, but the aqueous dispersed phase contained cyclohexylamine instead of iron salts. The microemulsions were mixed together at 65°C, where the dispersed phases reacted to afford maghemite nanoparticles. The particle size, which ranged from ~2 to 7 nm, could be controlled by changing the ratio between cyclohexane, Brij and aqueous iron salt solution.⁴²

Another synthetic method employed to produce maghemite nanoparticles is the thermal decomposition of $\text{Fe}(\text{CO})_5$ to generate Fe^0 nanoparticles. The Fe^0 nanoparticles are subsequently oxidized to afford $\gamma\text{-Fe}_2\text{O}_3$ nanoparticles. This process has been used to prepare controlled size $\gamma\text{-Fe}_2\text{O}_3$ stabilized with small molecule surfactants (fatty acids).^{43, 44} Euliss and Grancharov *et al.* thermally decomposed $\text{Fe}(\text{CO})_5$ in oleic acid micelles to afford Fe^0 nanoparticles. The subsequent oxidation of the Fe nanoparticles led to $\gamma\text{-Fe}_2\text{O}_3$ nanoparticles, which were then treated with tetramethylammonium hydroxide and sodium citrate to form electrostatically stabilized nanoparticles. The electrostatically stabilized nanoparticles were mixed with a block copolyptide of poly(N_ϵ -2[2-(2-methoxyethoxy)ethoxy]acetyl-L-lysine)₁₀₀-*b*-L-aspartic acid sodium salt)₃₀, leading to stabilized clusters where the carboxylic acid moiety of aspartic acid groups binds to maghemite crystals. It was hypothesized that the aspartic acid blocks would form the core of block copolyptide micelles, wherein multiple maghemite nanoparticles would be encased possibly bound to more than one aspartic acid block.⁴⁵

Underhill *et al.* prepared maghemite in crosslinked triblock copolymer templates. First a triblock copolymer of poly(isoprene-*b*-2-cinnamoyl ethylmethacrylate-*b*-*tert*-butylacrylate) (PI-*b*-PCEMA-*b*-PtBA) was dissolved in tetrahydrofuran (THF) and irradiated with UV radiation to crosslink the PCEMA block and form polymer capsules. Next, the PI block was hydroxylated and the *tert*-butyl groups of the PtBA were cleaved to generate poly(2,3-dihydroxyisoprene) (PHI) and poly(acrylic acid) (PAA) respectively. The crosslinked capsules were dispersed in water to which FeCl₂ was added. The solution was stirred for 24 hours and the capsules were subsequently removed and placed into water, where NaOH was added to a pH of 10. Finally, H₂O₂ was added to oxidize the Fe⁺² ions to Fe₂O₃. Particles synthesized by this method ranged from 4 to 16 nm in diameter.⁴⁶

1.3.2 Controlled size cobalt nanoparticles

Cobalt has three known crystal structures: face-centered cubic (fcc), hexagonal close packed (hcp) and epsilon (ϵ). The normal room temperature bulk crystal phase of cobalt is hcp; however, the high-temperature phase (>450°C) of fcc cobalt is commonly reported for nanoscale materials at or below room temperature. A new phase of cobalt (ϵ -cobalt), published in 1999, is described as having a primitive cubic structure resembling the β -phase of manganese.⁴⁷ The three phases of cobalt are energetically similar and hence, multiple phases of cobalt can be present owing to the low activation energy required for phase transformation.^{47, 48}

Cobalt nanoparticles are usually synthesized by the reduction of Co salts or the thermal decomposition of organometallic precursors; however, electron beam vapor deposition has also been used to produce metallic cobalt nanoparticles.⁴⁹ Most methods in the literature involve the use of small molecule surfactants or other small molecule ligands to stabilize cobalt nanoparticles. Puntès *et al.*, Sun *et al.*, Murray *et al.* and Hütten *et al.* used a combination of oleic acid and an alkyl phosphine or alkyl phosphine oxide to synthesize cobalt nanoparticles,^{48, 50-52} while Dinenga *et al.* used only trioctylphosphine oxide (TOPO) in their preparation of cobalt nanoparticles.⁴⁷ Cobalt nanoparticles can also be prepared in reverse micelles using a cobalt containing surfactant (Co(AOT)₂) as the cobalt source, followed by NaBH₄ reduction and stabilization by a fatty acid or TOPO.⁵³⁻⁵⁵ Moreover, Co₂(CO)₈ can be used as the cobalt precursor and thermally decomposed in toluene with AOT or AOT:oleic acid as the reverse micelle templates. Varying the concentrations of AOT and/or oleic acid leads to particle size

control from 3.9 nm for 2 mmol AOT to 13.1 nm for 0.01 mmol AOT:0.05 mmol oleic acid.⁵⁶ Another reverse micelle method employs didodecyldimethylammonium bromide (DDAB) in toluene for the micellar template, $\text{Co}(\text{Cl})_2$ as the cobalt source and NaBH_4 as the reducing agent to generate ~2 to 5 nm Co nanoparticles by varying the $\text{Co}(\text{Cl})_2$ concentration.⁵⁷

Poly(vinyl pyrrolidone) homopolymers have been used as polymeric stabilizers in the synthesis of Co nanoparticles by decomposing $\text{Co}(\eta^3\text{-C}_8\text{H}_{13})(\eta^4\text{-C}_8\text{H}_{12})$ with H_2 . This method affords superparamagnetic (discussed in section 1.4.2.6) Co nanoparticles with diameters between 1 and 2 nm.^{58, 59} Cobalt nanoparticles were synthesized in block copolymers as early as 1966. Thomas prepared controlled size Co nanoparticles (from 2 to 30 nm in diameter) by the thermal decomposition of $\text{Co}_2(\text{CO})_8$ in toluene in the presence of a poly(methylmethacrylate-ethylacrylate-vinyl pyrrolidone) terpolymer. Particle size was controlled by varying reagent concentrations, temperature and polymer composition. Thomas hypothesized that polymers with a large percentage of polar groups facilitate the synthesis of smaller cobalt particles.³⁴ Tadd *et al.* employed a poly(styrene-*b*-methyl methacrylate) block copolymer system to synthesize Co nanoparticles by the thermal decomposition of $\text{Co}_2(\text{CO})_8$ in toluene at 90°C for 16 hours, which afforded ~2 nm diameter Co nanoparticles. It was hypothesized that the poly(styrene) block was more soluble in the toluene, thus forming the corona of the micelle (stabilizing block) and the poly(methyl methacrylate) block formed the core of the micelle (anchor block). Furthermore, Fourier transform infrared spectroscopy (FTIR) revealed new absorption bands owing to the interaction between the PMMA ester groups and the cobalt particles.⁶⁰

Stevenson *et al.* demonstrated the use of poly(dimethylsiloxane-*b*-(3-cyanopropyl)methylsiloxane-*b*-dimethylsiloxane) (PDMS-*b*-PCPMS-*b*-PDMS) triblock copolymers as micellar templates for the preparation of Co nanoparticles by the thermal decomposition of $\text{Co}_2(\text{CO})_8$ in toluene at 100°C. Co nanoparticles with diameters ranging from 7 to 18 nm were prepared. Since toluene is a good solvent for the PDMS blocks and a poor solvent for the PCPMS blocks, the PDMS blocks will form the corona of the micelles while the PCPMS central blocks will form the core of the micelles. TEM revealed that particles were well-coated with polymer sheaths; however, the saturation magnetization values were lower than bulk cobalt suggesting that oxidation of cobalt had taken place.⁶¹ Rutnakornpituk *et al.* also used PDMS-*b*-PCPMS-*b*-PDMS triblock copolymer templates to prepare Co nanoparticles by the same method, but studied the effects of $\text{Co}_2(\text{CO})_8$:copolymer ratio and copolymer block lengths on particle

size. Particle diameters increased from 6 nm for low concentration reactions (0.2 g $\text{Co}_2(\text{CO})_8$:1 g copolymer) to 10 nm for medium concentration reactions (1.0 g $\text{Co}_2(\text{CO})_8$: 1 g copolymer) while higher concentrations of $\text{Co}_2(\text{CO})_8$ to copolymer resulted in particle aggregation. Varying the PCPMS block from 2,000 to 5,000 g mol^{-1} and the PDMS blocks from 5,000 to 15,000 g^{-1} did not have a noticeable effect on the particle size. The magnetization of Co nanoparticles was monitored over time to evaluate their oxidative stability, with results indicating that 0.3 to 0.9% of the magnetization was lost per day due to oxidation. Nanoparticle stabilization was proposed to take place via nitrile group interaction with the cobalt nanoparticle surfaces.⁶² Cobalt nanoparticles with improved oxidative stability were prepared by Connolly *et al.* using a pentablock copolymer comprised of poly(dimethylsiloxane-*b*-methyltriethoxysilylethylsiloxane-*b*-(3-cyanopropyl)methyl siloxane-*b*-methyltriethoxysilylethylsiloxane-*b*-dimethylsiloxane) (PDMS-PMTEOS-PCPMS-PMTEOS-PDMS). The PCPMS block is proposed to bind to the Co nanoparticle surfaces through nitrile group interaction, the PMTEOS blocks are catalytically condensed to form a protective silica shell around the particles and the PDMS blocks act as steric stabilizers. A decrease in oxidation was reported for particles with a silica coating compared with particles lacking a silica coating, suggesting the efficacy of this method for preparing oxidatively stable Co nanoparticles.⁶³

1.3.3 Controlled size cobalt ferrite nanoparticles

Cobalt ferrite belongs to a group of transition metal oxide known as simple ferrites with the chemical formula $\text{MO}\cdot\text{Fe}_2\text{O}_3$, where M is usually Mn, Fe, Co, Ni or Zn. Cobalt ferrites are prepared similarly to magnetite, which stands to reason, as the only difference is the divalent cation (Fe^{+2} for magnetite and Co^{+2} for cobalt ferrite).

Song *et al.* reported the synthesis of controlled CoFe_2O_4 nanoparticles using Co and Fe coordination precursors. $\text{Co}(\text{acac})_2$, 1,2-hexadecane diol, oleic acid and oleylamine were added to phenyl ether and heated to 140°C. A solution of $\text{Fe}(\text{acac})_3$ and phenyl ether was added dropwise, whereafter the temperature was increased to 240°C and held for 30 min. This process generated 5 nm spherical nanoparticles with a spinel crystal structure, which were then used as seeds to create larger spherical or cubic nanoparticles depending on the ratio of surfactant and additional precursor added to the seed nanoparticles.⁶⁴ Moumen *et al.* synthesized 2, 3 and 5 nm CoFe_2O_4 particles by adding aqueous methylamine ($\text{CH}_3\text{NH}_3\text{OH}$) to a solution of cobalt

dodecylsulfate and iron dodecylsulfate surfactants and stirring the solution at room temperature. The counter ions of the surfactants (Fe^{+2} and Co^{+2}) serve as the reactants and are in a ratio of 3:1, instead of the 2:1 ratio needed for CoFe_2O_4 , because the oxidation of Fe^{+2} to yield Fe^{+3} is ~65%.⁶⁵ Ngo *et al.* prepared cobalt ferrite nanoparticles with only 3.5 wt% cobalt utilizing the Co and Fe dodecylsulfate route demonstrated by Moumen *et al.* to generate $\text{Co}_{0.13}\text{Fe}_{2.58}\text{X}_{0.29}\text{O}_4$ nanoparticles (where X is a cationic vacancy). Necessary concentrations of $\text{Co}(\text{DS})_2$ and $\text{Fe}(\text{DS})_2$ were prepared in an aqueous solution to which $\text{CH}_3\text{NH}_3\text{OH}$ was added. Nanoparticles with a diameter of ~11 nm were prepared and it was suggested that the small amount of cobalt in the nanoparticles enhances the magnetocrystalline anisotropy, owing to the increased coercivity of the cobalt ‘doped’ system compared with Fe_3O_4 .⁶⁶

Bonini *et al.* synthesized CoFe_2O_4 nanoparticles by two pathways: 1) a microemulsion method and 2) a supersaturation method. In the microemulsion method, 350 μL of an aqueous solution of 0.2 M $\text{Fe}(\text{NO})_3$ and 0.1 M CoSO_4 was added to an organic solution of 1g CTAB, 10 mL *n*-octane and 1 mL *n*-butanol. Another microemulsion containing 350 μL ammonium hydroxide and the same organic phase was prepared and the two microemulsions were mixed under agitation to afford ~ 7nm CoFe_2O_4 nanoparticles. In the supersaturation method, equal volumes of 0.66 M Fe^{+3} and 0.33 M Co^{+2} solutions were added to concentrated HNO_3 and boiled. Boiling 1 M NaOH was added and the solution was rapidly agitated, resulting in a magnetic precipitate. The precipitate underwent other work-up treatments to electrostatically stabilize the nanoparticles. A portion of the electrostatically stabilized nanoparticles was added to a water:2-propanol solution. NH_4OH and tetraethylorthosilicate were added under agitation (procedure repeated multiple times) to form a silica shell around the nanoparticles. Small angle x-ray scattering (SAXS) measurements indicated that the proposed silica shell was ~2.5 nm thick.⁶⁷ Crystalline information about the nanoparticles was not reported for either method; however, the stoichiometry of the reaction suggests that CoFe_2O_4 should be formed.

Ji *et al.* reported the synthesis of CoFe_2O_4 nanoparticles by hydrothermally treating a solution of CoCl_2 and FeCl_3 , with and without cetyltrimethylammonium bromide (CTAB), in an autoclave for 15 hours at 130°C. Particles generated without CTAB were irregular in shape; however, particles prepared with CTAB were anisotropic (‘nanorods’) with lengths of ~120 nm and diameters of ~25 nm.⁶⁸

1.4 Magnetism overview

To understand and appreciate the myriad applications for nanoscale magnetic materials, one must first understand the fundamentals of magnetism. Magnetism has been a unique and intriguing phenomenon since the discovery of lodestone (i.e. magnetite), the only naturally occurring magnetic material. Since the discovery of magnetite, magnetism has been exploited in disciplines ranging from mining (mineral separation) to medicine (magnetic resonance imaging or MRI). The following section will discuss the fundamentals of magnetism and the different classes of magnetic materials.

1.4.1 Fundamentals of magnetism

Magnetism and electricity were combined into the theory of electromagnetism primarily owing to the work of Faraday and Maxwell in the 19th century.⁶⁹ The idea that an electric current can generate a magnetic field is useful in explaining the origin of magnetism in materials. In terms of volume, matter is made principally of electrons. The movement of electrons around atoms explains how magnetism arises from matter. Electrons have a spin magnetic dipole moment (μ_s) and an orbital magnetic dipole moment (μ_{orb}). The spin magnetic dipole moment is an intrinsic property of an electron and is related to the spin angular momentum (S) by:

$$\mu_s = -\frac{e}{m} S \quad 1.4.1$$

where e and m are the charge and mass of an electron respectively. The spin angular momentum is quantized and can only be $\pm \frac{1}{2}$. Since only the z component of S can be measured, only the z component of μ_s can be measured from the following equation:

$$\mu_{s,z} = \pm \frac{eh}{4\pi m} \quad 1.4.2$$

where h is Planck's constant. The positive value of this equation, known as the Bohr magneton (μ_B), has a value of $9.27 \times 10^{-24} \text{ J T}^{-1}$.³⁷ The Bohr magneton is the fundamental unit in magnetism and magnetic materials are described in terms of this quantity. The orbital magnetic dipole moment arises from the movement of electrons around the nucleus of an atom. The spin magnetic dipole moment and the orbital magnetic dipole moment combine for each electron of an atom. The sum of this combination for each element determines what type of magnetism a material displays. There are six classifications of magnetic materials: 1) diamagnetic, 2)

paramagnetic, 3) ferromagnetic, 4) antiferromagnetic, 5) ferrimagnetic and 6) superparamagnetic. The following section will explain the differences between the various types of magnetism. As a prelude to the discussion of magnetic materials, a table listing the quantities and units used in magnetism is provided (Table 1.4.1).

Table 1.4.1 Table of quantities and units used in magnetism

Quantity	Symbol	Gaussian units	Conversion Factor	SI units
Magnetic flux density, magnetic induction	B	gauss (G)	10^{-4}	tesla (T)
Magnetic flux	Φ	Maxwell (Mx)	10^{-8}	weber (Wb)
Magnetic field strength	H	oersted (Oe)	$10^3/4\pi$	Ampere/meter (A/m)
Volume magnetization	$4\pi M$	G	$10^3/4\pi$	A/m
Mass magnetization	σ, M	emu/g	1	$A \cdot m^2/kg$
Magnetic moment	m	emu	10^{-3}	$A \cdot m^2$
Magnetic dipole moment	j	emu	$4\pi \times 10^{-10}$	Wb·m
Volume susceptibility	χ	Dimensionless	4π	Dimensionless
Mass susceptibility	χ_p	cm^3/g	$4\pi \times 10^{-3}$	m^3/kg

1.4.2 The Six Classes of Magnetic Materials

The magnetic properties of a material are governed by the electronic structure of the atoms within the material. Magnetic materials vary from very weakly magnetic (diamagnetic) to permanently magnetic (ferromagnetic). The most important property of a magnetic material is the magnetic susceptibility (χ):

$$\chi = \frac{M}{H} \quad 1.4.3$$

where M is the magnetization and H is the magnetic field, both of which have the units $A \cdot m^{-1}$. The magnetic susceptibility is different for each material and is temperature dependent (except for diamagnetic materials) as seen in the following equation:

$$\chi = \frac{C}{T \pm \theta} \quad 1.4.4$$

where C and θ are constants that differ for each material. ³⁷ Table 1.3.2 lists the primary differences between the classes of magnetic materials. Figure 1.4.1 shows the alignment of magnetic moments at room temperature for the different classes of magnetic materials.

Table 1.4.2 Description of classes of magnetic materials ³⁷

Class	Critical Temp.	Magnitude of χ	Variation of χ with T	Atomic structure
Diamagnetic	None	$\sim -10^{-6}$ to -10^{-5}	Constant	Atoms have no permanent dipole moment
Paramagnetic	None	$\sim 10^{-5}$ to 10^{-3}	$\chi=C/T$	Atoms have permanent dipole moments, but adjacent moments do not interact
Ferromagnetic	Curie Temp., θ_C	$> 10^{-3}$	Above θ_C , $\chi=C/(T-\theta)$ $\theta \approx \theta_C$	Atoms have permanent dipole moments and interact causing alignment (parallel)
Antiferromagnetic	Néel Temp., θ_N	$\sim 10^{-5}$ to 10^{-3}	Above θ_N , $\chi=C/(T \pm \theta)$ $\theta \neq \theta_N$	Atoms have permanent dipole moments and interact causing alignment (antiparallel)
Ferrimagnetic	Curie Temp., θ_C	$> 10^{-3}$	Above θ_C , $\chi \approx C/(T \pm \theta)$ $\theta \neq \theta_C$	Atoms have permanent dipole moments and interact causing uneven antiparallel alignment
Superparamagnetic	Curie Temp., θ_C	$> 10^{-3}$	Above θ_C , $\chi=C/T$	Atoms have permanent dipole moments and interact causing alignment

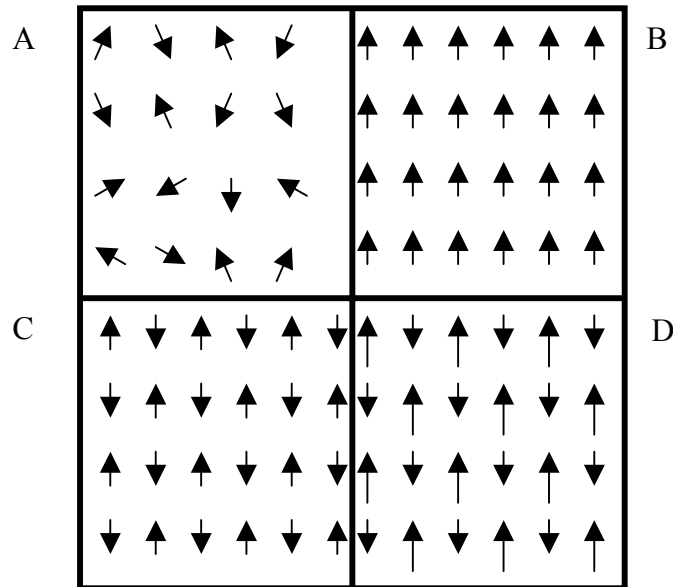


Figure 1.4.1 Schematic of magnetic dipole moment alignments in zero applied-field at room temperature for: A) paramagnetic or superparamagnetic material, B) ferromagnetic material, C) antiferromagnetic material and D) ferrimagnetic material.

1.4.2.1 Diamagnetism

The induction of a magnetic moment upon exposure to an external magnetic field defines diamagnetism. All materials are inherently diamagnetic. Materials that have filled electron shells exhibit no net spin magnetic dipole or orbital magnetic dipole and are classified as purely diamagnetic. However, materials that also have unfilled electron shells exhibit other types of magnetism that will outweigh the diamagnetic effects. Diamagnetic materials have a negative magnetic susceptibility (χ), because of the direction of the induced magnetic moment upon exposure to a magnetic field. This explanation is based on Lenz's law, which states that the magnetic field due to the current (of electrons) opposes the change in magnetic field, which induced the current.⁶⁹ Thus, when a diamagnetic material is exposed to an external magnetic field, the induced magnetic field is in the opposite direction. Figure 1.4.2 shows a magnetization vs. magnetic field plot for a Teflon sample holder used in this research. The negative slope of the curve in positive magnetic fields is indicative of a purely diamagnetic material. Note that the magnetization value is of the order of -10^{-5} to -10^{-3} , which is expected for purely diamagnetic materials.

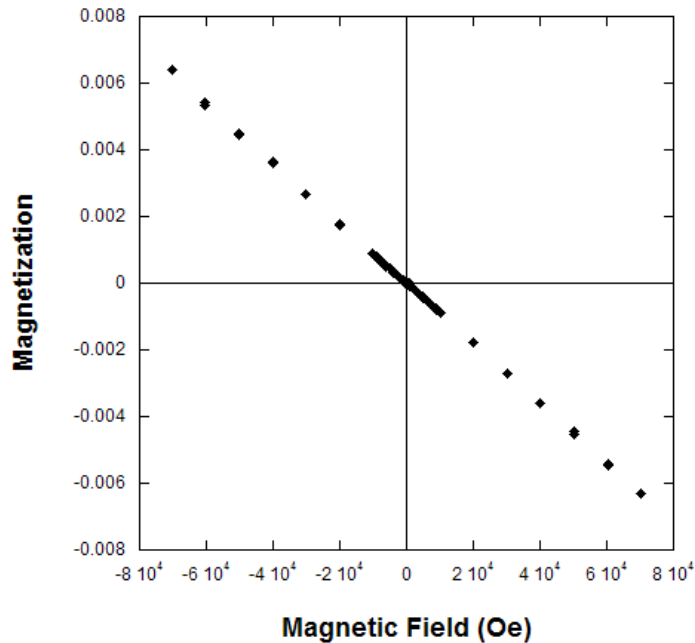


Figure 1.4.2 Room temperature M vs. H plot for a diamagnetic Teflon sample holder

1.4.2.2 Paramagnetism

Paramagnetism occurs in materials with permanent magnetic dipole moments, such as atoms or molecules with an odd number of electrons and atoms or ions with unfilled electron shells.⁷⁰ In zero applied magnetic field, the atoms randomly align to give a net moment of zero for the material. However, when exposed to an externally applied magnetic field, a small amount of magnetization occurs. The reason that only partial alignment occurs is explained by the inverse relation of χ with T : $\chi=C/T$. This relationship also explains the positive susceptibility of paramagnetic materials and is expressed more formally as:

$$\chi = \frac{c\mu_o Nm^2}{kT} \quad 1.4.5$$

where c is a constant, μ_o is the permeability of a vacuum, N is number of magnetic dipoles (m) per unit volume, k is Boltzmann's constant and T is the absolute temperature.³⁷ Equation 1.3.5 is called the Curie law and ideal paramagnetic materials obey this at most temperatures, except very low temperatures (< 5 K). The value of kT is the governing factor for the behavior of paramagnetic materials, as it is greater than the energy required to align magnetic dipole moments.⁶⁹ Figure 1.4.3 shows the temperature relationship for a sample containing a paramagnetic component. Notice the positive slope in high applied-fields at 5 K and the saturation effect in high applied-fields at 300 K.

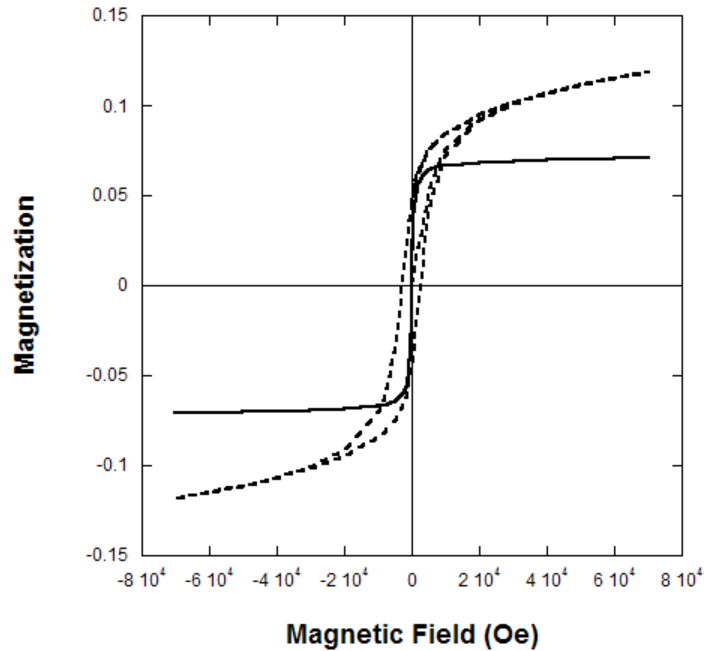


Figure 1.4.3 Magnetization vs. Magnetic Field plots for a material with a paramagnetic impurity at: 300 K (—) and 5 K (---)

1.4.2.3 Ferromagnetism

Ferromagnetism differs from the weaker diamagnetism and paramagnetism, in that the electrons of neighboring atoms interact with one another in a process called exchange coupling.

⁶⁹ Exchange coupling phenomena, caused by exchange fields, result in the magnetic dipole moments of atoms being aligned at room temperature despite the effect of kT . The most common ferromagnetic materials are zero-valent transition metals like Fe^0 , Co^0 and Ni^0 . Ferromagnetism is strongly temperature dependent, and the magnetization of a ferromagnetic material is inversely related to temperature by:

$$\chi = \frac{C}{T - \theta} \quad 1.4.6$$

where C is a constant and θ is close to the Curie temperature (θ_C) for the material. The Curie temperature is the temperature above which the exchange coupling ceases to be present. This means that above θ_C , a ferromagnetic material randomizes due to thermal energy as in paramagnetic materials. The expanded version of equation 1.4.6, called the Curie-Weiss law, is:

$$\chi = \frac{\mu_o N m^2 c / k}{T - \mu_o N m^2 c w / k} \quad 1.4.7$$

where C is defined by the numerator and θ is defined by the fraction in the denominator where w is called the exchange field coefficient.^{37, 70} Thus, ferromagnetic materials have their highest magnetization at 0 K and the magnetization decreases up to the Curie temperature where it disappears. Complete alignment of magnetic dipole moments (magnetic saturation) occurs readily for ferromagnetic materials. The Curie-Weiss law indicates that ferromagnetic materials have a higher χ than paramagnetic materials due to the subtraction of θ in the denominator. This increased χ enables a ferromagnetic material to become saturated in very low fields, sometimes less than 1 T.

Most ferromagnetic materials are comprised of magnetic domains. Magnetic domains are regions of a material where the magnetic dipole moments are aligned in one direction. An example of a region would be a single crystal within a polycrystalline sample. Magnetic energy minimization within a material causes the formation of magnetic domains. When domains are arranged such that the north pole of one domain is at the south pole of another and vice versa, the energy is decreased by $\frac{1}{2}$. Further application of this theory leads to the energy of a material decreasing by $1/N$ where N is the number of domains formed (Figure 1.4.4. A and B).⁷⁰ Domain wall is the term used to define the interfacial region between magnetic domains and the application of a magnetic field to a ferromagnetic material results in domain wall movement. Qualitatively, the domain walls move such that domains aligned in the direction of the applied field ‘grow’ and domains that are in other directions ‘shrink.’ The direction of the magnetic moments within domains that are not aligned in the direction of the applied field may also begin to rotate at significant field strengths (Figure 1.4.4. C and D). Nevertheless, the formation of magnetic domains is energetically unfavorable below a certain size, which is different for each material. In this case, the material is classified as single-domain. Single-domain particles are uniformly magnetized along an easy axis.⁷¹ The topic of single-domain particles in the superparamagnetic regime will be discussed further in section 1.4.2.6. For a more detailed account of magnetic domains the reader is referred to Morrish.⁷²

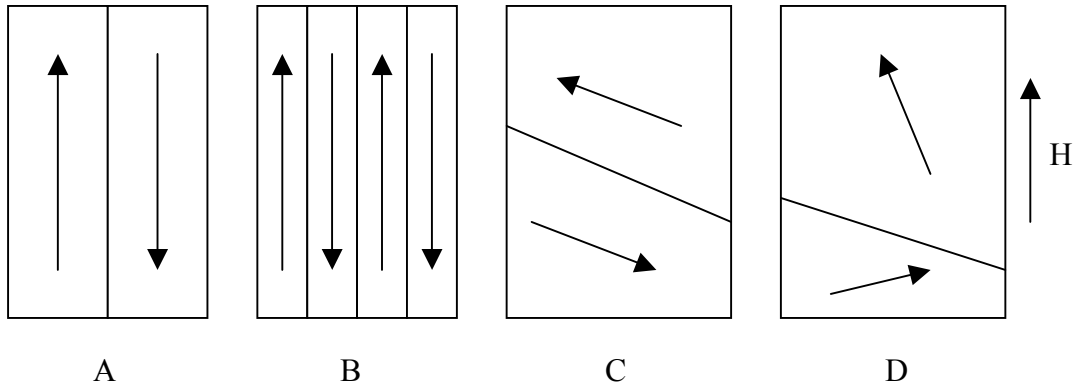


Figure 1.4.4 A) material with two domains has energy decreased by $\frac{1}{2}$, B) material with four domains has energy decreased by $\frac{1}{4}$, C) material in zero applied field and D) material in strong applied field

Since ferromagnetic materials are the most interesting magnetic materials in terms of their actual and potential applications, their properties need to be measured quantitatively. Hysteresis loop measurements reveal the magnetic properties of interest in magnetic materials. A hysteresis loop is measured by placing the sample in a magnetometer and measuring the response of the material (M or σ) with respect to the applied magnetic field (H). Several valuable quantities are obtained from hysteresis loop measurements: 1) M_S or σ_S , 2) M_R , 3) H_C and 4) H_E . The saturation magnetization (M_S) or specific saturation magnetization (σ_S) are values indicating the magnetization of a specimen when all of the magnetic dipole moments are aligned in the direction of the applied magnetic field. Magnetic remanence (M_R) is the magnetization of a sample in zero applied field. Coercivity (H_C) is the strength of the magnetic field needed to remove any remanent magnetization from a sample. The exchange bias field (H_E) denotes the shift of the center of a field-cooled hysteresis loop, brought about by the coupling of a ferromagnetic material with an antiferromagnetic material. The experiments involved with acquiring these data will be discussed in more detail in the experimental methods section.

1.4.2.4 Antiferromagnetism

Antiferromagnetic materials are characterized by having a weak magnetic susceptibility of the order of paramagnetic materials. Examples of antiferromagnetic materials are transition metal compounds and some transition metal oxides (CuCl_2 , CoO , NiO). Antiferromagnetic

materials are comprised of sublattices of atoms whose magnetic dipole moments are aligned antiparallel. The antiparallel alignment of magnetic dipoles in antiferromagnetic materials is complex and will not be discussed in detail. The antiparallel arrangement of magnetic dipoles in antiferromagnetic materials is the cause for the small magnetic susceptibility of antiferromagnetic materials. The temperature above which antiferromagnetic order ceases to exist is called the Néel temperature (θ_N). Above θ_N , antiferromagnetic materials have a slight positive magnetic susceptibility comparable to paramagnetic materials. Below θ_N , however, antiferromagnetic materials have a spontaneous magnetization ($H=0$) that causes the magnetic dipole moments of the sublattices to align antiparallel to each another. The reader is referred to Chapter 8 in Morrish for a more comprehensive and detailed discussion on antiferromagnetic materials.⁷²

1.4.2.5 Ferrimagnetism

Ferrimagnetic materials, like ferromagnetic materials, have a spontaneous magnetization below a critical temperature called the Curie temperature (θ_C). The magnitude of magnetic susceptibility for ferro- and ferrimagnetic materials is similar; however, the alignment of magnetic dipole moments is drastically different. The magnetic dipole moments in a ferrimagnetic material are divided into sublattices and are classified as a subset of antiferromagnetic materials. Each sublattice can be treated as a ferromagnetic material and the difference between the magnetic dipole moments for the sublattices results in the net magnetization for the ferrimagnetic material.³⁶ The difference between ferri- and antiferromagnetic materials is that either the magnitude or number of the moments of the sublattices is different.³⁷ Thus, the mathematical derivation for the magnetic susceptibility is complex and the reader is referred to³⁷ and Ch. 9 in⁷². Qualitatively, ferrimagnetic materials behave like paramagnetic materials at high temperatures ($\chi \sim T^{-1}$), while at temperatures below θ_C they have a spontaneous magnetization and are organized into magnetic domains.⁷³ Magnetic materials that fall into the classification are transition metal oxides like magnetite (Fe_3O_4) and mixed ferrites like cobalt ferrite (CoFe_2O_4).

1.4.2.6 Superparamagnetism

Superparamagnetic materials are a unique class of materials. Superparamagnetic materials are single-domain particles that behave like ferromagnetic materials below θ_C , because they have rather large susceptibilities, are saturated in moderate magnetic fields and display remanence and coercivity. Above θ_C , however, superparamagnetic materials behave like paramagnetic materials as they display no hysteresis (i.e. no magnetic remanence or coercivity).

³⁷ Superparamagnetic particles are uniformly magnetized along an easy axis and thermal energy causes the magnetization to switch between equivalent easy axes through an anisotropy barrier. This switching happens so quickly that the time average magnetic remanence is zero. Superparamagnetic particles align with an applied magnetic field by one of two mechanisms: 1) Néel rotation or 2) Brownian rotation. Néel rotation occurs when particles are in a fluid or the solid state and results from the rotation of the magnetic moment of a stationary particle. Brownian rotation only occurs when particles are in a fluid and results from the physical rotation of a particle towards the direction of the applied magnetic field.⁷⁴

CHAPTER 2. Physical Characterization of Magnetic Nanoparticles

This chapter will cover various analytical techniques used to characterize magnetic nanoparticulate systems. The first section discusses the operation of a transmission electron microscope (TEM) and the valuable information, such as images, diffraction patterns and spectra, obtained with this technique. The method discussed in the second section is x-ray diffraction (XRD). XRD provides the means for analyzing the crystal structure of a sample. When using electron diffraction with TEM, XRD is a complementary technique used to corroborate the crystal structure of a larger volume of a specimen. The third section on magnetometry discusses the use of magnetic susceptometry to understand the magnetic properties of magnetic nanoparticles. These properties include but are not limited to the saturation magnetization (σ_S or M_S), the remanence magnetization (M_R) and the coercivity (H_C). The final section is on small angle x-ray scattering (SAXS). SAXS is used to extract information related to the particle size and shape of a relatively large volume of sample, and is complementary to particle size analysis conducted from microscopic measurements.

2.1 Transmission Electron Microscopy

Transmission electron microscopy (TEM) is a fundamental technique used to characterize specimens in materials science. A TEM is very similar to an optical microscope (OM), in that radiation is emitted from a source and passed through a condenser lens until it interacts with the sample at or near the objective lens. After interacting with the sample, the radiation travels through a series of additional lenses to a viewing ‘screen’ where one can see the image. This ‘screen’ is the human eye for an OM and a fluorescent screen for a TEM (Figure 2.1.1). In OM the radiation is light and the lenses are glass, whereas in TEM the radiation is electrons and the lenses are electromagnetic. This section on TEM will give the reader a basic understanding of how a TEM operates and its capabilities.

The types of samples addressed in this section are magnetic nanoparticles; however, TEM is also used to analyze biological, geological and a variety of other specimens. Two TEMs were used in this research: 1) JEOL 2000 FX TEM operated at 80 kV and 2) JEOL 3000 F field-emission gun TEM operated at 300 kV. The JEOL 2000 FX microscope has a thermionic electron source and images and diffraction patterns are collected on film. The JEOL 3000 F microscope has a field-emission electron source, digital imaging system and Gatan image filter.

Images are collected with a charge-coupled device (CCD) camera; however, diffraction patterns must still be collected on film. It is important to understand the similarities and differences between these instruments; therefore, a detailed description of microscope operation is provided.

The first part of this section will give an overview of the fundamentals of TEM and a description of the microscope's components. The second part deals with electron-sample interactions, which give rise to images, spectra and diffraction patterns. The third part discusses limitations of TEM and the fourth and final part covers data acquisition, i.e. imaging, spectroscopy and diffraction. Recommended resources are mentioned throughout this section for the reader who desires a more in-depth explanation on the topics.

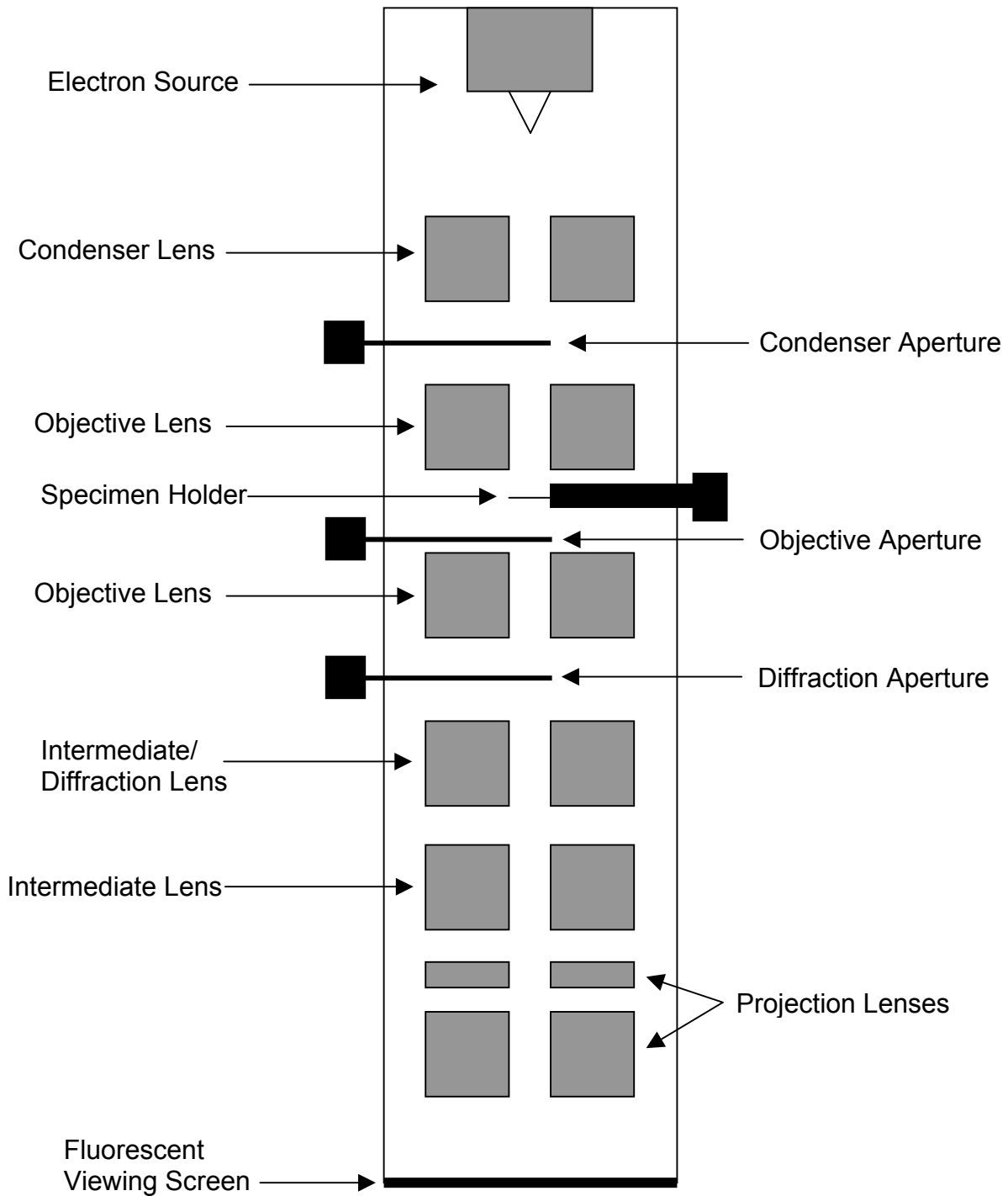


Figure 2.1.1 Schematic of a transmission electron microscope with the source, lenses and apertures labeled.

2.1.1 Fundamentals

A transmission electron microscope (TEM) uses electrons as the source of radiation compared to light (photons) used in optical microscopy (OM). The benefit of using electrons over photons is that the wavelength is much smaller. Visible light wavelengths vary from 400-700 nm, whereas the wavelength of electrons depends on the accelerating voltage. A field-emission TEM operating at 300 kV, generates electrons whose relativistic wavelength is 0.00197 nm with an energy spread of less than 0.5 eV.⁷⁵ The wavelength and energy spread have larger implications that will be discussed in later sections. A TEM can be broken down into three primary components: 1) the electron source, 2) the electromagnetic lenses with their respective apertures and 3) the projection chamber.

2.1.1.1 Electron Sources

In a TEM there are two types of electron sources: 1) thermionic source (JEOL 2000 FX) and 2) field-emission source (JEOL 3000 F).⁷⁶ Electrons are emitted from a thermionic source by heating the source (usually a tungsten filament or LaB₆ crystal), by the passage of an electrical current through the source, to a sufficient energy that allows the electrons to leave their respective atoms. The energy for an electron to leave an atom is referred to as the work function (Φ) and can be calculated from Richardson's law (equation 2.1.1) where J is the current density from the source, A_R is Richardson's constant, T is the absolute temperature in K, Φ is the work function and k is Boltzmann's constant.⁷⁶

$$J = A_R T^2 e^{-\Phi/kT} \quad 2.1.1$$

The thermionic source is known as a triode gun, since it is comprised of a cathode (emission source), an anode and a Wehnelt cap (Figure 2.1.2).

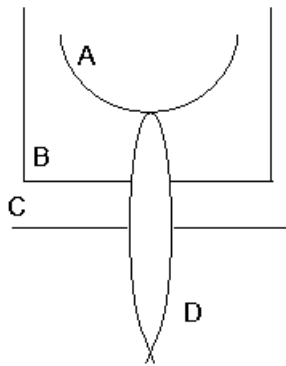


Figure 2.1.2 Diagram of thermionic emission gun. A) cathode or emission source, B) Wehnelt cap, C) anode and D) electron beam.

The cathode is held at a high negative potential with respect to the anode, which allows for a rapid acceleration of the electrons across a large potential towards the anode to generate an electron beam.⁷⁵ The Wehnelt cap is held at a slightly more negative potential than the cathode and controls the diameter of the electron beam leaving the cathode. The difference in potential between the cathode and anode is what defines the accelerating voltage of a microscope, and hence the energy of the electrons.

The field-emission source (zirconia coated tungsten crystal) differs from the thermionic emission source, as it relies on quantum tunneling of electrons to generate an electron beam. A large electrical current ($> 10^9$ V/m) is passed through the source to increase the probability of an electron leaving the surface without requiring the energy specified by the work function for that material.⁷⁵ Once the electrons leave the surface of the source (cathode) they are pulled away by an extraction anode. The potential between the cathode and the extraction anode is only a few kilovolts. However, once the electrons reach the extraction anode they are accelerated down the column of the microscope by the acceleration anode (Figure 2.1.3). The potential difference between the extraction anode and the acceleration anode is approximately 100-300 kilovolts. For field-emission to occur, the electron source must be perfect. That is, no contaminants can be in the column to interfere with this delicate source. For this reason, the field-emission microscopes are kept under a very high vacuum (10^{-8} Pa) compared with thermionic microscopes ($10^{-2} - 10^{-4}$ Pa). It should be noted that there are two types of field-emission electron guns. The first is

called the cold field-emission gun and relies on ‘extracting’ electrons from the source at room temperature. Alternatively, thermal field emission (Schottky emitters) (JEOL 3000 F) can be used which effectively combines the thermionic emission process with the field-emission process, but not at the temperatures required for pure thermionic emission.⁷⁶

Once the electrons have been emitted or extracted from the source, they are sent down the microscope column at a certain accelerating voltage governed by the potential difference between the cathode and anode. The next section will discuss the ways that the electron beam is manipulated with electromagnetic lenses to generate images and diffraction patterns.

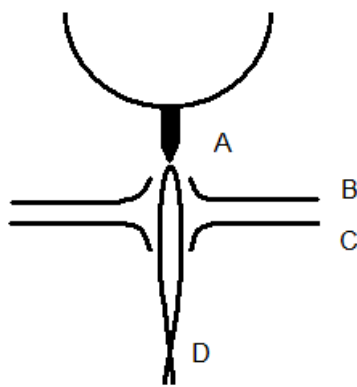


Figure 2.1.3 Diagram of field-emission gun: A) emission source or cathode, B) extraction anode, C) acceleration anode and D) electron beam.

2.1.1.2 Electromagnetic Lenses

Electromagnetic lenses in a TEM serve to manipulate the electron beam that is traveling vertically down the microscope column. Electromagnetic lenses are constructed of polepieces and a coil of copper wire. The polepieces are made of a soft magnetic material such as iron and in most polepieces there is an upper and lower polepiece. Electrons travel through a hole or ‘bore’ that is drilled through each polepiece. The distance between polepiece faces is called the gap and the bore/gap ratio controls the ability of a lens to focus.⁷⁶ When a current is passed through the copper coil, a magnetic field is generated in the bore. Electrons passing through the bore are affected by the magnetic field within the bore, since electrons have spin angular momentum. By changing the current through each lens, the magnetic field strength can be varied and hence the focal length can be precisely controlled.⁷⁵ There are four types of lens systems within a TEM: 1) condenser lens(es), 2) objective lens, 3) intermediate lens and 4)

projector lens(es). Each lens or set of lenses serves a different purpose, which will be expanded upon in the following sections.

2.1.1.2.1 Condenser Lens System

Two or more condenser lenses are usually found below the emission source in a TEM. The condenser lenses demagnify the electron beam as it travels from the emission source towards the sample. These lenses are used to control the diameter of the beam (hence the intensity), and can be referred to as the ‘brightness’ control for the microscope. A condenser aperture is used to decrease the electron beam intensity by permitting only electrons within a certain range of angles to continue down the microscope column. The two-lens condenser system is popular in microscope design and the reader is referred to ^{75, 77} for a more detailed discussion on the operation of this system.

2.1.1.2.2 Objective Lens System

The most versatile type of objective lens is a called a split polepiece objective lens. The upper and lower poles of this lens can be adjusted to different strengths to achieve different goals. In addition, there is room for the sample to be inserted between the two poles along with the objective aperture. This sample placement is advantageous for: 1) X-ray analysis, since the detector can be placed close to the specimen to detect emitted X-rays(TEM, Basics, 92) and 2) tilting, as the sample chamber is large enough to tilt the sample in two directions. Primarily, the objective lens is used to form a focused image of the specimen being analyzed. However, given that the different poles can be adjusted to different strengths, the objective lens also serves to magnify the image of the sample from 50 to 100 times. ⁷⁸ A series of objective apertures can be inserted to control the range of scattered electrons that form an image. The diameter of the objective aperture governs the final resolution of the image based on equation 2.1.2, where r is the resolution, λ is the wavelength of the electrons and α is the half-angle created by the aperture.

⁷⁵

$$r = \frac{0.61\lambda}{\alpha} \qquad \qquad \qquad 2.1.2$$

Thus, for increasing aperture size (large α), the r becomes smaller leading to improved resolution. Furthermore, the objective aperture is used to control image contrast by removing

strongly scattered electrons. Once an objective aperture is inserted, the regions in an image with higher contrast usually contain materials with higher Z elements that strongly scatter the electrons. This type of contrast is called mass-thickness contrast and will be discussed further in the section on imaging.

The JEOL 3000 F has improved resolution over the JEOL 2000 FX, because the field-emission source operated at 300 kV generates electrons with a smaller wavelength and wavelength spread than the thermionic source operated at 80 kV. Although the resolution of a TEM is much better than that of an optical microscope, it is still not capable of achieving the theoretical limits. This is due to imperfections in the man-made materials that comprise the lenses of the microscope. These imperfections lead to two types of aberrations: chromatic and spherical. Chromatic aberration occurs when electrons of different wavelengths pass through an electromagnetic lens and are focused at different points. There are two ways to minimize chromatic aberration: 1) use an electron source with minimal energy spread, i.e. a field-emission source, and 2) analyze a very thin sample to minimize energy loss. Spherical aberration occurs when electrons travel through a lens at different distances away from the center of the lens and are focused at different distances away from the lens. Apertures are used to minimize the spherical aberration by limiting the distance that electrons are from the center of a given lens, resulting in electrons that are focused at a single distance away from the lens.

2.1.1.2.3 Intermediate Lens System

The intermediate lens is positioned after the objective lens in the column of the microscope. The intermediate lens operates in two modes: 1) image mode or 2) diffraction mode. When in image mode, the lens focuses on the image plane of the objective lens. Subsequent projector lenses then control the final magnification of the image. However, when the intermediate lens is in diffraction mode, it focuses on the back focal plane of the objective lens and the diffraction pattern is then projected to the final projector lenses which control the final magnification of the pattern (camera length is the term used for magnification in diffraction patterns).^{75, 76} The aperture associated with this lens system is called the selected area diffraction (SAD) aperture, since only the area selected by the aperture is analyzed.

2.1.1.2.4 Projector Lens System

A series of projector lenses following the intermediate/diffraction lens magnify the image/diffraction pattern to what one sees on the fluorescent screen. The projector lenses can be turned on and off depending on the desired magnification: off for low magnification and large field of view or on for high magnification and high-resolution imaging. When all of the projector lenses are in use, final magnifications of > 1 million times are achievable with current microscopes. This magnitude of magnification enables the imaging of lattice fringes that are on the order of angstroms.

2.1.2 Electron-sample interactions

As the electron beam travels down the microscope column, it interacts with the sample before an image is formed on a fluorescent screen or CCD camera. The interaction of electrons with matter is a subject unto itself and this section will focus on the interactions applicable to transmission electron microscopy.

A wide variety of radiation is emitted/transmitted when the primary electron beam hits the sample. Figure 2.1.4 is a schematic of an incident electron beam interacting with a sample and shows the variety of radiation emitted. X-rays can be useful when performing energy dispersive x-ray spectroscopy; however, in TEM the elastically and inelastically scattered electrons are of primary interest. Electrons scatter upon hitting a sample, because they interact with either nuclei of atoms and/or the electron clouds around them. Incident electrons that interact electrostatically with the sample and lose little or no energy are termed elastically scattered electrons. Elastically scattered electrons are used for imaging and diffraction in TEM. Inelastically scattered electrons, which are used for various types of spectroscopy, lose energy as a result of interacting with the sample.⁷⁵

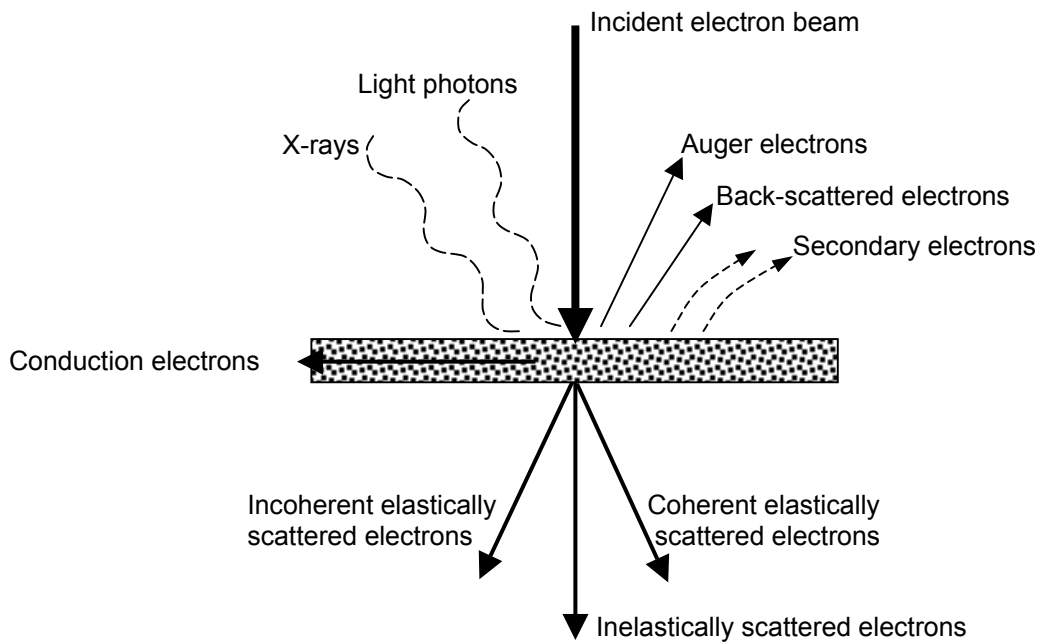


Figure 2.1.4 Schematic of electrons from primary beam of TEM interacting with sample

2.1.3 Limitations and difficulties with TEM

Although TEM is an vital technique used to characterize a wide variety of materials, it does have limitations. These limitations will be divided into two categories: 1) specimen limitations and 2) sampling limitations.

2.1.3.1 Specimen Limitations

Sample preparation is crucial in TEM analysis. Several factors need to be considered when preparing the sample: 1) how does one mount the sample, 2) will the sample be sensitive to the electron beam 3) how thick is the sample and 4) will the sample preparation method alter the sample.

Sample mounting can be achieved in several ways. When looking at small particles, it is recommended that the particles be dispersed in solvent to a very weak concentration. A drop of this dispersion is then placed onto an amorphous carbon coated copper grid and the solvent is allowed to evaporate. If a sample tends to be sensitive to the electron beam, it can be embedded

in a resin. The resin is then crosslinked under heat and the sample is microtomed. A microtome uses a very sharp diamond knife to slice thin sections (~50-150 nm) of a specimen, which are subsequently placed onto a copper grid for analysis. Two things to consider when embedding and microtoming a sample are: 1) will the embedding process alter the sample and 2) how thick will the microtomed sample be. The embedding process may alter the sample depending on the nature of the sample. If it is a mineral, the chances of disturbing the sample are small. However, if the sample is a polymer, there is a good chance that the embedding procedure will alter the sample since it involves chemically reactive polymers and solvents. Finally, specimen thickness should be < 150 nm to minimize energy loss, which can result in decreased resolution.

2.1.3.2 Sampling Limitations

Although the TEM is a robust instrument in terms of what it can analyze, it does have limitations. The primary reason for using a microscope is to observe objects that cannot be viewed with the naked eye. This primary reason introduces one of the largest limitations of TEM, which is small sampling volume. When analyzing a sample with TEM it is wise to evaluate the entire sample grid to ensure that the images being recorded are representative of the entire sample. Otherwise, one can make inaccurate conclusions about the size, morphology, crystallinity or chemical composition of a sample. When using TEM to analyze the size of a sample, in particular small particles, it is pragmatic to use another technique to corroborate the TEM data. Such techniques would be scattering techniques like small angle X-ray scattering (SAXS) or dynamic light scattering (DLS). Scattering techniques sample a larger volume of the specimen and give information about the bulk properties of sample.

The previous sections facilitated the understanding of TEM operation, electron-specimen interactions and TEM limitations. The remaining sections will focus on the myriad uses of TEM to extract a great deal of information from a specimen.

2.1.4 Data Acquisition with TEM

A variety of types of data can be acquired using transmission electron microscopy (TEM). These types of data include images, diffraction patterns and spectra depending on how the microscope is configured. This vast amount of data provides the user with information

related to the size, morphology, chemical composition and crystallinity of the specimen being analyzed.

2.1.4.1 Imaging

Imaging in TEM is a consequence of contrast within a sample. Contrast results from scattering of the incident electrons with the sample. There are two types of contrast in TEM: 1) phase contrast and 2) amplitude contrast. Phase contrast occurs when electrons of different phases (wave character of electron) pass through the objective aperture. When electrons with different phases interfere they create fringes, which are utilized mainly in high-resolution TEM (Section 2.2.4.1.2).⁷⁵ Amplitude contrast is comprised of two types of contrast: 1) mass-thickness contrast and 2) diffraction contrast.

Mass-thickness contrast evolves from incident electrons interacting with high or low atomic number (Z) elements and from passing through thick or thin samples. Mass-thickness contrast is the primary form of contrast in amorphous samples. The electrons are described as incoherent elastically scattered electrons since they are out of phase with one another owing to the 'random' arrangement of atoms within an amorphous sample. High Z elements scatter electrons more strongly than low Z elements; therefore high Z or 'electron dense' elements appear darker than low Z elements. Sample thickness also affects contrast, since the thickness of a sample governs the probability of scattering events. If sample thickness varies, contrast arises owing to the increased probability of scattering in the thicker section leading to stronger contrast. A thinner section will scatter less and result in weaker contrast.⁷⁹ Ultimately, it is not possible to differentiate between contrast that arises from mass or thickness variations and the term mass-thickness contrast is used to jointly describe these phenomena.

Diffraction contrast arises from the coherent elastic scattering of electrons in a crystal. Atoms within a crystal lie in a well-defined lattice. When the incident electron beam interacts with a specific lattice plane, the resulting electrons will still be 'in phase' or coherent owing to the periodic spacing of atoms within the lattice. Some regions of a crystal will appear darker than others, depending on the orientation of a crystal with respect to the incident electron beam. Tilting the specimen will result in changing which regions are darker, since the orientation of the crystal has been changed with respect to the electron beam.

2.1.4.1.1 Bright field imaging

Bright-field imaging in TEM relies on mass-thickness contrast to view a sample. Strongly scattered electrons are removed by using apertures and the resulting image is a result of weakly scattered or unscattered electrons. Bright-field images are what one uses to study the size and morphology of ‘macroscopic’ components of a sample. The term ‘macroscopic’ is used loosely, as it only means large with respect to the Angstrom. Strongly scattered electrons that are removed by apertures in bright-field imaging are utilized in a technique termed dark-field imaging. This topic, however, will not be discussed and the reader is referred to texts by Goodhew *et al.*, Buseck *et al.* and Spence for a discussion of dark-field imaging.^{75, 80-82}

2.1.4.1.2 High-resolution imaging

To fully understand high-resolution (HR) imaging, one needs first to understand resolution. Resolution is defined as the smallest distance between two objects where one can still differentiate between those objects. The theoretical resolution of an electron microscope was described in equation 2.1.2. For microscopes with an accelerating voltage of 300 kV, this resolution is much smaller than the size of an atom. Thus, to obtain high quality HR images, a microscope with a high accelerating voltage is recommended.

A surprising amount of information can be extracted from high-resolution images. The lattice fringes of a high-resolution image of a crystal have a periodic spacing. Fourier transforming the image creates a representation of the image in reciprocal space. This Fourier transform is similar to a diffraction pattern, since it represents all of the repeating frequencies within a high-resolution image (Figure 2.1.6). Measurements of the intense spots in the Fourier transform are equivalent to measuring reflections that would be seen in an electron diffraction spot pattern.

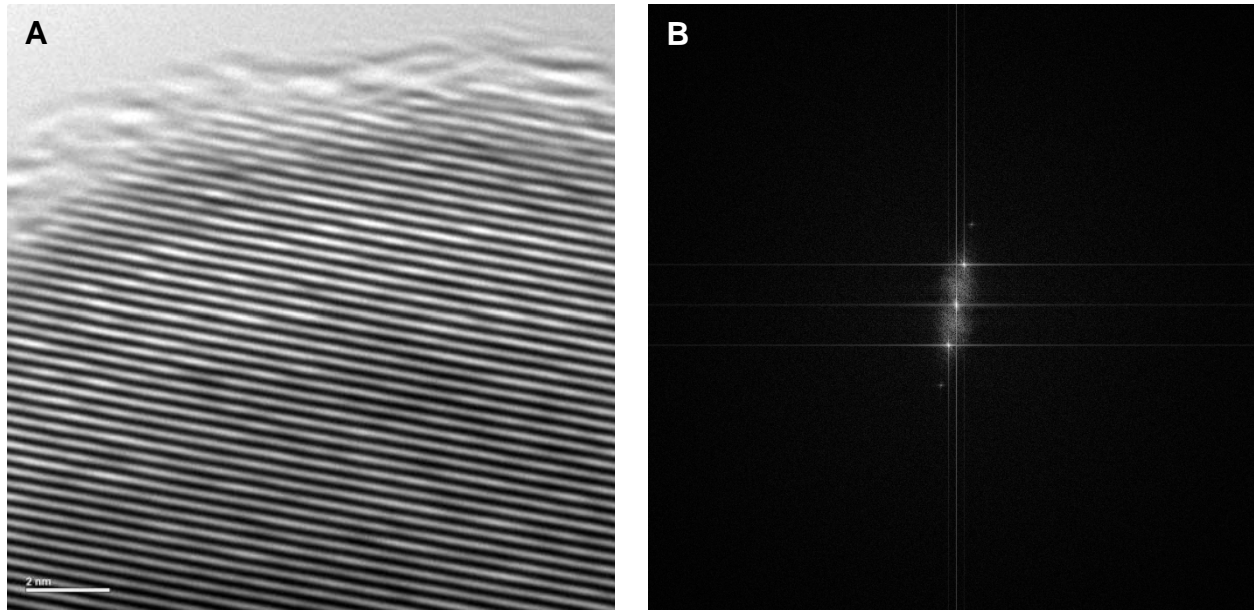


Figure 2.1.5 A) high-resolution image and B) corresponding Fourier transform indicating the repeating frequencies in the image.

2.1.4.2 Spectroscopy

This section will focus on two types of spectroscopy used in TEM analysis: electron energy loss spectroscopy (EELS) and energy dispersive X-ray spectroscopy (EDX). EELS is a technique that exploits inelastically scattered electrons to learn about the chemical composition of a sample. EDX also provides chemical information about a sample, but through a different mechanism. As discussed in section 2.2.2, X-rays are one form of radiation given off by the interaction of an incident electron beam with a specimen. X-rays have characteristic energies for each element, and are therefore useful for determining elemental composition.

2.1.4.2.1 Electron Energy Loss Spectroscopy (EELS)

Electrons that scatter inelastically from a sample lose a certain amount of energy depending on the element and the energy level of the electron with which they interact. An EELS spectrometer is a magnetic prism spectrometer, with an energy resolution of approximately 1 eV.⁸³ A spectrometer known as a Gatan image filter (GIF) will be the focus of this section. The GIF is situated underneath the viewing screen in a TEM, so the viewing screen needs to be lifted in order for the spectrometer to work. As electrons that have interacted with

the sample travel down the column, they enter the spectrometer. The spectrometer ‘bends’ or deflects the electrons at an angle $\geq 90^\circ$. Electrons with a significant energy loss are deflected more than electrons with little or no energy loss. The benefit of using a GIF is that it gives the user capabilities of either looking at electron energy loss spectra and/or energy filtered images. EELS spectra will be discussed in this section, with the following section focusing on energy-filtered imaging.

The electron energy loss spectrum can be divided into three main categories: 1) the zero-loss peak, 2) the low-loss spectrum and 3) the high-loss (core-loss) spectrum. EEL spectroscopy can be conducted both qualitatively and quantitatively. This section will only discuss qualitative EELS.

The zero-loss peak is caused by elastically scattered electrons or electrons that have lost minimal energy due to inelastic scattering events. This peak is the largest and most troublesome peak, as it may sometimes overlap with the low-loss part of the spectrum effectively masking any information contained therein.

The low-loss portion of the spectrum ranges from a few eV up to ~ 50 eV. The main contributors to the low-loss spectrum are plasmons and inter- and intra-band electron transitions.⁸³ A note on terminology must be discussed here. When referring to a plasmon peak in an EELS spectrum, the peak is a result of an electron losing energy by generating a plasmon in the sample, rather than the spectrometer registering a plasmon. There can be multiple peaks due to plasmon losses, because an incident electron can scatter multiple times. To decrease the effect of plural and multiple scattering, the sample should be thin, i.e. a decreased mean-free path. Inter- and intra-band transitions occur when an incident electron transfers the required energy to promote an inner shell electron to an outer shell. These types of transitions, if intense enough, may then be compared to a database of electronic fingerprints of known samples.

The electron energy loss spectrum from 50 eV to ~ 2 keV is called the high-loss or core-loss spectrum. When an incident electron interacts with a core electron with sufficient energy to eject the electron, the resulting atom becomes ionized. The incident electron that caused the ejection lost a specific amount of energy, depending on the shell location (K, L, M, etc., where K = 1s, L = 2s and 2p, M = 3s, 3p, 3d, etc.) of the electron that was ejected. Therefore, electrons that lose energy due to core-shell ionization processes are useful in determining the elemental composition of a sample. Since ionization happens at defined energies, the ionization edges of

the spectrum are sharp. Much information is available near the ionization edges and two techniques take advantage of the edges to provide detailed information about a sample. A technique called energy loss near edge structure (ELNES), is useful within 30 eV of the edge onset and provides information on bonding. Extended energy loss fine structure (EXELFS) utilizes information that is more than 50 eV away from the edge onset to give details on nearest neighbor distances.

2.1.4.2.1.1 Energy filtered imaging

Energy filtered transmission electron microscopy (EFTEM) utilizes the information obtained from an EEL spectrometer to generate an image instead of a spectrum. This is done by first defining the ionization edge for a particular element in the EEL spectrum. Next a series of EEL images are taken, utilizing electrons of specified energies, before (pre-edge) and after (post-edge) the ionization edge. The Gatan software package extrapolates the background from two pre-edge images past the post-edge image. The background is then subtracted from the post-edge image and the resulting elemental distribution image is due only to electrons that have lost the amount of energy defined by the ionization edge under investigation.⁸⁴ This technique is also called ‘elemental mapping,’ since the energy filtered image can be compared with a bright-field image of the same section to determine the distribution of selected elements within the image. For example, the L_3 - and L_2 -edges of cobalt are at 779 and 784 eV respectively. The slit width of the spectrometer is set at 40 eV, with the selected energy at the center of the slit. The first pre-edge image is acquired at 714 eV, which covers the energy range from 694 eV to 734 eV. The second pre-edge image is acquired at 754 eV, which covers the energy range from 734 eV to 774 eV. The post-edge image is acquired at 799 eV, which covers the energy range from 779 eV to 819 eV. The L_3 -edge onset is at ~ 779 eV, so the post-edge image contains both the L_3 and L_2 edges of cobalt. The background is extrapolated from the two pre-edge images as shown in Figure 2.1.6. Background subtraction from the post-edge image generates the cobalt map.

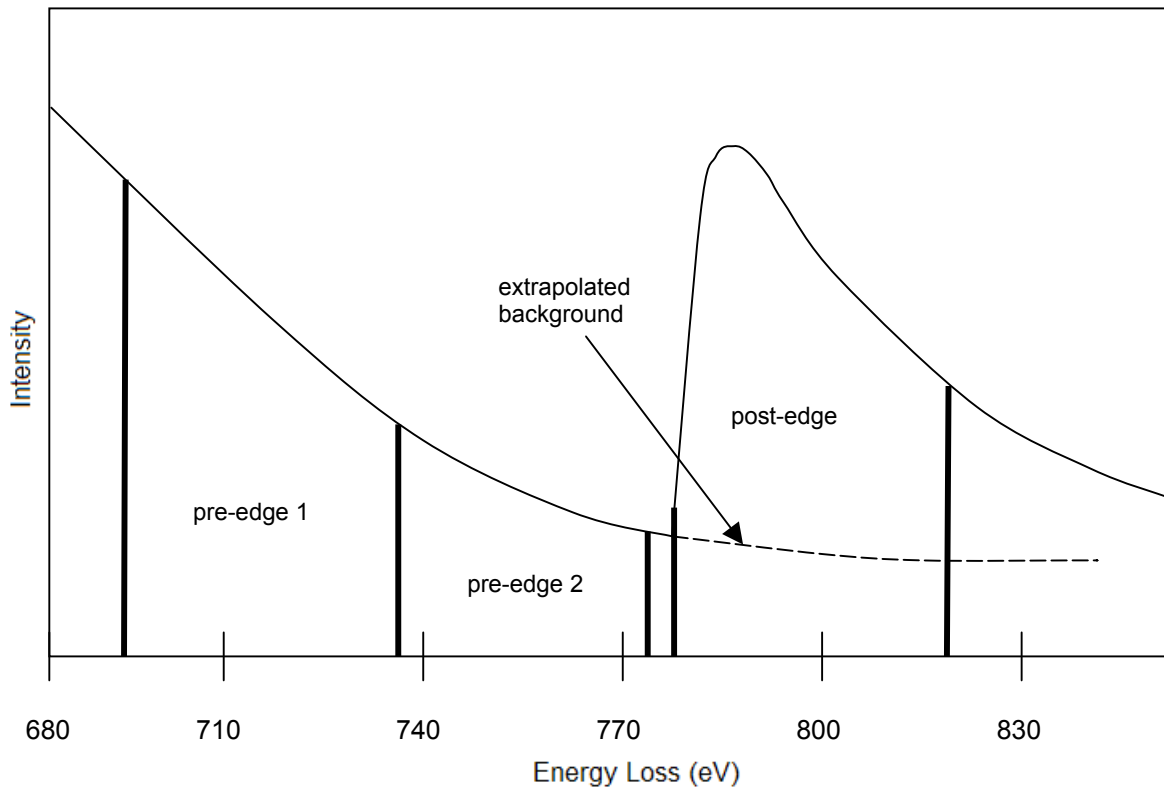


Figure 2.1.6 Electron energy-loss spectrum indicating energy ranges where energy-filtered images are acquired.

2.1.4.2.2 Energy Dispersive X-ray Spectroscopy (EDX)

Energy dispersive X-ray spectroscopy (EDX) makes use of X-rays emitted from electron-sample interactions to determine the chemical composition of a sample. The EDX spectrometer is placed close to the sample to maximize the X-ray signal reaching the detector. An EDX spectrum is comprised of peaks of varying energies. Since X-rays have specific energies that correspond to each element, the peaks in the EDX spectrum are used to identify elements within a sample. For further information on EDX, the reader is referred to Chapter 4 in Shindo⁸⁴.

2.1.4.3 Electron Diffraction

Electron diffraction is employed to study the crystallinity of a sample. Diffraction is another term for scattering used when looking at crystals comprised of periodically spaced atoms. While imaging techniques exploit the particle nature of an electron, diffraction exploits the wave nature of an electron. Diffraction patterns are effectively interference patterns, where

the intense spots or rings are caused by the constructive interference of electrons, while the dark regions result from the destructive interference of electrons. Diffraction provides significant information about a sample. It can be used to tell if a sample is amorphous or crystalline (single crystal or polycrystalline). If a sample is crystalline, the crystal structure and lattice parameters for the specimen can be determined by analysis of the diffraction pattern. Electron diffraction, like X-ray diffraction, is governed by Bragg's law:

$$n\lambda = 2d_{hkl} \sin(\theta_B) \quad 2.1.3$$

where n is an integer, λ is the wavelength of the electron beam, d_{hkl} is the interplanar atomic spacing and θ_B is the Bragg angle (Figure 2.1.7). Sets of atomic planes within a crystal will cause constructive interference (diffraction) if the incident electron beam hits them at the Bragg angle. Atomic planes, from which d_{hkl} values are determined, are indexed using conventional Miller index notation.^{70, 85}

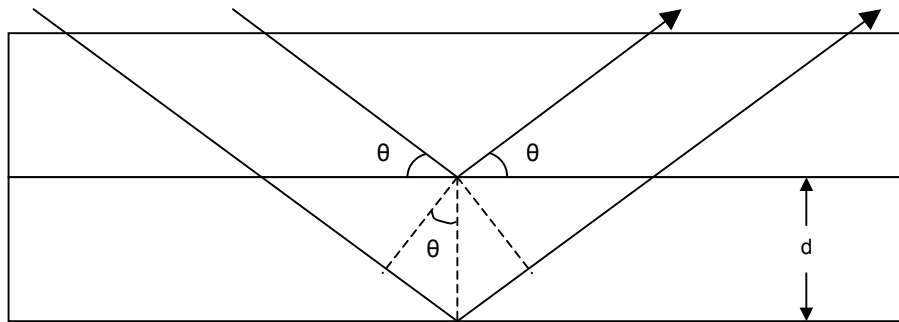


Figure 2.1.7 Schematic of incident electrons diffracting from lattice planes

Two types of diffraction patterns can be acquired with a TEM: 1) selected area electron diffraction patterns and 2) convergent beam electron diffraction patterns.

2.1.4.3.1 Selected area electron diffraction

Selected area electron diffraction (SAD) is conducted on a TEM by removing the objective aperture (located in the back focal plane of the objective lens) and inserting an SAD aperture. The SAD aperture is located in the image plane of the objective lens and is smaller in diameter than an objective aperture. The aperture selects an area for which a diffraction pattern is desired.^{76, 86} To obtain an SAD pattern there are three steps to follow: 1) remove the objective

aperture and insert the desired SAD aperture, 2) put the microscope in diffraction mode and 3) focus the diffraction pattern using the brightness control and the diffraction focus control. Once these steps are taken, the pattern is collected on film for analysis.

A diffraction pattern results from the angular distribution of electrons that have been scattered by a crystalline specimen. Electrons that scatter at small angles (large d-spacings) result in rings or spots close to the center of the diffraction pattern, while electrons that scatter at larger angles (small d-spacings) create rings or spots further out from the center. There is an inverse relationship between scattering angle and d-spacing; a smaller scattering angle is a result of a large d-spacing and vice versa. Scattering angle increases going out from the center of a diffraction pattern, and hence the calculated d-spacings decrease.

Diffraction patterns can consist of rings or spots depending on the sample. The diffraction pattern of a single crystalline particle will result in a spot pattern where each spot is due to a particular lattice spacing. As the number of particles being analyzed increases, the number of spots for each lattice spacing increases. The diffraction spots for a group of particles are distributed radially, as the orientation of each particle with respect to the electron beam is not necessarily the same. If enough particles are analyzed these radially distributed spots will form a ring.

The analysis of a diffraction pattern can be complicated if the material is unknown. However, if the identity is known, measurements of rings or spots can be made and compared to literature values for known phases of a material. Analyzing a ring pattern involves measuring the radius of each ring from the center of the diffraction pattern. To obtain exact d-spacings from a diffraction pattern the camera length (term used for magnification) must be known precisely. Combining the equation for the camera length (equation 2.1.4),

$$\tan 2\theta_B = \frac{R}{L} \quad 2.1.4$$

where R is the radius of a ring and L is the camera length, with Bragg's law (equation 2.1.3) gives the user a simple equation to calculate d-spacings (equation 2.1.5).

$$d_{hkl} \approx \frac{\lambda L}{R} \quad 2.1.5$$

If the camera length is not known precisely or if the sample height is not eucentric, ratios between spots or rings can be calculated. The ratios between spots or rings are constant

irrespective of camera length or focus. Ratios calculated from an experimental diffraction pattern can be compared with literature ratios of suspect materials to determine the sample structure. Analyzing a zone axis pattern is easier and provides more information than a ring pattern. A zone axis pattern is obtained when a crystal is oriented such that the electron beam interacts with one of the zone axes present within the crystal. If a crystal is not on a zone axis, the sample can be tilted until a zone axis is located. This is easily done by following Kikuchi lines; however, a detailed discussion on Kikuchi lines are outside the scope of this section. A zone axis pattern is similar to a spot pattern, but with limited reflections defined by the particular zone axis. Diffraction spots (or ratios) are measured similar to rings and d-spacings can be easily calculated. Angles between spots can also be measured, which provides more concrete information for determining the exact zone axis of a particular crystalline specimen.

2.1.4.3.2 Convergent beam electron diffraction (Nanodiffraction)

Convergent beam electron diffraction, unlike SAD, uses a focused beam of electrons to generate a diffraction pattern. The resulting pattern is comprised of discs, instead of spots typically seen in SAD patterns (Figure 2.1.8). With improving technologies, focused electron beam diameters can be of the order of 1 to 2 nm leading to the new term ‘nanodiffraction.’ Using a focused electron beam between 1 to 2 nm in diameter, one can probe the variations in crystal structure within single nanoscale crystals. The electron beam is focused into the smallest point using the objective lens and onto a crystalline specimen. Then, the microscope is put into diffraction mode and discs appear on the fluorescent viewing screen. Discs are created, because the electrons are arriving at the sample with a range of angles. Each angle at which electrons arrive at the sample generates a spot pattern. The spot pattern for each angle is in the form of a disc, as the electron beam is circularly focused.⁸⁷ Therefore, a large amount of information is contained within the discs; however, the discs can also be treated as individual spots as in SAD. The study of information contained within individual discs is an art unto itself and the reader is referred to two references by Cowley for more information on detailed convergent beam electron diffraction pattern analysis.^{88, 89}

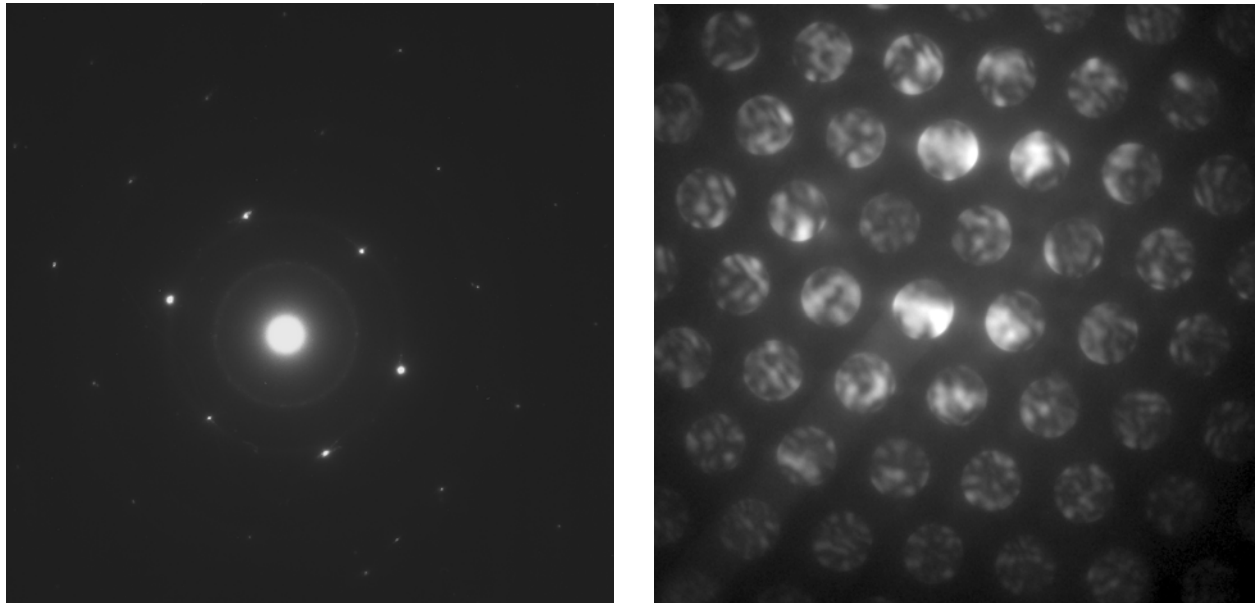


Figure 2.1.8 A) Selected area diffraction spot pattern and B) Nano-beam electron diffraction pattern

2.2 X-ray diffraction

X-ray diffraction (XRD) is a complementary analytical technique to electron diffraction. One limitation of electron diffraction (SAD or NBD) is small sampling volume. If several electron diffraction patterns are not collected across the entire specimen, it is difficult to make a claim about the crystallinity of the bulk of the sample. X-ray diffraction, however, analyzes milligrams of sample (billions of particles in the 1 to 100 nm range) while electron diffraction may analyze micrograms (thousands of particles in the 1 to 100 nm range). Using XRD in combination with electron diffraction allows one to corroborate data acquired with both techniques.

An X-ray diffractometer utilizes some of the fundamental operations of a transmission electron microscope, so a useful analogy can be made. In an X-ray diffractometer, x-rays are generated within an evacuated tube and exit through a window composed of a light element, usually beryllium. Inside of the tube, a current is passed through a filament (usually tungsten) to generate electrons.⁶⁹ These electrons are then accelerated through a potential difference towards

a metal target, such as copper. When the incoming electrons have sufficient energy to eject electrons from the core-shell (K shell) of copper, a characteristic spectrum is created. The characteristic spectrum is composed of discrete energies, which occur due to x-rays emitted by the 'falling in' of electrons to replace the ejected electron. Electrons 'falling in' from the L shell into the K shell give rise to copper $K\alpha$ peaks, electrons from the M shell give $K\beta$ peaks and electrons from the N shell give $K\gamma$ peaks. $K\alpha$ and $K\beta$ peaks are the most prominent peaks in the characteristic spectrum and since the $K\gamma$ peaks are a weak component they can be neglected. The $K\alpha$ peaks and $K\beta$ peaks are doublets owing to the difference in energies of electrons 'falling in' from different L and M subshells respectively. Electrons will not 'fall in' from the L_1 subshell, but will fall in from the L_2 and L_3 subshells. Electrons that 'fall in' from the L_2 subshell give rise to $K\alpha_2$ peaks and electrons that 'fall in' from the L_3 subshell give rise to $K\alpha_1$ peaks. Due to the small difference in energy between the $K\alpha_2$ and the $K\alpha_1$ peaks, the $K\alpha$ peak is a closely spaced doublet. A similar process occurs for electrons 'falling in' from two of the five M subshells to give a $K\beta$ doublet. For experiments where monochromatic radiation is required, $K\alpha$ radiation is of interest and a filter needs to be used to remove the $K\beta$ radiation.⁹⁰

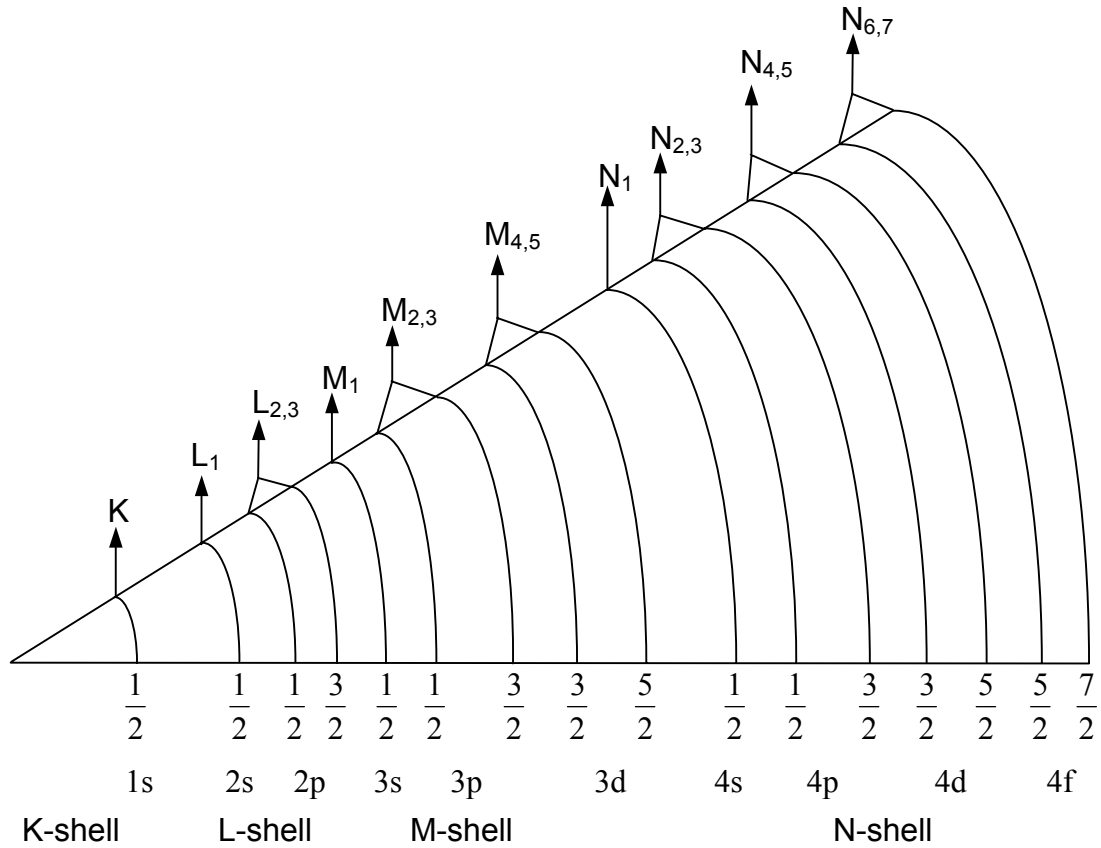


Figure 2.2.1 Schematic of electronic shells ⁸³

Diffraction of x-rays can be explained in a similar fashion to the diffraction of electrons. X-ray diffraction exploits the wave nature of electromagnetic radiation and as x-rays interact with a sample, they interfere with each other. Most of the x-rays undergo destructive interference; however, the x-rays that interact with the sample at a specific angle (θ_B) undergo constructive interference, which results in a signal for that particular angle. The angle θ_B is known as the Bragg angle and by using the formula

$$n\lambda = 2d_{hkl} \sin \theta_B \quad 2.2.1$$

the interplanar d-spacings (d_{hkl}) can be calculated using a radiation source with known wavelength (λ). The d-spacings are similar to those described in section 2.1.4.3 and are commonly defined using the Miller index hkl notation.

To acquire a diffraction pattern, a sample placed onto a sample holder made of a material that has low x-ray absorption, e.g. an amorphous polymer like poly(carbonate). The sample holder is placed on a stage and is rotated within a range of angles between 0 and 158°. ⁹¹ The x-rays diffract from the sample and are collected at the detector. The diffraction pattern is then displayed on a computer where the peaks can be matched to a database of known crystal structures compiled by the JCPDS-International Center for Diffraction Data. Each peak has a value for 2θ , which is twice the Bragg angle. A given d-spacing corresponding to a lattice plane is obtained for each 2θ value.

The size of crystallites in a system can be determined by using the Scherrer equation (equation 2.2.2):

$$t = \frac{K\lambda}{\Delta(2\theta)\cos\theta} \quad 2.2.2$$

where t is the crystallite thickness, K is a constant that depends on the shape of the crystallites and how t and $\Delta(2\theta)$ are defined, $\Delta(2\theta)$ is the full width at half maximum of a diffraction peak and λ is the wavelength of the incident x-rays. ^{90, 92} As crystallites decrease in size, their respective diffraction peaks broaden due to the increase in the number of lattice planes that diffract the incident x-rays. Crystallite size comparisons can be made by calculating the peak broadening for different samples; however, it is recommended that complementary techniques (TEM, SAXS) be used to determine the consistency of the data.

2.3 Magnetometry

Magnetometry is a general term referring to the magnetic property measurement of a particular system. Numerous techniques are available for measuring the magnetic properties of magnetic samples; however, this section will focus on a magnetometer with a Superconducting QUantum Interference Device (SQUID) based sensor. SQUID magnetometers, as they are commonly called, are known for their precision and sensitivity owing to the superconducting coils used to sense magnetic fields. This section also discusses several types of experiments used to study the magnetic properties of a sample: 1) zero field-cooled/field-cooled magnetization vs. temperature measurements, 2) room temperature hysteresis loop measurements and 3) zero field-cooled/field-cooled hysteresis loop measurements.

2.3.1 Superconducting QUantum Interference Device (SQUID) Based Magnetometer

In a superconducting quantum interference device (SQUID) based magnetometer, a magnetic sample passes through a set of sensing coils. The sensing coils are comprised of superconducting coils separated by thin insulating layers that are less than 30 Å thick. The insulating layers are called Josephson junctions after Brian Josephson who, in 1962, showed that Cooper pairs (electron pairs in superconducting materials) in superconductors can tunnel through an insulating layer or weak link between the superconductors.⁹³ A *dc*-SQUID is comprised of two Josephson junctions connected in parallel (Figure 2.3.1). A current is passed through the superconductors and when no magnetic sample is present the Cooper pairs weakly interfere as they pass through the Josephson junctions. This interference is caused by phase shifts (δ_A and δ_B) of the Cooper pairs passing through junctions A and B respectively. However, when a magnetized sample passes through the center of the SQUID device, the magnetic flux changes the interference (phase difference) of the Cooper pairs. Ultimately, the total current passing through the superconducting loops (I) changes as a result of any magnetic flux (B) through the loops by the relationship

$$I = 2I_0 \sin \delta_0 \cos\left(\frac{e}{\hbar} \int B \cdot dS\right) \quad 2.3.1$$

where I_0 is the initial current, δ_0 is a constant phase shift, e is the charge of an electron, \hbar is Planck's constant divided by 2π and S is area of the superconducting loops.⁹⁴ For a detailed mathematical derivation of equation 2.3.1, the reader is referred to Chapter 10 of⁹⁴. The current change causes a change in voltage, which is amplified by a coil coupled to the SQUID and converted into a current with equal and opposite flux.⁷³ The sensitivity of the SQUID magnetometer is directly related to its ability to measure the phase difference of Cooper pairs. This quantum level sensitivity enables SQUID magnetometers to detect and measure electrical signals in the human heart and brain.⁹⁵ SQUID magnetometers are also very precise, allowing for reproducible standard deviations on the order of 10^{-3} to 10^{-6} emu for six averaged measurements. The sensitivity of the SQUID is not necessary when measuring samples with large moments (e.g. Co, Fe, Fe₃O₄); however, the precision provides extremely reliable data for moments ranging from 10^1 to 10^2 emu.

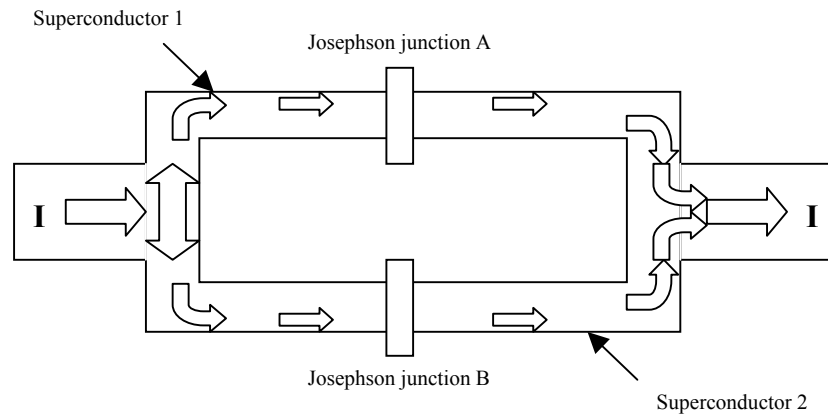


Figure 2.3.1 Diagram of SQUID sensing device

2.3.2 Types of Experiments

Numerous experiments are conducted to measure various magnetic properties of a sample. This section focuses on the four types of experiments used to characterize the nanoparticulate magnetic materials studied in this research. Some experiments are time dependent (hysteresis loop measurements), and the experimental time frames were the same for all samples analyzed. All samples in this research were prepared by weighing ~5 to 20 mg of material into an acid washed Teflon sample holder. A plug of paper was placed on the top of each sample before being capped to prevent the physical movement of the sample.

2.3.2.1 Zero Field-Cooled/Field-Cooled Magnetization vs. Temperature Measurements

The Curie temperature (T_C) of a magnetic material, if it has one, is an important value as it governs the classification of a material as ferro-, ferri- or superparamagnetic. Zero field-cooled/field-cooled magnetization versus temperature (ZFC/FC M vs. T) measurements are commonly used to determine T_C , also known as the blocking temperature, of a magnetic material. To begin, a sample is cooled from room temperature to 5 K in zero applied magnetic field. Then, a small magnetic field is applied and the temperature is ramped to 300 K in 10 K intervals (zero field-cooled measurement). When the measurement reaches 300 K, the applied field remains and the temperature is decreased to 5 K, whereupon the temperature is again increased to 300 K in 10 K intervals (field-cooled measurement). In the ZFC measurement, the

magnetic dipoles of the sample are random at room temperature and remain random upon cooling. At 5 K, the dipoles do not have enough thermal energy to rotate. As the temperature is increased, kT increases and the magnetic dipoles align in the direction of the applied magnetic field resulting in an increase in the magnetic moment. In the field-cooled measurement, the magnetic dipoles are aligned at 300 K and are cooled to 5 K in this configuration. As the temperature is increased, kT provides the energy for the magnetic dipoles to randomize resulting in a decrease in the magnetic moment. The point at which the ZFC and FC curves intersect is called the bifurcation point and the temperature at this point is called the blocking temperature. Below the blocking temperature, there is not enough thermal energy for the magnetic dipoles to randomize and a material behaves like a ferro- or ferrimagnet. Above the blocking temperature, there is sufficient thermal energy to randomize the magnetic dipoles and a material behaves like a paramagnet.

2.3.2.2 Room Temperature Magnetization vs. Applied Magnetic Field Measurements

Magnetization vs. applied magnetic field measurements (hysteresis loop measurements) are a time dependent measurement of the magnetic moment of a sample as the magnetic field is increased and decreased in a hysteretic fashion. Hysteresis loops provide information such as the saturation magnetization (M_S), remanence magnetization (M_R) and coercivity (H_C) for a given sample. These values are specific to the temperature at which the hysteresis loop experiment is performed, as the magnetic moment of a sample can depend on the temperature. Hysteresis loop experiments were performed at 300 K beginning at zero applied magnetic field. First, the magnetic field was ramped to 1000 Oe in 100 Oe increments, followed by ramping to 10,000 Oe in 1000 Oe increments and finally to 70,000 Oe in 10,000 Oe increments. Next, the magnetic field was reversed, following the same type of field spacings, to $-70,000$ Oe. Finally, the magnetic field was increased to 70,000 Oe, with the same field spacings, to complete the hysteresis loop measurement. M_S was determined by observing the magnetic moment of the material at the largest applied magnetic field. M_R was determined by locating the point on the y-axis (if there was one), where there was a magnetization in zero applied magnetic field. H_C was determined by locating the point on the x-axis (if there was one), where the magnetization was zero in an applied magnetic field (Figure 2.3.2).

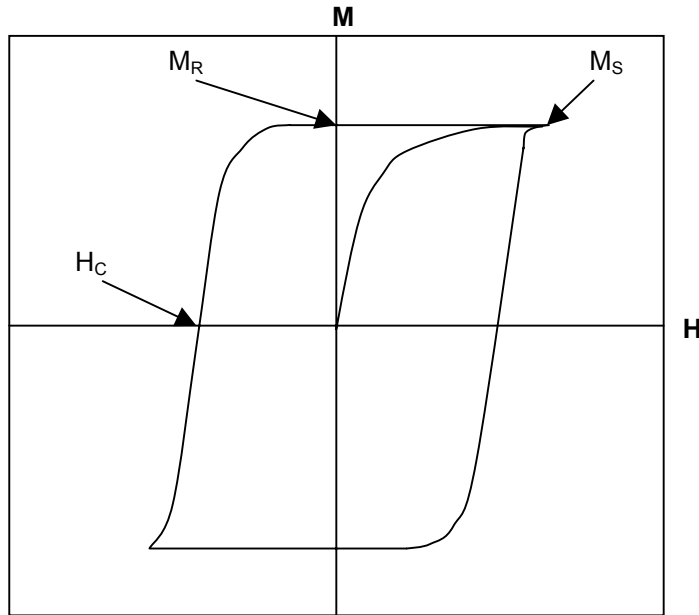


Figure 2.3.2 Hysteresis loop indicating locations of points of interest

2.3.2.3 Zero Field-Cooled/Field-Cooled Magnetization vs. Applied Magnetic Field Measurements

Interactions or impurities can be present in a sample that the previous two measurements would not detect. It is necessary, therefore, to conduct a third set of experiments that allow for the detection of these interactions and impurities. Specifically, transition metal ions not incorporated into a crystal lattice are paramagnetic. The paramagnetic susceptibility (χ) of a material can be detected at low temperatures (5 K), due to the relationship of χ with temperature. Paramagnetic materials obey the Curie law ($\chi=C/T$), so the lower the temperature the higher the magnetic susceptibility (χ). Thus, a positive slope of the magnetization curves at 5 K can be indicative of paramagnetic species in the sample. Furthermore, transition metals readily oxidize upon exposure to air. The oxidation process of transition metal (Co, Ni) particles typically leads to the formation of an antiferromagnetic oxide shell around a ferromagnetic core. The Néel temperature of an antiferromagnet is usually lower than 300 K; hence, at 300 K the antiferromagnet is behaving like a paramagnet and there is no observable coupling between the antiferromagnet and the ferromagnet. However, if the sample is cooled to a temperature below the Néel temperature of the antiferromagnet, an exchange interaction is observed. In a zero field-cooled (ZFC) hysteresis loop measurement, the sample is cooled from 300 K to 5 K without

an externally applied. Once at 5 K, the sample undergoes a hysteresis loop measurement similar to that described in section 2.3.2.2. Next, the sample is warmed to 300 K, where a 70,000 Oe magnetic field is applied. The sample is then cooled to 5 K (field-cooled (FC)), where it undergoes a hysteresis loop measurement similar to that described in section 2.3.2.2., without the initial ramping from 0 to 70,000 Oe. In the ZFC part of the measurement, both the ferromagnetic and antiferromagnetic components of the sample are cooled without any alignment of the magnetic dipole moments. Hence, the ZFC measurement resembles a 300 K hysteresis loop in shape and symmetry. However, in the FC part of the measurement, the ferromagnetic and antiferromagnetic components of the sample are in an applied field when cooled. This means that the ferromagnetic part will align in the direction of the applied magnetic field, and since the antiferromagnetic part is in contact with the ferromagnetic part it will align in the lowest energy configuration. This coupling of the antiferromagnet with the ferromagnet results in the FC loop undergoing an asymmetric shift. Figure 2.3.3 shows a schematic of an antiferromagnetic/ferromagnetic coupled sample as it is taken through the field-cooled part of the ZFC/FC hysteresis loop cycle. First the sample is cooled from 300 K to 5 K in an applied magnetic field of 70,000 Oe. This takes the antiferromagnet (AFM) below its temperature and the magnetic dipoles align with the ferromagnet (FM) to achieve the lowest energy state (Figure 2.3.3, arrow A). Next, the applied magnetic field is decreased from 70,000 Oe to $-70,000$ Oe and during this process the magnetic dipoles of the FM begin to rotate towards the direction of the negative applied field (Figure 2.3.3, arrow B). However, the AFM is coupled to the FM and imparts a microscopic torque on the FM. Thus, it takes a larger applied field for the FM magnetic dipoles to rotate 180° than it would without any exchange interaction. At $-70,000$ Oe the FM magnetic dipoles have completely rotated towards the applied field direction (Figure 2.3.3, arrow C). Upon increasing the field from $-70,000$ Oe to 70,000 Oe, the magnetic dipoles of the FM will rotate back to their initial state (Figure 2.3.3, arrow A), but this rotation requires less of an applied field due to the torque exerted by the AFM (Figure 2.3.3, arrow D). The exchange interaction (exchange bias) between the AFM and FM leads to an asymmetric field-cooled hysteresis loop shift. The magnitude of the shift (exchange field (H_E)) is measured by taking the average of the sum of the absolute values of the positive and negative coercive fields. In the example shown ($+H_C \sim -50$ Oe and $-H_C \sim -6400$ Oe) the value of H_E is approximately -3200 Oe.

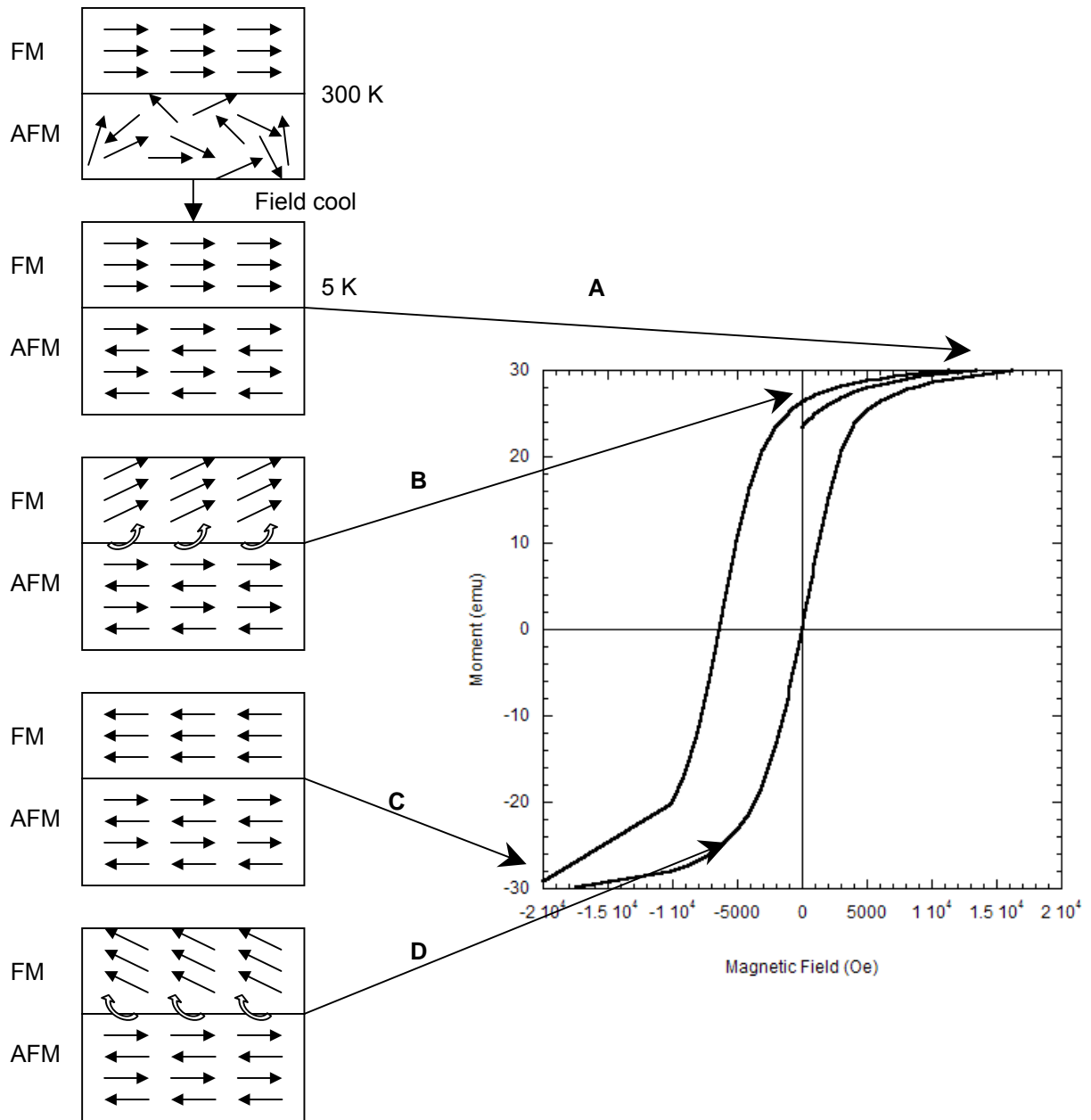


Figure 2.3.3 Schematic showing the behavior of magnetic dipoles of ferromagnetic (FM) and antiferromagnetic (AFM) components of a material undergoing a field-cooled hysteresis loop measurement

2.3.2.4 Henkel plot experiments

Henkel plot experiments can be used to determine the presence of interparticle interactions within magnetic nanoparticle systems. Allen *et al.* have used Henkel plots to study ferritin nanoparticles and determined that weak interparticle interactions were present.⁹⁶ To construct a Henkel plot, isothermal remanence magnetization (IRM) curves are generated for a virgin sample by applying a magnetic field for 700 seconds and measuring the total magnetic moment. The field is then removed and the remanent moment is measured after waiting 700 seconds. This procedure is done in 500 Oe intervals up to 20,000 Oe, whereupon the procedure is reversed beginning at -500 Oe and increasing the negative field to -20,000 Oe. The reversal procedure generates *dc*-demagnetization curves (DCD). A plot of IRM versus DCD indicate how well particles obey the Wohlfarth relation:

$$M_{DCD} = M_{\infty} - 2M_{IRM} \quad 2.3.2$$

where M_{DCD} is the *dc*-demagnetization remanence, M_{∞} is the saturation remanence and M_{IRM} is the isothermal remanence magnetization remanence.^{97, 98} The Wohlfarth relation is linear and any deviation from linearity is interpreted as being due to interparticle interactions.

2.4 Small Angle X-ray Scattering

Since x-rays interact almost entirely with the electrons of atoms, small angle x-ray scattering (SAXS) can be used to study variations in electron density within a sample. When using SAXS to study nanoscale metallic particles, the variations in electron density are related to the particle size, particle shape and particle size distribution. SAXS operates on the same basic principles as XRD; however, the information about the sample is different. While XRD typically operates at values of 2θ greater than 10° (Bragg region), SAXS operates between 2θ values of $0-6^\circ$ (Guinier and Porod regions). Crystallographic data about a sample cannot be obtained at such small values of 2θ , because d_{hkl} is inversely related to θ from Bragg's law (equation 2.2.1). By decreasing θ , larger structures can be probed providing useful information on average particle size and shape within a sample. A SAXS pattern is similar to an electron or x-ray diffraction pattern, in that the information obtained pertains to the periodicity with which certain objects are arranged. In electron and x-ray diffraction, the resulting patterns depend on the periodic spacing of lattice planes that are oriented with respect to the incident electron or x-ray beam. SAXS patterns provide information on the periodicity of electron density, which can be related to the

size of objects within a sample. SAXS results are discussed in terms of q and intensity (I), where q is defined by the relationship:

$$q = \frac{2 \sin \theta}{\lambda} = r_{hkl} = \frac{1}{d_{hkl}} \quad 2.4.1$$

where r_{hkl} is the reciprocal space lattice and d_{hkl} is the real space lattice. Thus, the units used for q are \AA^{-1} . As shown in Figure 2.4.1, q is the vector difference between the incident radiation vector (S_0) and the scattered radiation vector (S).⁹²

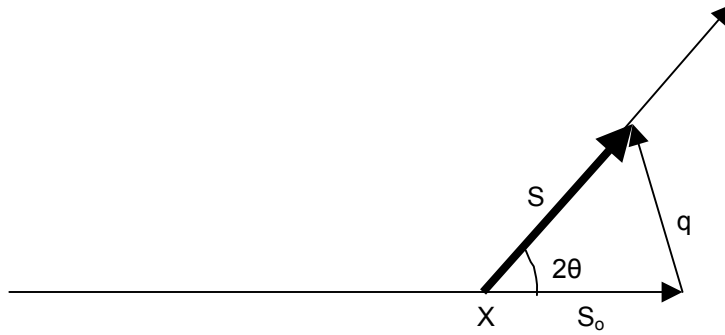


Figure 2.4.1 Vector diagram of incident radiation (S_0) and radiation scattered from X (S).

The intensity is expressed as:

$$\frac{dW}{d\Omega} = P_0 \Delta\Omega_1 \frac{\Delta\lambda}{\lambda} \Delta\Omega_2 S d \exp(-\mu d) \frac{d\sigma}{d\Omega} \quad 2.4.2$$

where P_0 is the intensity of the incident radiation, S is the sample cross-section, d is the sample thickness, μ is the attenuation coefficient, $\Delta\Omega_1$ and $\Delta\Omega_2$ relate to the uncertainty of the scattering angle, $\frac{\Delta\lambda}{\lambda}$ is the monochromator wavelength bandwidth and $\frac{d\sigma}{d\Omega}$ is the differential cross-section of the material per unit volume.⁹⁹

A schematic of a SAXS apparatus is shown in Figure 2.4.2. Powder samples are mounted in the center hole of brass sample holder and held in place with adhesive tape. If the sample is a liquid, it is sealed in an evacuated capillary tube. The specimen is placed inside a chamber that is subsequently evacuated. The incident beam passes through a monochromator prior to interacting with the sample. After interaction with the sample, scattered x-rays are detected by a position sensitive detector (PSD). A beam stop is placed at $\theta = 0$ (transmitted radiation) to prevent damage to the detector.

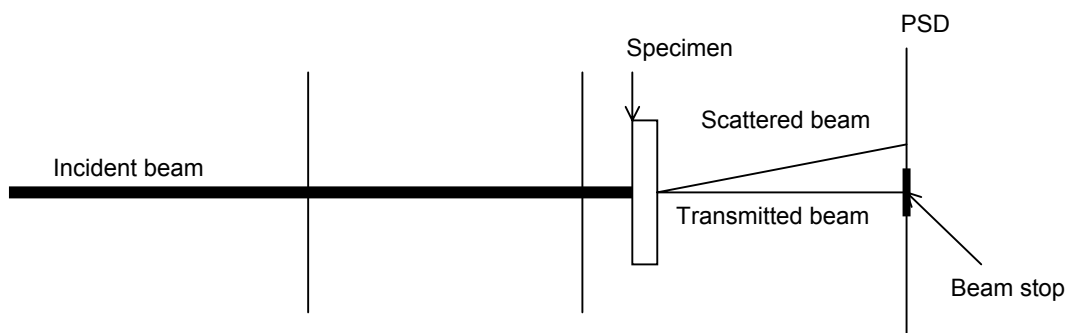


Figure 2.4.2 Diagram of small angle x-ray scattering instrument

SAXS data analysis is performed using Igor Pro software (Wavemetrics) and a subroutine from NIST modeling x-ray scattering from polydisperse spheres.¹⁰⁰ Mean particle size values and standard deviations determined from TEM are entered as starting values for the fitting. Three additional fits of models to the data are evaluated, where the particle size, polydispersity and particle size/polydispersity values are permitted to vary to optimize the curve fitting.

CHAPTER 3. Structural and Magnetic Properties of Oxidatively Stable Cobalt Nanoparticles Encapsulated in Graphite Shells

Michael A. Zalich,^{1,3} Vincent V. Baranauskas,³ Judy S. Riffle,³ Martin Saunders,² Timothy G. St. Pierre^{1*}

¹School of Physics and ²Center for Microscopy and Microanalysis, The University of Western Australia, 35 Stirling Highway, Crawley, WA 6009, Australia; ³Department of Chemistry and Macromolecules and Interfaces Institute, Virginia Polytechnic Institute and State University, Blacksburg, VA 24060, USA

3.1 Abstract

Oxidatively stable magnetic cobalt nanoparticles were prepared by annealing cobalt nanoparticles coated with poly(styrene-*b*-4-vinylphenoxyphthalonitrile) block copolymers. An oxygen impermeable graphitic coating around the cobalt nanoparticles was created during thermal treatment at 700°C owing to the thermal decomposition/crosslinking of a polymer with a highly aromatic character. A variety of analytical techniques was used to elucidate the physical properties of the pre-heat-treated and heat-treated samples. The cobalt specific saturation magnetization (σ_s) increased from 81 to 173 emu g⁻¹ Co upon heating of the polymer coated cobalt nanoparticles. The pre-heat-treated sample readily oxidized, as revealed by low-temperature magnetic susceptibility studies, whereas the heat-treated sample showed oxidative stability for over one year. The mean cobalt particle size increased from 18.5 to 36.1 nm during thermal treatment. Electron diffraction and x-ray diffraction revealed that the pre-heat-treated particles were weakly crystalline, while the heat-treated particles were strongly crystalline. The dominant phase of the heat-treated sample was determined to be face-centered cubic with other minor phases present (hexagonal close packed, epsilon).

Keywords: cobalt, nanoparticles, magnetic, microscopy, diffraction

3.2 Introduction

Magnetic nanoparticles are of considerable interest owing to their potential applications in biomedicine and the magnetic recording industry. There are several current and potential applications for magnetic nanomaterials in medicine including magnetic resonance imaging (MRI) contrast agents,¹⁰¹ magnetic field directed drug delivery systems,^{102, 103} biotoxin removal,^{104, 105} gene therapy,^{106, 107} and magnetic fluid hyperthermia.¹⁰⁸ Iron oxides (magnetite and maghemite) have received much attention owing to their oxidative stability and biocompatibility; however, other transition metals and their alloys are also under investigation (Ni, Co, Fe). Cobalt has one of the largest magnetic susceptibilities of these materials but it readily oxidizes upon exposure to air resulting in the antiferromagnetic cobalt oxide. Hence, coating of cobalt nanoparticles with an oxygen impermeable sheath is a desirable prerequisite for their potential use in biomedical applications.

Several research groups have prepared graphite coated cobalt nanoparticles, nanorods and nanocapsules utilizing the Krätschmer-Huffman carbon arc process designed for the synthesis of fullerene materials.¹⁰⁹⁻¹¹⁵ The resulting materials are reported to be oxidatively stable and chemically resistant, which are desirable qualities if such materials were to be used for biomedical applications. Harris *et al.* reported on the impregnation of a pyrolyzed block copolymer comprised of poly(vinylidene chloride) and poly(vinyl chloride) with a cobalt nitrate solution heated at 1800°C for two hours. Their findings indicated that a small percentage (5%) of metallic cobalt particles were encapsulated in graphite shells.¹¹⁶ Tomita *et al.* reported that the transition metals (Co, Ni, Fe) act as catalysts in graphitization and their studies revealed the onset of a graphitic coating at 600°C upon the annealing of cobalt and diamond particles with electron beam radiation.¹¹⁷ Finally, Yudasaka *et al.* studied the properties of nickel films deposited on various allotropic carbon films. They concluded that nickel can catalyze the formation of graphite from any organic precursor; however, the organic precursor governs the temperature at which graphitization occurs.¹¹⁸

Herein, we report the physical properties of cobalt nanoparticles prepared by the thermolysis of dicobalt octacarbonyl in poly(styrene-*b*-4-vinylphenoxyphthalonitrile) copolymer micelles and subsequently heated at 700°C to create graphite-coated, oxidatively-stable cobalt nanoparticles. Magnetic susceptometry, transmission electron microscopy, electron diffraction,

x-ray diffraction and small-angle x-ray scattering were utilized to assess the properties of these materials.

3.3 Experimental Section

3.3.1 Synthesis of poly(styrene-*b*-4-vinylphenoxyphthalonitrile).

A detailed synthetic procedure for poly(styrene-*b*-4-vinylphenoxyphthalonitrile) and the characterization thereof has been previously reported.¹¹⁹ Briefly, the block copolymer was synthesized by a living anionic polymerization. First, poly(styrene-*b*-*tert*-butyldimethylsilyloxystyrene) was prepared by the sequential addition of styrene and *tert*-butyldimethylsilyloxystyrene monomers using *n*-butyllithium as the initiator. Next, the *tert*-butyldimethylsilyl ether group of poly(styrene-*b*-*tert*-butyldimethylsilyloxystyrene) was hydrolyzed under acidic conditions to generate poly(styrene-*b*-4-vinylphenol). Poly(styrene-*b*-4-vinylphenoxyphthalonitrile) was synthesized by reacting 4-nitrophthalonitrile with poly(styrene-*b*-4-vinylphenol) in the presence of potassium carbonate. The poly(styrene-*b*-4-vinylphenoxyphthalonitrile) polymer synthesized for this study had well controlled block lengths of 50,000 and 10,000 g mol⁻¹ respectively (Figure 3.1). The composition and molecular weight of the polymer were characterized with ¹H-NMR, gel permeation chromatography and infrared spectroscopy.

3.3.2 Cobalt nanoparticle synthesis.

Cobalt nanoparticles were synthesized by the addition of 1 g of dicobalt octacarbonyl into a reaction vessel containing 0.5 g of poly(styrene-*b*-4-vinylphenoxyphthalonitrile) dissolved in 50 mL of deoxygenated toluene. The reaction was refluxed at 110°C for 5 hours and the subsequent reaction product was placed into a capped vial and purged with dry nitrogen. Toluene was removed from the sample under vacuum at 100°C for ~ 24 hours (pre-heat-treated sample).

3.3.3 Elevated heat treatment of polymer coated cobalt nanoparticles.

Approximately 1 g of the dried cobalt-polymer complex was placed into a ceramic boat and positioned in the center of a quartz tube furnace under a constant argon flow. The tube

furnace was then heated at 700°C for 4 hours, after which the sample was removed and stored under atmospheric conditions for analysis (heat-treated sample).

3.3.4 Transmission electron microscopy.

Transmission electron microscopy (TEM), high-resolution TEM (HRTEM), energy-filtered TEM (EFTEM), selected area electron diffraction (SAD) and nano-beam electron diffraction (NBD) were conducted with a JEOL 3000F field-emission transmission electron microscope (operated at 300 kV) equipped with a Gatan image filter (GIF) and digital imaging system. The pre-heat-treated sample was re-dispersed in toluene and cast onto an amorphous carbon-coated copper grid for analysis. The heat-treated sample was embedded in resin and microtomed to a thickness of ~ 100 nm. Microtomed slices were then placed onto an amorphous carbon coated copper grid for analysis. NBD was conducted on single crystals of the heat-treated sample using an ~2 nm focused electron beam. Particle size analysis was performed on two fields of view for each sample. Each field of view was divided into sections and all of the particles of a particular section were measured in two directions: 1) in any obvious long direction and 2) perpendicular to the first measurement. The two measurements for each particle were then averaged and the aspect ratio for each particle (longer measurement/shorter measurement) was calculated. The mean and standard deviation were calculated for the particle size and aspect ratio for both fields of view of each sample. Energy-filtered TEM was conducted using the GIF with a spectrometer slit width of 40 eV at the cobalt $L_{3,2}$ edge (778-793 eV). Pre-edge background images were acquired at 714 and 753 eV and the post-edge image at 799 eV.

3.3.5 Small angle x-ray scattering.

Small angle x-ray scattering (SAXS) measurements were conducted on a Bruker Nanostar SAXS instrument. Samples were prepared by placing a powdered fraction of each sample in the center of a sample holder where it was held in place with adhesive tape. The samples were measured for 12 hours over a 2θ range of 0-4.4° with a Cu $K\alpha$ source.

3.3.6 X-ray Diffraction.

Siemens x-ray diffractometers (model D-500 for pre-heat-treated sample and D-5000 for heat-treated sample, both using Cu- $K\alpha$ radiation) were used to acquire x-ray diffraction patterns

of the pre-heat-treated and heat-treated samples. Powdered samples were placed onto poly(carbonate) sample holders and scanned at: 1) a rate of 0.2°/min with a step size of 0.03° from 10-110° for the pre-heat-treated sample and 2) a rate of 0.13 °/min with a step size of 0.04° from 10-110° for the heat-treated sample.

3.3.7 Magnetic Susceptometry.

A Quantum Design magnetic properties measurement system (MPMS-7) equipped with a superconducting quantum interference device (SQUID)-based sensor was used to make cobalt specific magnetization measurements (σ) at varying applied fields (H) from -70,000 to +70,000 Oe at 300 K and 5 K, with 100 Oe spacings between -1000 Oe and 1000 Oe. Low-temperature measurements were conducted both after cooling the sample in zero applied field and in an applied field of 70,000 Oe. The purpose of the different measurements was to study: 1) the saturation magnetization at 300 K, 2) the hysteretic behavior of the sample at 300 K, 3) the presence of an exchange bias, owing to a cobalt oxide layer on the surface of the cobalt nanoparticles and 4) the presence of paramagnetic species, owing to any residual cobalt carbonyl species in the sample. In addition, isothermal remanent magnetization (IRM) and DC-demagnetization (DCD) curves were generated at 300 K in order to qualitatively understand the interparticle interactions of the magnetic cobalt nanoparticles in both systems. The IRM curve was measured by applying a constant magnetic field for 700 s, removing the field and measuring the remanent moment 700 s after field removal. This process was conducted up to 20 kOe (in 500 Oe steps), whereupon the procedure was reversed (beginning at -500 Oe) and followed by applying negative fields to -20 kOe to provide the DCD curve. Henkel plots generated from these data were constructed by plotting the normalized IRM remanence vs. DCD remanence magnetizations.

3.3.8 Elemental analysis.

Elemental analyses were performed on the pre-heat-treated and heat-treated samples using inductively coupled plasma atomic emission spectroscopy (ICP-AES) at the Marine and Freshwater Research Laboratory at Murdoch University, Perth, Western Australia. The samples were prepared by digestion in a 1:1 mixture of HNO₃:H₂SO₄ for 13 days at 70-100°C. The samples and a blank were diluted and analyzed for cobalt concentrations.

3.4 Results and Discussion

3.4.1 Particle size analysis.

Transmission electron microscopy (TEM) was used to study the particle size, size distribution, morphology, chemical composition and crystallinity of the pre-heat-treated and heat-treated cobalt complexes. A ‘particle’ was deemed to be a region with contrast obviously different from the background. Diffraction contrast causes individual particles to have different intensities. Particles were easy to define in the heat-treated sample owing to the strong crystallinity and contrast relative to the background and the relatively large particle size. The decreased crystallinity and smaller particle size of the pre-heat-treated sample made it more difficult to accurately identify the edges of the particles and more care was needed to ensure that accurate particle size data were obtained in this case. The particle size distribution for the pre-heat-treated sample ranged from 9 to 45 nm with a mean of 18.5 nm (sample population = 346 particles) (Figure 3.2). The average aspect ratio for particles of the pre-heat-treated sample was 1.43 with a standard deviation of 0.39. A dramatic increase in particle size and size distribution after heat treatment at 700°C was apparent from the images taken during analysis. The particle size distribution for the heat-treated sample increased to 7 to 147 nm with a mean of 36.1 nm (sample population = 369 particles) (Figure 2). The average aspect ratio was 1.48 with a standard deviation of 0.51. These increases in mean particle size and size distribution are likely to result from particle sintering at 700°C, which may be explained by an Ostwald ripening mechanism similar to that reported by Host *et al.*¹⁰⁹

3.4.2 Small angle x-ray scattering.

Small angle x-ray scattering data were analyzed using Igor Pro (Wavemetrics) software and a NIST subroutine (PolyCoreForm)¹⁰⁰ modeling x-ray scattering from polydisperse spheres. Mean particle size values and standard deviations determined from TEM were entered as starting values for the fitting. Three additional fits of models to the data were evaluated, where the particle size, polydispersity and particle size/polydispersity values were permitted to vary to optimize the curve fitting (curves not shown). The measured SAXS data were consistent with the particle size and size distribution data obtained from TEM particle size analysis. The SAXS data indicated that the pre-heat-treated sample comprised smaller particles with a narrower size distribution than the heat-treated sample.

3.4.3 Transmission Electron Microscopy.

Energy filtered TEM (EFTEM) was conducted on the pre-heat-treated and heat-treated samples to confirm the elemental identity of the electron dense nanoparticles. The resulting cobalt distribution maps correlated well with the electron dense regions of the bright field images, confirming the chemical identity of the particles in both samples (Figure 3.3).

There are two reported phases of cobalt for nanomaterials: 1) face-centered cubic (fcc)^{56, 120} and 2) epsilon (ϵ).^{47, 50, 121} Moreover, the three reported phases of cobalt (hexagonal close packed (hcp), fcc and ϵ) are very close in energy and low activation energies are sufficient to cause stacking faults and possibly complete phase transitions.^{47, 121}

High-resolution TEM (HRTEM) was used to observe the presence of any crystallinity in the cobalt nanoparticles. HRTEM analysis of the pre-heat-treated sample indicated weak particle crystallinity; however, there were some well-crystallized particles (Figure 3.4 A). Measurements of planar spacings (1.97 Å) from an exemplary highly crystalline particle are consistent with the {111} crystal plane (2.05 Å) of fcc cobalt, but could also correspond to the {002} or {101} crystal plane of hcp cobalt or the {310} crystal plane of ϵ -cobalt (2.04 Å).^{1, 47, 122}

HRTEM of the heat-treated sample revealed highly crystalline particles with defects, such as twin planes. Twinning is commonly observed in nanocrystals, often among fcc materials.¹²³ Measurements of lattice spacings (2.04 Å) of a multi-twinned crystalline particle again matched the {111} plane of fcc cobalt (2.05 Å) (Figure 3.4 B). The presence of fcc cobalt was confirmed through nano-beam electron diffraction of individual particles (Figure 3.4 C). A small number of particles demonstrating hcp structure were also found (Figure 3.5 A). A Fourier transform of Figure 3.5A gives a hexagonal arrangement of spots at a 2.2 Å spacing, consistent with the {10 $\bar{1}$ 0} plane in hcp-Co (Figure 3.5 B). In addition, the high-resolution image revealed the presence of a graphitic coating around the cobalt particle (Figure 3.5 A inset). Measurements of the Fourier transform of Figure 3.5A indicated that the spacing between the layers surrounding the particle is consistent with the interlayer spacing of graphite (3.4 Å).¹²⁴ This graphitic coating may be the barrier that afforded observed oxidation protection for over one year.¹¹⁹ McHenry *et al.* also reported the presence of faulted graphite coated cobalt particles prepared by a process based on the Krätschmer-Huffman carbon arc process.¹¹¹

3.4.4 X-ray Diffraction.

X-ray diffraction (XRD) was used to complement electron diffraction data as it provides crystallographic information on the bulk of the sample in an effort to determine the presence of a dominant phase of cobalt in these systems. Broad peaks at $2\theta = 17^\circ$ were found in both diffraction patterns and are due to an adhesive used to hold the samples on the holder. XRD yielded information about the crystal phase of cobalt in the pre-heat-treated sample, despite its weakly crystalline nature. By using the JCPDS database, the structure was determined to be fcc cobalt (Figure 3.6, Table 3.1), although there were other peaks (a and b) that appeared in the diffraction pattern. These peaks seemed to match well with cobalt oxide, which is likely since the magnetic susceptibility measurements indicated a cobalt oxide component in the pre-heat-treated sample (see section 3.4.5). XRD also clarified the crystal phase of cobalt in the heat-treated sample. The peaks in the heat-treated sample diffraction pattern were more well-defined than the pre-heat-treated sample indicating that an improvement in crystallinity had taken place during the heating procedure (Figure 3.7). Furthermore, the peaks were matched to the fcc phase of cobalt using the JCPDS software database (Table 3.2). Thus, it appears that the dominant phase of cobalt in the heat-treated cobalt nanoparticle system is fcc; however, there may be a small percentage of hcp and ϵ -cobalt present. Saito and Saito *et al.* reported that small amounts of the hcp phase of cobalt were formed by a method based on the carbon arc method for fullerene production; however, the dominant phase was fcc cobalt.^{114, 115} Additionally, the broad peak at $2\theta \approx 24^\circ$ corresponds to an experimental d-spacing of 3.7 Å. This value falls within the range reported for the interplanar spacings of graphite ($d_{002} = 3.4\text{-}3.9$ Å) in carbon nanotubes of varying diameter.¹²⁴ Since the peak is broad, it is thought to encompass graphitic spacings of coatings on particles of varying dimensions. Finally, the Scherrer equation was used to qualitatively examine peak broadening caused by differences in particle size. The x-ray diffraction peaks were narrower for the heat-treated sample indicating that the relative particle size for the heat-treated sample is larger than the relative particle size for the pre-heat-treated sample, which suggests an increase in particle size with heat treatment. This conclusion is consistent with both TEM and SAXS data on the particle sizes of these systems.

3.4.5 Magnetic Susceptometry.

Magnetic susceptometry measurements were conducted on the pre-heat-treated and heat-treated samples at 300 K and 5 K to elucidate their magnetic properties. Room temperature σ vs. H measurements of the pre-heat-treated sample revealed a cobalt specific saturation magnetization (σ_s) of $81 \text{ emu g}^{-1} \text{ Co}$, a cobalt specific remanent magnetization (σ_r) of $19 \text{ emu g}^{-1} \text{ Co}$ and a coercivity (H_c) of $\sim 410 \text{ Oe}$ (Figure 8A). The magnetic remanence and coercivity values along with zero-field cooled/field cooled σ vs. T measurements indicated that the sample is comprised of a combination of superparamagnetic and magnetically blocked particles at room temperature.

The slope of the magnetization curve is positive in high fields at low temperature, while at 300 K this slope is reduced and the magnetization curve almost saturates at high fields (Figure 3.8). This positive slope at 5 K is indicative the presence of paramagnetic material with a possible contribution from an antiferromagnetic component in the sample. It is difficult to separate the paramagnetic component from the antiferromagnetic component, as the magnitude of their effects is similar, but much lower than that of a ferromagnetic material. The paramagnetic component may be due to unreacted cobalt carbonyl species that have not been incorporated into cobalt nanoparticles. Low temperature zero field-cooled/field-cooled hysteresis loop experiments exhibit an asymmetric field-cooled hysteresis loop shift. This field-cooled hysteresis loop shift is indicative of an exchange bias ($H_e \approx 3200 \text{ Oe}$) created by the coupling of an antiferromagnetic cobalt oxide surface layer with the ferromagnetic cobalt metal core.¹²⁵⁻¹²⁷ Thus, the departure of σ_s for the pre-heat-treated sample from the value for bulk cobalt is most likely due to residual cobalt carbonyl species and the partial oxidation of the sample.

Two different sample digestion procedures led to two different cobalt concentration measurement results for the heat-treated sample as reported by Baranauskas *et al.*¹¹⁹ Briefly, the first digestion procedure involved dissolving the sample in a 1:1 mixture of concentrated HNO_3 : H_2SO_4 for 4 days between 70-100°C. The second procedure involved dissolving the sample in a 1:1 mixture of concentrated HNO_3 : H_2SO_4 for 13 days between 70-100°C with an addition of 5 mL of concentrated H_2SO_4 on the ninth day. The relatively robust nature of a protective graphitic coating will hamper acid digestion of the metallic cobalt and hence is likely the cause for disagreement between the elemental analysis data. The first digestion procedure

(D1) gave a [Co] = 31% by mass while the more rigorous second digestion procedure (D2) gave [Co] of 41% by mass. The difference in these cobalt concentrations suggests that: 1) the protective coating can be digested over time under extreme conditions or 2) it takes a significant amount of time for the acid to penetrate defects in the graphitic coatings and dissolve the cobalt particles. Room temperature magnetic susceptometry measurements showed apparent saturation magnetizations of 230 emu g^{-1} of calculated Co for D1 and 172 emu g^{-1} of calculated cobalt for D2 (Figure 3.9A). Both the magnitude of these values and their differences indicate that the sample digestion procedure for this material is critical to the values of cobalt concentration obtained from the ICP-AES measurements. The value of 230 emu g^{-1} Co for D1 is significantly higher than the maximum cobalt specific magnetization expected based on the value for bulk cobalt, and hence implies that the sample digestion was incomplete. The reduction in the apparent cobalt specific magnetization with increased digestion time suggests that the digestion process is very slow for this material. Several research groups have investigated the use of acid digestion techniques to dissolve unencapsulated cobalt formed when preparing graphite coated cobalt nanoparticles using a modified arc-discharge procedure. Their findings indicated that cobalt particles completely encapsulated by graphite were not dissolved; however, the acid treatments used were not as rigorous as reported above.^{110, 113, 128} It is reasonable that strong mineral acids will eventually penetrate minor defects in the graphite coatings leading to cobalt dissolution. Moreover, the difference of σ_s for D2 (172 emu g^{-1} Co) is only 7.5% larger than the literature value of $\sim 160 \text{ emu g}^{-1}$ Co.¹²⁹ This error may be within the limits of reproducibility for the elemental analysis measurements. Room temperature magnetic hysteresis loop measurements showed that the sample exhibits magnetic remanence and coercivity ($\sigma_r = 34 \text{ emu g}^{-1}$ Co; $H_c = 416 \text{ Oe}$). Field cooled and zero field cooled σ vs. T measurements in conjunction with σ vs. H measurements at room temperature (Figure 9A) suggest that the heat-treated sample consists of a combination of particles that are superparamagnetic and magnetically blocked at room temperature.

Low temperature magnetization measurements on these heat-treated cobalt-graphitic complexes indicate similar saturation magnetizations to those measured at room temperature. Field-cooled σ vs. H measurements show magnetic hysteresis with negligible field bias ($H_e = 144 \text{ Oe}$) relative to zero-field-cooled σ vs. H measurements (Figure 3.9B and 3.9C), suggesting the absence of cobalt oxide layers around the metallic cobalt nanoparticles. The long-term

saturation magnetization stability confirms that the annealed carbonaceous cobalt complexes are oxidatively stable.¹¹⁹ Compared with the pre-heat-treated sample, the cobalt specific magnetization for the heat-treated sample saturates at high fields in both room temperature and low temperature studies indicating an absence of the paramagnetic component that was observed for the pre-heat-treated sample. It is possible that residual carbonyl species evolve during thermal treatment with the concomitant incorporation of residual cobalt atoms into the cobalt nanoparticles, and that this largely decreases or eliminates any paramagnetic species in the sample.

Henkel plots (not shown) for the pre-heat-treated and heat-treated systems indicated weak interparticle demagnetizing magnetic interactions as would be expected for magnetic cobalt nanoparticles in close proximity with each other (but not in direct contact.)

3.5 Conclusions

Cobalt nanoparticles were prepared by the thermolysis of dicobalt octacarbonyl in poly(styrene-*b*-4-vinylphenoxyphthalonitrile) block copolymer micelles. The particles were subsequently heat-treated at 700°C to afford oxidatively stable cobalt nanoparticles with a “graphitic” coating. The cobalt specific saturation magnetization value increased upon heating due to one or both of the following reasons: 1) sintering of cobalt nanoparticles leading to an increase in particle size and 2) annealing of cobalt nanoparticles leading to an increase in particle crystallinity. A graphitic coating appears to be the protective barrier against oxidation for the heat-treated cobalt nanoparticles. Transmission electron microscopy, electron diffraction and x-ray diffraction were used to identify the dominant crystal phase of the pre-heated and heat-treated samples as being face-centered cubic, although there may be oxide present in the pre-heated sample and other phases of cobalt (hcp, ϵ) present.

Future work will involve studying the heat treatment process in more detail to create an oxygen impermeable coating around the cobalt nanoparticles and improving the particle crystallinity without any particle sintering.

3.6 Acknowledgements

The authors of this paper acknowledge the support of NSF under contract DMR-0312046, DARPA-AFOSR (contracts #F49620-02-1-0408 and F49620-03-1-0332), OMNOVA

Solutions and the Australian Research Council (grant # DP0559333) for funding. M. A. Zalich thanks the Australian-American Fulbright Commission for a Fulbright Postgraduate Fellowship to conduct research in Australia. The authors would also like to thank Dr. J. Connolly from Curtin University of Technology, Perth, Australia for help with SAXS data acquisition and E. Bovell from The University of Western Australia for help with SAXS curve fitting.

*Corresponding author: A/Prof Timothy G. St. Pierre, School of Physics, The University of Western Australia, Crawley, WA, 6009, Australia. Ph: +61 8 6488 2747; Fax: +61 8 6488 1879; e-mail: stpierre@physics.uwa.edu.au

Table 3.1 Experimental and literature d-spacings for fcc cobalt for the pre-heat-treated sample.

Peak number	2 θ	d-spacing in Å (experimental)	d-spacing in Å (literature)
1	44.24	2.05	2.05
2	51.49	1.78	1.77
3	75.88	1.25	1.25
4	92.38	1.07	1.07
5	97.84	1.02	1.02
a (Co ₃ O ₄)	36.16	2.48	2.44
b (CoO)	61.69	1.50	1.51

Table 3.2 Experimental and literature d-spacings for fcc cobalt for the heat-treated sample.

Peak number	2 θ	d-spacing in Å (experimental)	d-spacing in Å (literature)
1	44.24	2.05	2.05
2	51.52	1.77	1.77
3	75.84	1.25	1.25
4	92.28	1.07	1.07
5	98.12	1.02	1.02
a	24.08	3.70	3.4-3.9 ¹²⁴

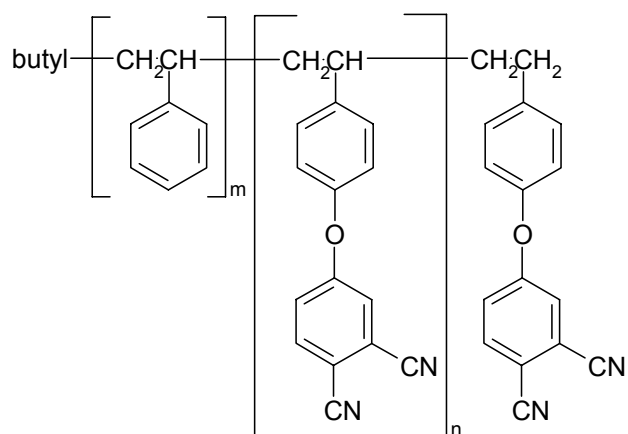


Figure 3.1 Poly(styrene-*b*-4-vinylphenoxyphthalonitrile)

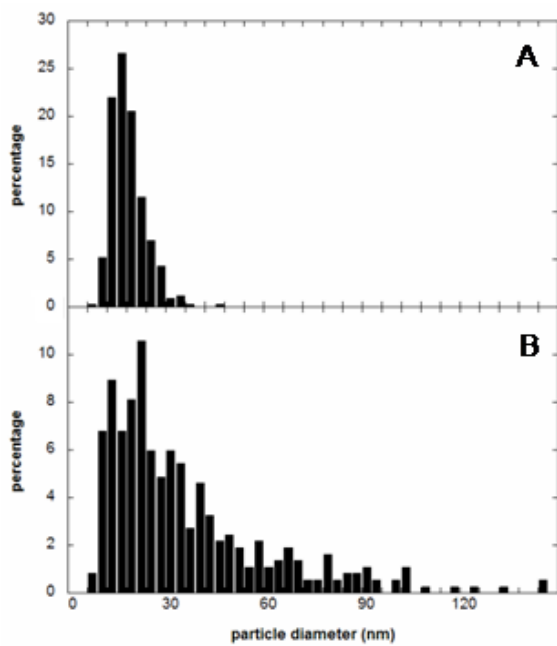


Figure 3.2 Particle size histograms for: A) pre-heat-treated and B) heat-treated samples

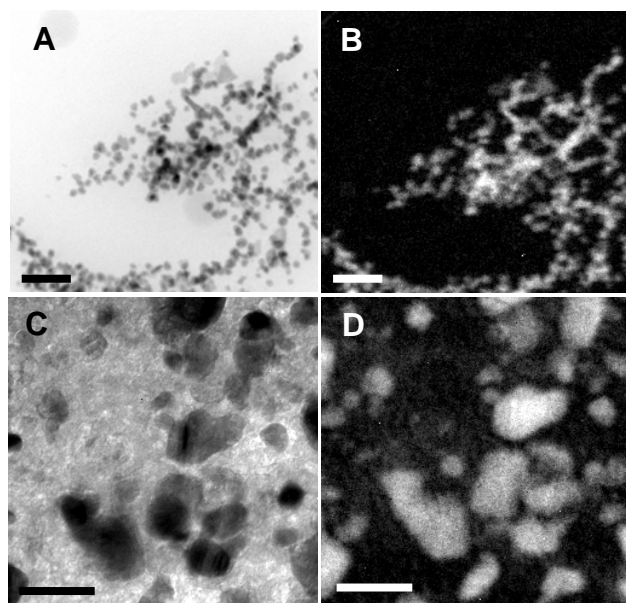


Figure 3.3 A) Bright-field image of pre-heat-treated sample, B) corresponding cobalt distribution image of (A), C) bright-field image of heat-treated sample and D) corresponding cobalt distribution image of (C). Scale bars = 100 nm

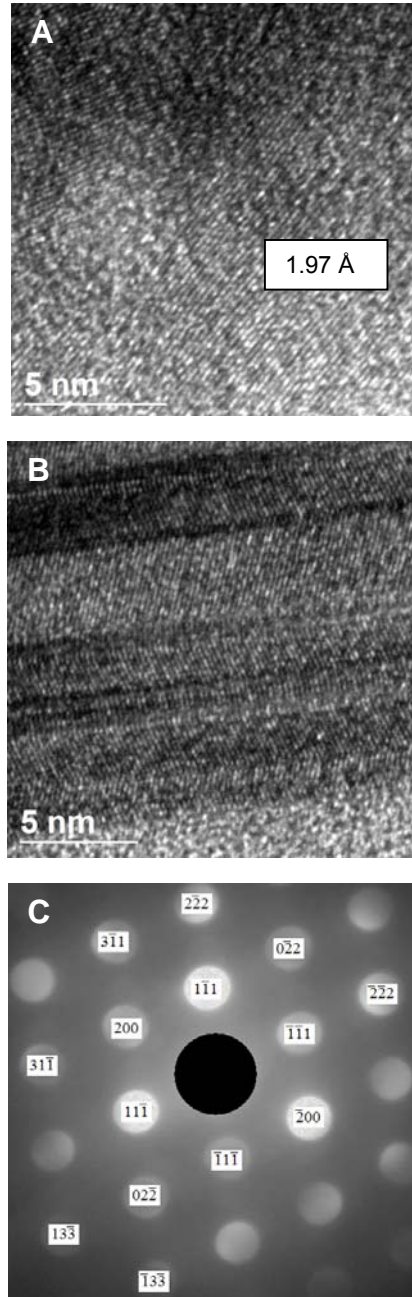


Figure 3.4 A) HRTEM of pre-heat-treated sample, B) HRTEM of heat-treated sample showing multiple twinning within a single crystal, C) indexed nano-beam electron diffraction pattern of $\langle 011 \rangle$ zone axis of fcc cobalt.

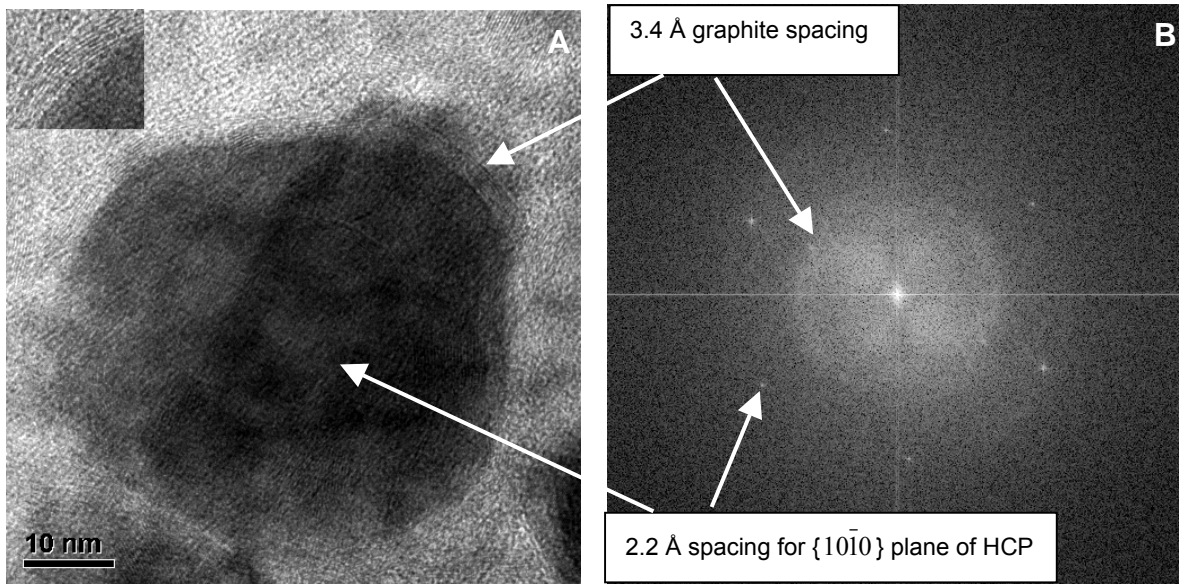


Figure 3.5 A) High-resolution image of hcp cobalt particle and B) Fourier transform of “A” showing graphite and hcp spacings. Inset in A is a magnified region of graphitic layers.

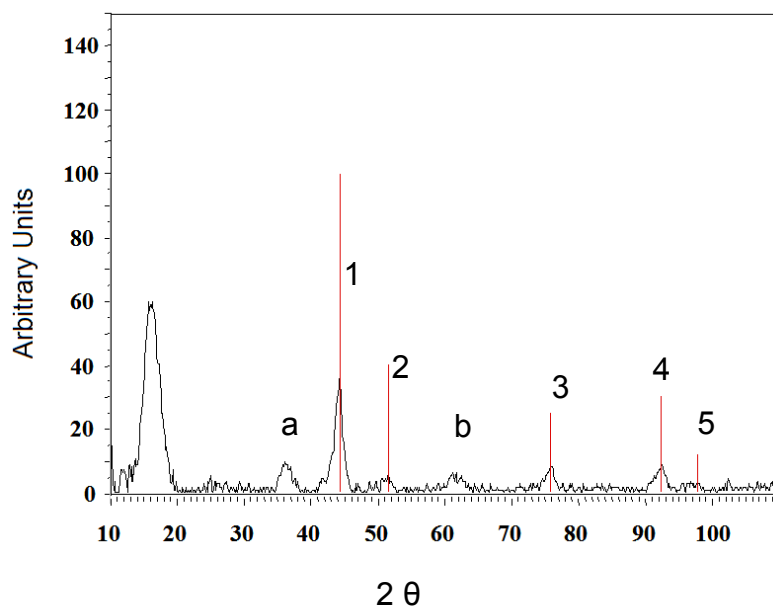


Figure 3.6 X-ray diffraction pattern for pre-heat-treated sample. Vertical lines are peak matches provided by the JCPDS software database.

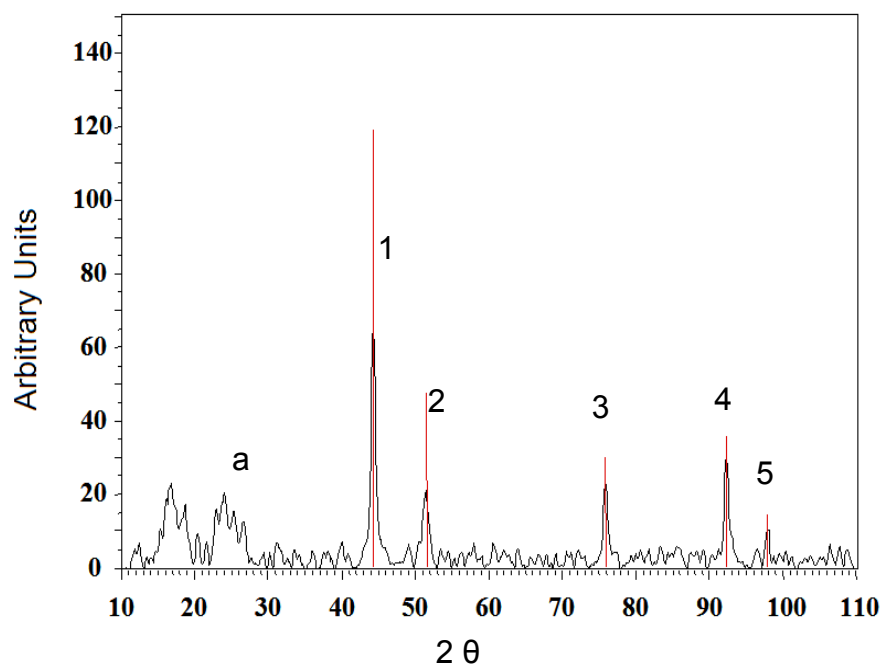


Figure 3.7 X-ray diffraction pattern for heat-treated sample. Vertical lines are peak matches provided by the JCPDS software database.

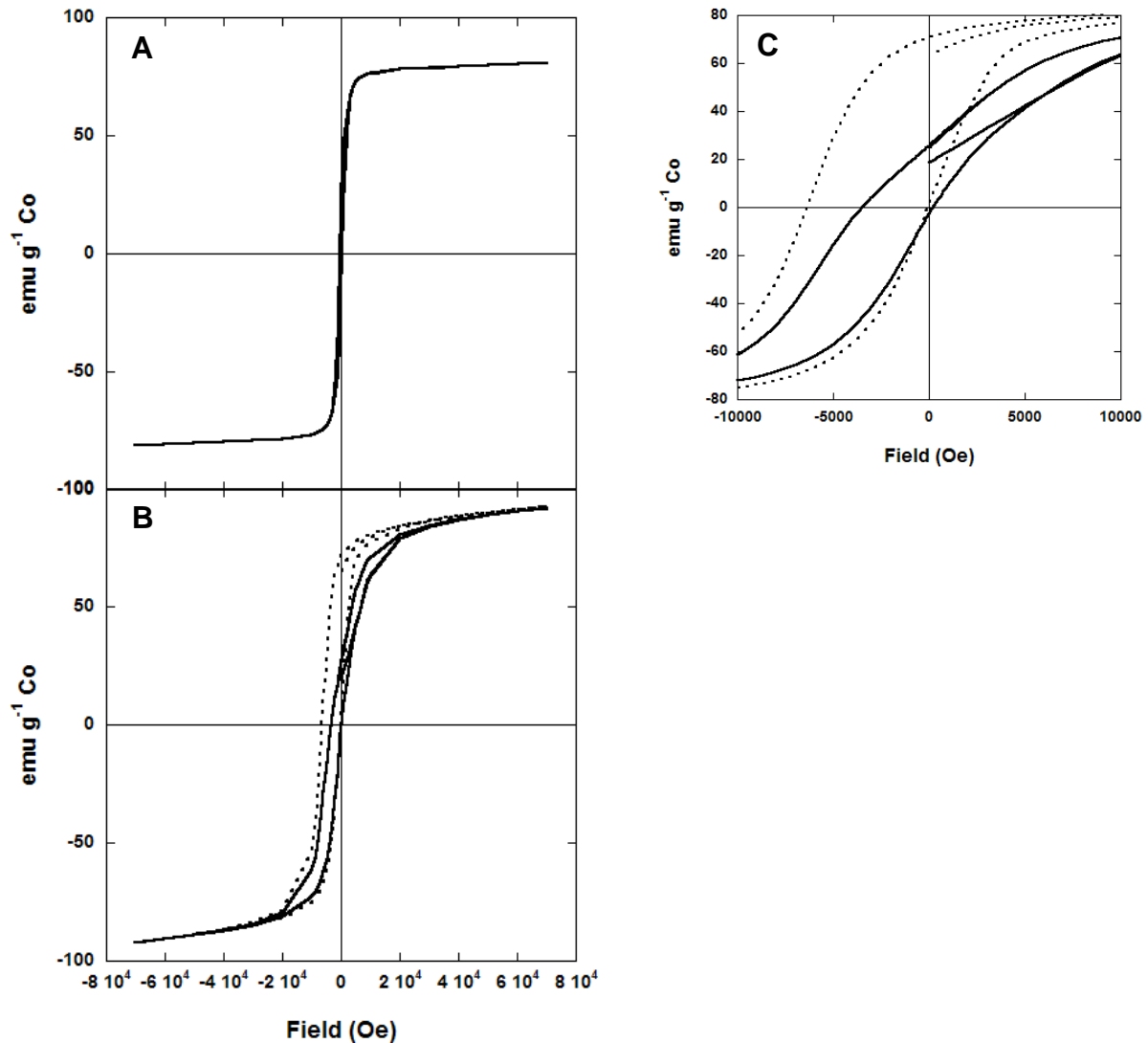


Figure 3.8 σ vs. H measurements conducted at A) 300 K and B) 5 K (zero-field cooled hysteresis loop —, field-cooled hysteresis loop •••) on pre-heat-treated cobalt-polymer complexes that had been aged under ambient conditions for three months. C) shows enlarged region around the origin for 5 K hysteresis loops showing the asymmetric field-cooled hysteresis loop shift.

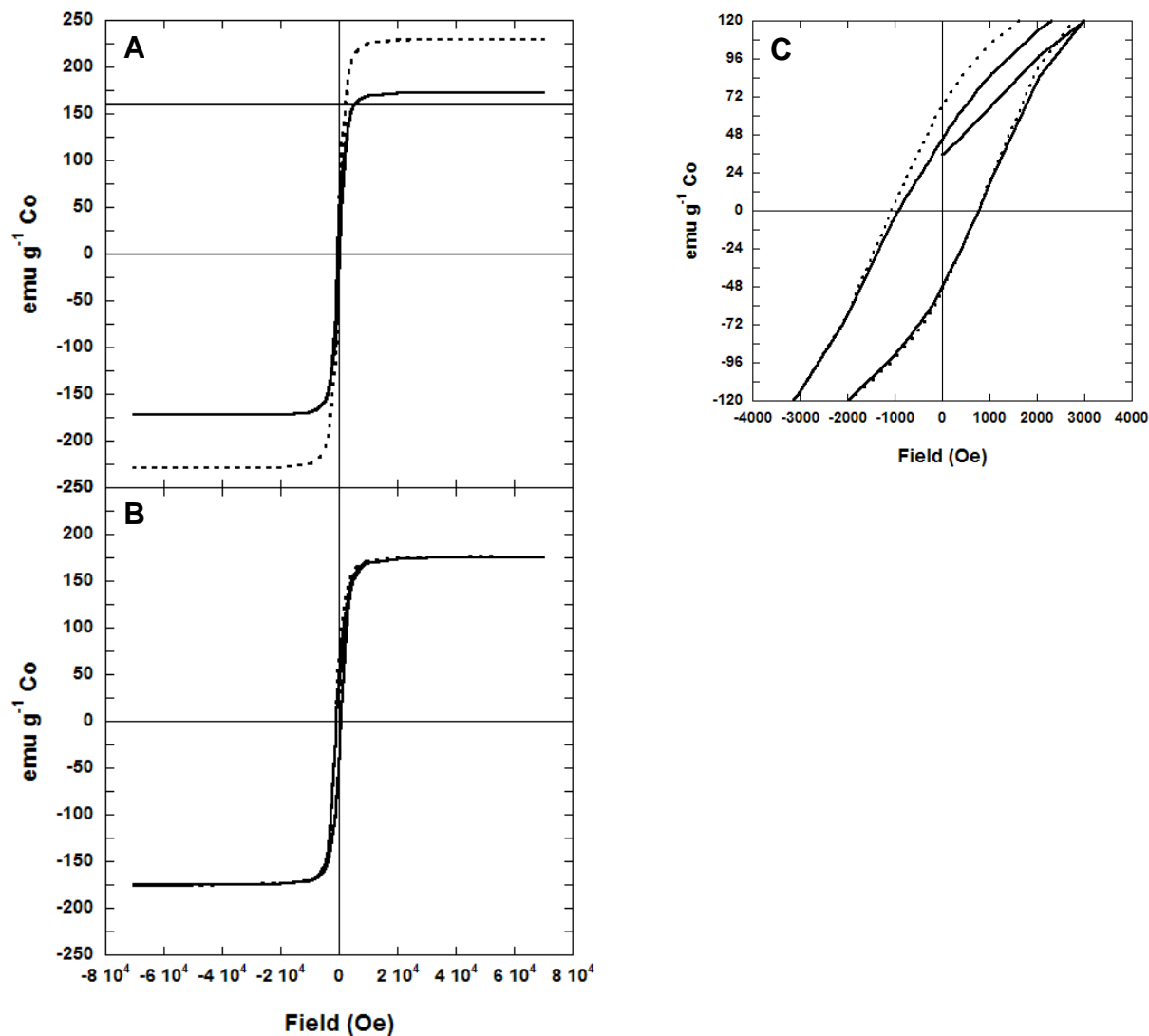


Figure 3.9 σ vs. H measurements conducted on a cobalt-copolymer sample that had been thermally treated at 700°C at A) 300 K (4 day acid digestion ($\bullet\bullet$) and 13 day acid digestion (—)) and B) 5 K (13 day acid digestion: zero field-cooled (—), field-cooled ($\bullet\bullet$)). C) shows enlarged region around the origin for 5 K hysteresis loops (13 day acid digestion) and shows minimal field-cooled hysteresis loop shift. The horizontal line at $160 \text{ emu g}^{-1} \text{ Co}$ in (A) indicates the maximum reported specific magnetization for cobalt metal.

CHAPTER 4. Structural and magnetic properties of as-prepared and heat treated cobalt nanoparticles stabilized with a siloxane-based block copolymer system

Michael A. Zalich,^{1,3} Michael L. Vadala,³ Judy S. Riffle,³ Martin Saunders,² Timothy G. St. Pierre^{1*}

¹School of Physics and ²Center for Microscopy and Microanalysis, The University of Western Australia, 35 Stirling Highway, Crawley WA 6009, Australia; ³Department of Chemistry and Macromolecules and Interfaces Institute, Virginia Polytechnic Institute and State University, Blacksburg, VA 24060, USA

4.1 Abstract

A stable dispersion of cobalt nanoparticles was prepared by the thermolysis of dicobalt octacarbonyl in a solution of poly(dimethylsiloxane-*b*-(methylvinylsiloxane-*co*-methyl(2-trimethoxysilyl)ethyl)siloxane)) (PDMS-*b*-(PMVS-*co*-PMTMS)). Two experiments were conducted, where different samples were heated in a quartz tube furnace at 600 or 700°C with the goal of creating an oxygen impermeable “silica” shell around the cobalt particles. The samples were characterized with a variety of analytical techniques to probe their physical properties. The heating process led to an increase in the cobalt specific saturation magnetization (σ_s) from 48 to 141 and 146 emu g⁻¹ Co for the 600 and 700°C processes respectively. Pre-heat-treated and heat-treated cobalt-copolymer complexes exposed to ambient conditions displayed a degree of oxidation. Particle size analyses indicated an increase in average particle size in the sample heated at 600°C compared with the pre-heat-treated sample; however, the sample heated at 700°C had a similar particle size distribution to the pre-heat-treated sample. Electron diffraction and x-ray diffraction data confirmed that the heat-treated cobalt nanoparticles were in the face-centered cubic phase, while the pre-heat-treated sample was weakly crystalline. Hence, the increase in σ_s from the pre-heat-treated sample to the heat-treated samples is most likely due to an improvement in particle crystallinity through the annealing process and less oxidation can possibly be attributed to partial protection by a ‘silica’ shell.

Keywords: cobalt, nanoparticles, TEM, SQUID, magnetic, diffraction

4.2 Introduction

One of the most exciting and rapidly growing areas of interest for magnetic nanoparticles is biomedicine. A number of current and potential applications for magnetic nanoparticles in medicine exist, ranging from MRI contrast enhancement agents¹³⁰ to tumor hyperthermia treatment.^{131, 132} Magnetite (Fe_3O_4) is a material of interest owing to its biocompatibility; however, the saturation magnetization of magnetite ($\sim 92 \text{ emu g}^{-1}$) compared to Fe^0 (218 emu g^{-1}) or Co^0 (161 emu g^{-1}) may not be sufficient for some applications.¹²⁹

It would be advantageous to protect zero-valent cobalt nanoparticles against oxidation by passivating the particles with a protective coating, thereby enabling their usage for biomedical applications. Cobalt metal is known to be toxic, so a protective coating may also serve to eliminate any toxicity associated with this type of system. Rutnakornpituk *et al.* and Stevenson *et al.* investigated the use of a siloxane based triblock copolymer (poly(dimethylsiloxane-*b*-(3-cyanopropyl)methylsiloxane-*b*-dimethylsiloxane) (PDMS-PCPMS-PDMS)), where the cyano groups were proposed to bind to the cobalt nanoparticles while the PDMS tail blocks sterically stabilized the particles in dispersion. A decrease in the cobalt specific magnetization over time was reported, owing to cobalt oxide formation.^{61, 62} Connolly *et al.* evaluated the magnetic properties of a pentablock copolymer (poly(dimethylsiloxane-*b*-methyltriethoxysilylethylsiloxane-*b*-(3-cyanopropyl)methyl siloxane-*b*-methyltriethoxysilylethylsiloxane-*b*-dimethylsiloxane) (PDMS-PMTEOS-PCPMS-PMTEOS-PDMS)), where the cyano groups of the central block were proposed to bind to the cobalt nanoparticles, the PMTEOS blocks were catalytically condensed to form a silica shell around the cobalt nanoparticles and the PDMS blocks sterically stabilized the nanoparticles in dispersion. Cobalt nanoparticles synthesized by the thermolysis of dicobalt octacarbonyl in pentablock micelles, where PDMS was the solvent, were oxidatively stable; however, a small amount of oxidation was detected when toluene was used as the solvent.⁶³ The copolymer system currently proposed (poly(dimethylsiloxane-*b*-(methylvinylsiloxane-*co*-methyl(2-trimethoxysilyl) siloxane)) contains trialkoxy functional groups, which bind to the cobalt nanoparticles¹³³ and possibly serve as precursors to a silica shell surrounding the particles.

Keller reported on the oxidative protection of carbon fibers by a poly(carborane-siloxane-acetylene) polymer system. The polymer was heated to form a crosslinked ceramic coating, which successfully protected the carbon fibers against oxidation at elevated temperatures (1000°C).¹³⁴ Although the proposed polymer in this research does not contain boron or

acetylene units, it is hypothesized that methoxy groups of the diblock copolymer will crosslink at elevated temperatures to generate a silica network around the cobalt nanoparticles. Michalet *et al.* reported on the pyrolysis of PDMS with Al and Al₂O₃ filler particles and described the process by which PDMS is converted into amorphous silica at temperatures above 200°C.¹³⁵ Finally, Scheffler *et al.* demonstrated the capacity for a mixed siloxane system comprised of PDMS, poly(methoxymethylsiloxane) and a Sn catalyst to crosslink at 1000°C under argon.¹³⁶

Herein, we discuss an attempt to prevent the oxidation of cobalt by heating cobalt nanoparticles coated with poly(dimethylsiloxane-*b*-(methylvinylsiloxane-*co*-methyl(2-trimethoxysilethyl)siloxane)) at 600 and 700°C. The research by Keller, Michalet *et al.* and Scheffler *et al.* suggests that the heat treatment of PDMS-*b*-(PMVS-*co*-PMTMS) coated cobalt nanoparticles may lead to amorphous silica coated cobalt nanoparticles, which may be protected from oxidation by a silica shell. The structural and magnetic properties of the cobalt nanocomposite materials before and after heat treatment were elucidated using transmission electron microscopy, electron diffraction, x-ray diffraction, small angle x-ray scattering and magnetic susceptometry.

4.3 Experimental

4.3.1. Synthesis of poly(dimethylsiloxane-*b*-(methylvinylsiloxane-*co*-methyl(2-trimethoxysilethyl)siloxane)) (PDMS-*b*-(PMVS-*co*-PMTMS).

A detailed synthetic procedure for (PDMS-*b*-(PMVS-*co*-PMTMS)) and the characterization of the precursors and final polymers have been reported previously.¹³³ Briefly, poly(dimethylsiloxane-*b*-methylvinylsiloxane) (PDMS-*b*-PMVS) was synthesized by the sequential addition of hexamethylcyclotrisiloxane (D_3) and 1,3,5-trivinyl-1,3,5-trimethylcyclotrisiloxane (D_v^3) monomers, initiated with *n*-butyllithium. After purification and characterization of the PDMS-*b*-PMVS copolymer, approximately half of the vinyl groups on the PMVS block were hydrosilated with trimethoxysilane to afford the final PDMS-*b*-(PMVS-*co*-PMTMS) block copolymer. The block copolymer used in this investigation had block lengths of 5000 and 3400 g mol⁻¹ for the PDMS and PMVS-*co*-PMTMS blocks respectively (Figure 4.1).

4.3.2 Synthesis of a cobalt nanoparticles.

Cobalt nanoparticles were synthesized by the addition of 1 g dicobalt octacarbonyl into a reaction vessel containing 1 g PDMS-*b*-(PMVS-*co*-PMTMS) in 20 mL of deoxygenated toluene. The reaction was refluxed at 110°C for 2 hours to evolve most of the carbon monoxide ligands. After cooling, a stable magnetic dispersion of cobalt nanoparticles resulted. Toluene was removed under vacuum to provide a dried sample for characterization (referred to as **N1a**). **N1a** was analyzed 4 months after being synthesized. Two other samples synthesized using the same procedure as **N1a** were prepared and immediately exposed to heat-treatments (referred to as virgin samples of **N1a**).

4.3.3 Heat treatment of PDMS-*b*-(PMVS-*co*-PMTMS) coated cobalt nanoparticles.

A virgin sample of **N1a** was transferred (with limited exposure to air) onto a ceramic boat and inserted into a quartz tube furnace. One sample was heated to and held at 600°C for 4 hours (referred to as **P1a**) under a flow of argon gas. Another virgin sample of **N1a** was heated at 700°C for 2 hours (referred to as **P2a**) under the same conditions. After heating, the samples were removed from the tube furnace and placed into separate sample vials under argon. Samples **P1a** and **P2a** were ground immediately before magnetic susceptometry measurements were conducted.

4.3.4 Exposure of samples to ambient conditions.

Each sample (**N1a**, **P1a**, **P2a**) was exposed to air and subsequently analyzed by magnetic susceptometry. **N1a** was exposed for an additional 11-month period (total exposure time was 15 months), **P1a** was exposed for 8 months after the initial grinding and **P2a** was exposed for 10 days after the initial grinding. The results for the exposed samples (**N1b**, **P1b**, **P2b**) were compared with results for **N1a**, **P1a** and **P2a** to evaluate the oxidative stability of the cobalt-copolymer complexes over time.

4.3.5 Transmission Electron Microscopy.

Transmission electron microscopy (TEM), high-resolution TEM, energy-filtered TEM, selected area electron diffraction (SAD) and nano-beam electron diffraction (NBD) were conducted with a JEOL 3000F field-emission transmission electron microscope (operated at 300

kV) equipped with a Gatan image filter (GIF) and digital imaging system. **N1a**, **P1a** and **P2a** were embedded in resin and microtomed to a thickness of ~ 100 nm. Microtomed slices were then placed onto amorphous carbon coated copper grids for analysis. NBD was conducted on single crystals of **P1a** with an ~ 2 nm focused electron beam. Particle size analysis was performed on two fields of view for each sample. Each field of view was divided into sections and all of the particles of a particular section were measured in two directions: 1) in any obvious long direction and 2) perpendicular to the first measurement. The two measurements for each particle were then averaged and the aspect ratio for each particle (longer measurement/shorter measurement) was calculated. The mean and standard deviation were calculated for the particle size and aspect ratio for both fields of view of each sample. Energy-filtered TEM was conducted using the GIF with slit widths of 40 eV at the cobalt $L_{3,2}$ edge (778-793 eV). Pre-edge background images were acquired at 714 and 754 eV, while the post-edge image was acquired at 799 eV.

4.3.6 X-ray Diffraction.

A Siemens D-500 x-ray diffractometer (Cu-K α radiation) was used to acquire x-ray diffraction patterns of the samples before and after heat treatment. Powdered samples were placed onto poly(carbonate) sample holders and scanned at: 1) a rate of 0.2°/min with a step size of 0.03° from 10-110° for **N1a** and **P2a** and 2) a rate of 0.266°/min with a step size of 0.03° from 20-100° for **P1a**.

4.3.7 Magnetic Susceptometry.

A Quantum Design magnetic properties measurement system (MPMS-7) equipped with a superconducting quantum interference device (SQUID) sensor was used to make cobalt specific magnetization measurements (σ) at varying applied fields (H) from $-70,000$ to $+70,000$ Oe at 300 K and 5K, with 100 Oe spacings between -1000 Oe and 1000 Oe. Low-temperature measurements were conducted both after cooling the sample in zero applied field and in an applied field of 70,000 Oe. The purpose of the different measurements was to study: 1) the saturation magnetization at 300 K, 2) the hysteretic behavior of the sample at 300 K, 3) the presence of an exchange bias owing to a cobalt oxide layer on the surface of the cobalt nanoparticles, and 4) the presence of paramagnetic species owing to any residual cobalt carbonyl

species in the sample. The samples were prepared by crushing the sample into a powder using a spatula and placing 10 to 20 mg of the sample into an acid-washed Teflon sample holder.

4.3.8 Elemental Analysis.

Elemental analyses were performed on the pre-heat-treated and heat-treated samples (**N1a**, **P1a**, **P2a**) using inductively coupled plasma atomic emission spectroscopy (ICP-AES) at the Marine and Freshwater Research Laboratory at Murdoch University, Perth, Western Australia. The samples were prepared by digestion in a 1:1 mixture of HNO₃:H₂SO₄ for 14 days at 70-100°C. The samples and a blank were diluted and analyzed for cobalt concentrations.

4.4 Results and Discussion

4.4.1 Transmission Electron Microscopy.

Transmission electron microscopy (TEM) was used to study the particle size, size distribution, morphology, chemical composition and crystallinity of the pre-heat-treated and heat-treated cobalt-polymer complexes. A ‘particle’ was deemed to be a region with contrast obviously different from the background. The particle size distribution for the pre-heat-treated sample (**N1a**) ranged from 8 to 38 nm with a mean of 14.1 nm and mode of 12.5 nm (sample population = 536 particles) (Figure 4.2A). The mean aspect ratio for particles of the pre-annealed sample was 1.51 with a standard deviation of 0.46. A dramatic difference in particle size and size distribution after thermal treatment at 600°C (**P1a**) was apparent from the images taken during analysis. There were two different populations of particles, which resulted in a bimodal particle size distribution (modes at ~ 10 and 120 nm). The particle size distribution for **P1a** ranged from 4 to 750 nm with a mean of 91 nm (sample population = 399 particles) (Figure 4.2B). The mean aspect ratio for the smaller particles was 1.61 with a standard deviation of 0.5, while the mean aspect ratio for the larger particles was 2 with a standard deviation of 0.9. Thermal treatment of **N1a** at 700°C to produce **P2a** resulted in a narrow particle size distribution, similar to that of **N1a**. The particle size for **P2a** ranged from 4 to 21 nm with a mean of 10.1 nm and a mode of ~9.5 nm (sample population = 310 particles) (Figure 4.2C). The mean aspect ratio was 1.37 with a standard deviation of 0.34. It is proposed that thermal treatment at 600°C leads to cobalt particle aggregation and possibly sintering during the pyrolysis of the polymer. In some cases particle aggregates probably occur before the polymer is completely pyrolyzed,

which leads to large aggregates of fused cobalt nanoparticles. However, it appears that a more rapid pyrolysis of the polymer, such as may be achieved at 700°C, may prevent the cobalt particles from coming into contact with one another and sintering during the pyrolysis step. Jacobsohn *et al.* reported the increase in size of ion-implanted cobalt nanoparticles in a fused silica matrix after annealing at 900°C under vacuum for 10 hours.¹³⁷ The system reported by Jacobsohn *et al.* is different from the system discussed here; nevertheless, the particle growth mechanism seems similar. In the **P2a** system, it is possible that the polymer readily pyrolyzes at the higher temperature (700°C) before the cobalt particles can come into contact. Thus, the particles are separated by a ‘silica’ matrix and the average particle size and size distribution remain narrow as in the pre-heat-treated sample.

Energy filtered TEM (EFTEM) was conducted on **N1a**, **P1a** and **P2a** to confirm the elemental identity of the electron dense nanoparticles. The cobalt distribution maps correlated well with the electron dense regions of the bright-field images, confirming that the dense particles in these systems were indeed the cobalt nanoparticles (Figure 4.3).

High-resolution transmission electron microscopy (HRTEM) was implemented to evaluate the crystallinity of the cobalt nanoparticle complexes. Although **N1a** was weakly crystalline, several high-resolution images were obtained. Figure 4.4A shows a crystalline particle of **N1a** with measured lattice spacings of ~2.01 Å, which are consistent with {111} plane of fcc cobalt (2.05 Å), but could be the {002} plane of hcp cobalt (2.02 Å). A HRTEM image of **P1a** provided evidence of the hcp structure of cobalt. Figure 4.4B is a high-resolution image of **P1a** with the arrows normal to the {100} and {002} lattice planes of hcp cobalt. Nevertheless, nano-beam electron diffraction (NBD) (Figure 4.4C) and selected area electron diffraction (SAD) of **P1a** provided evidence for the fcc structure of cobalt (Table 1). A high-resolution image of a multi-twinned **P2a** particle gives spacings of ~2.04 Å for two twin planes, which is consistent with the {111} of fcc cobalt (2.05 Å) (Figure 5A). Multiple twinning is common in fcc materials¹²³ and has been reported for cobalt nanocrystals.⁵¹ Additional measurements of the Fourier transform of the lower twin in Figure 4.5A (~1.83 and 1.06 Å) are consistent with the {200} and {311} lattice planes of fcc cobalt (1.77 and 1.07 Å) (Figure 4.5B). SAD supports the HRTEM data for **P2a**, by also indicating the presence of fcc cobalt (Table 1).

4.4.2 X-ray diffraction.

X-ray diffraction was used to complement electron diffraction as it provides crystallographic information on the bulk of the sample. Sample **N1a** was only weakly crystalline as indicated by the diffraction pattern (Figure 4.6A). Some intense reflections were present at 2θ values of 41.3, 44.7 and 47.4° corresponding to experimental d-spacings of 2.19, 2.03 and 1.92 Å respectively. These values match well with literature d-spacings for hexagonal close packed (hcp) cobalt of 2.17, 2.04 and 1.92 Å respectively. However, the experimental intensities do not follow the same trend as the literature intensities. The energetic difference in atomic stacking between the three known phases of cobalt (fcc, hcp and epsilon) is low; therefore, having multiple phases of cobalt is possible.^{47, 121} Sample **P1a** exhibited intense reflections at 2θ values of 44.1, 51.5, 75.7 and 92.1° corresponding to d-spacings of 2.05, 1.77, 1.25 and 1.07 Å respectively. These experimental values match well with the literature values for the {111}, {200}, {220} and {311} lattice planes of fcc cobalt (Figure 4.6B). Other peaks are present, which are less intense but may indicate the presence of other phases. Nevertheless, it is clear that the dominant phase of cobalt in **P1a** is fcc. Sample **P2a** was similar to **P1a** with major reflections at 2θ values of 44.4, 52, 76 and 92° corresponding to d-spacings of 2.03, 1.76, 1.25 and 1.07 Å respectively. These reflections, although broader than **P1a**, matched the literature values for fcc cobalt (Figure 4.6C). Qualitative peak broadening calculations were performed for **P1a** and **P2a** using the Scherrer equation. The increase in breadth for **P2a** peaks compared with **P1a** peaks is consistent with particle size data obtained from TEM analysis, which indicated a smaller mean particle size for **P2a** relative to **P1a**.

4.4.3 Magnetic Susceptometry.

Room temperature σ vs. H measurements of **N1a** revealed a cobalt specific saturation magnetization (σ_s) of 48 emu g⁻¹ Co, which is significantly less than the 161 emu g⁻¹ value reported for bulk cobalt.¹²⁹ Moreover, **N1b** had a similar value of 47 emu g⁻¹ Co, indicating that no further oxidation had taken place after exposing the sample for 15 months to ambient conditions (Figure 4.7 A). σ_s for **N1a** and **N1b** remained constant irrespective of exposure time (4 months for **N1a** and 15 months for **N1b**), which suggests that the sample reached the maximum extent of oxidation in 4 months and prolonged exposure did not serve to enhance the oxidation process. In addition, neither of the **N1** materials displayed significant remanence or

coercivity. Room temperature magnetization curves almost saturate in high applied fields, while 5 K magnetization curves have a positive slope in high applied fields. The positive slope in the low temperature magnetization curves suggests the presence of a paramagnetic component in the sample. The paramagnetic component is believed to be unreacted cobalt carbonyl species that were not incorporated into the cobalt nanocrystals during the thermolysis procedure. A slight shift of the field-cooled hysteresis loop with respect to the zero field-cooled hysteresis loop was noticed for the **N1a** sample ($H_e \sim 460$ Oe), which is indicative of an exchange bias interaction between an antiferromagnetic cobalt oxide surface layer and a ferromagnetic cobalt metal core (Figure 4.7B).^{126, 127} The exchange bias (H_e) for the **N1b** sample increased to ~ 1100 Oe, suggesting that more cobalt oxide is present or a stronger coupling between the cobalt oxide and cobalt occurred despite no significant decrease in σ_s at room temperature. There was a difference in 11 months between measurements of the **N1a** and **N1b** samples, and the **N1a** sample displayed signs of a slight oxide layer. It is possible that the cobalt oxide layers coupled with the cobalt particles increased their interfacial order over time and hence strengthened the exchange interaction between the cobalt oxide layer and cobalt core of the nanoparticles. σ vs. T measurements indicated that the maximum blocking temperature of the **N1** system was near room temperature.

Room temperature σ vs. H measurements for **P1a** and **P1b** indicated values of 141 and 91 $\text{emu g}^{-1} \text{Co}$ for σ_s respectively (Figure 4.8A). Both magnetization curves for **P1** almost saturate in high-applied fields at room temperature, but have a slight positive slope in high-applied fields at 5K. A proposed explanation for the slight positive slope in both **P1** hysteresis loops at 5K is the paramagnetic behavior of cobalt atoms that have not been incorporated into cobalt nanocrystal lattices. The elevated heat treatment would have eliminated any remaining carbonyl ligands; however, it is possible that the polymer pyrolyzes before all of the cobalt atoms (that were in the form of cobalt carbonyl species in **N1**) could diffuse through the system to become part of cobalt nanocrystals. Furthermore, H_e increased from ~ 50 Oe for **P1a** to ~ 350 Oe for **P1b** (Figure 4.8C). The negligible magnitude of H_e in **P1a** suggests that oxidation had not taken place prior to grinding the sample or during the measurements. This data suggests that the sample in its un-ground state is adequately protected against oxidation. Exposure of ground **P1** to air for an 8-month period resulted in the formation of a detectable amount of cobalt oxide as indicated by both the increased H_e and reduced σ_s for **P1b**. The grinding process appears to

fracture the brittle silica coating formed around the nanoparticles during thermal treatment, thus exposing bare cobalt. Bare cobalt nanoparticles readily oxidize upon exposure to air, which is manifested by a decrease in σ_s and an increase in H_e . σ vs. T measurements indicated that the maximum blocking temperature for the **P1** system was near room temperature.

Room temperature σ vs. H measurements for **P2a** yielded a σ_s value of 146 emu g⁻¹ Co. There is a slight, but most likely insignificant, increase of 5 emu g⁻¹ Co in σ_s from **P1a** to **P2a**. The increase may be due to more perfect cobalt crystals in the **P2a** sample compared with the **P1a** sample; however, the results may be within experimental error of the elemental analysis data. **P2b** had a decreased σ_s value of 91 emu g⁻¹ Co, indicating that oxidation of the ground complex had taken place during exposure to air (Figure 4.9A). Low temperature σ vs. H measurements indicated a negligible field-cooled hysteresis loop shift in **P2a** ($H_e \sim 70$ Oe), but an increased value for **P2b** ($H_e \sim 125$ Oe) also indicating that oxidation has taken place (Figure 4.9B). The difference in magnitude of H_e for the **P2** samples is not comparable with the difference in the **P1** samples. This may be explained using the same hypothesis proposed for the increase in H_e over time in the **N1** samples. Perhaps the antiferromagnetic layers in the **N1** and **P1** samples had significant time to increase their interfacial order, leading to an increased exchange interaction between the antiferromagnetic cobalt oxide surface layers and the ferromagnetic cobalt cores. **P2b** was analyzed only 10 days after the initial grinding and a drastic decrease in σ_s was observed, albeit without a dramatic increase in H_e . With a longer aging time, it is expected that H_e for **P2b** will increase as the cobalt oxide surface layers improve their interfacial order with the cobalt cores. The magnetization curves for both samples of **P2** almost saturate in high-applied fields at room temperature, but have a slight positive slope in high-applied fields at 5K. The same explanation proposed for the positive slope in the **P1** 5K hysteresis loops also applies to the **P2** 5K hysteresis loops, as the proposed trapping mechanism of paramagnetic cobalt atoms is controlled by the pyrolyzed state of the polymer. The positive slope exhibited in both **P1** and **P2** 5K hysteresis loops is significantly smaller than the positive slope of the **N1** 5K hysteresis loops, implying that most cobalt atoms have been incorporated into cobalt crystals. σ vs. T measurements indicated the maximum blocking temperature of the **P2** system was near room temperature.

4.5 Conclusions

Cobalt nanoparticles were synthesized by thermally decomposing $\text{Co}_2(\text{CO})_8$ in poly(dimethylsiloxane-*b*-(methylvinylsiloxane-*co*-methyl(2-trimethoxysilyl)ethyl)siloxane) block copolymer micelles. Subsequent heat treatment of the nanoparticles at 600°C led to an increased particle size distribution compared with the pre-heat-treated sample, while heat treatment at 700°C afforded a particle size distribution similar to the pre-heat-treated sample. σ_s was greater for the heat-treated samples owing to an increase in particle crystallinity resulting from annealing of the cobalt nanoparticles. Transmission electron microscopy, electron diffraction and x-ray diffraction were used to identify the dominant crystal phase of the heat-treated samples as being face-centered cubic, although HRTEM analysis indicated the presence of hcp cobalt in the 600°C heat-treated sample. Magnetic susceptometry indicated that the pre-heat-treated sample was not oxidatively stable. The heat-treated samples were oxidatively stable until they were ground. The grinding procedure may have fractured the silica coatings, which exposed bare cobalt and ultimately led to cobalt nanoparticle oxidation.

Future work will focus on creating an oxygen impermeable barrier around discrete, annealed cobalt nanoparticles. In addition, cobalt nanoparticles coated with a silica shell provide a means for functionalization of the surfaces of these nanoparticles, which we have already demonstrated and will pursue further.¹³⁸

4.6 Acknowledgements

The authors of this paper acknowledge the support of NSF under contract DMR-0312046, DARPA-AFOSR (contracts #F49620-02-1-0408 and F49620-03-1-0332), OMNOVA Solutions and the Australian Research Council (grant # DP0559333) for funding. M. A. Zalich thanks the Australian-American Fulbright Commission for a Fulbright Postgraduate Fellowship to conduct research in Australia. The authors would also like to thank Dr. J. Connolly and C. Maitland from Curtin University of Technology, Perth, Australia for help with SAXS data acquisition and E. Bovell from The University of Western Australia for help with SAXS curve fitting.

*Corresponding author: A/Prof Timothy G. St. Pierre, School of Physics, The University of Western Australia, Crawley, WA, 6009, Australia. Ph: +61 8 6488 2747; Fax: +61 8 6488 1879; e-mail: stpierre@physics.uwa.edu.au

Table 4.1 Comparison of Experimental d-spacing ratios from SAD patterns for **P1a** and **P2a** with Literature fcc cobalt d-spacing ratios ¹

	Ratio of lattice planes	Experimental	Literature
P1a	{111}:{200}	1.15	1.15
	{200}:{220}	1.41	1.41
	{220}:{311}	1.19	1.17
	{111}:{220}	1.63	1.63
	{111}:{311}	1.94	1.91
P2a	{111}:{200}	1.15	1.15
	{200}:{220}	1.42	1.41
	{220}:{311}	1.17	1.17
	{311}:{222}	1.05	1.04

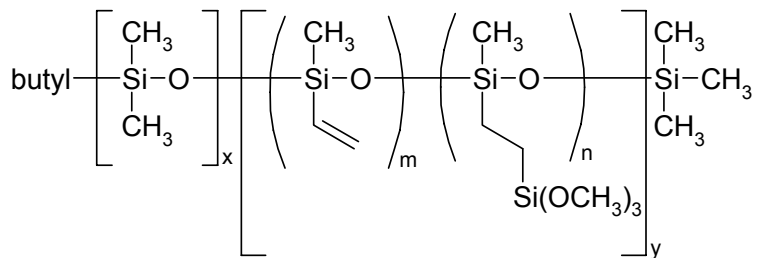


Figure 4.1 PDMS-*b*-(PMVS-*co*-PMTMS)

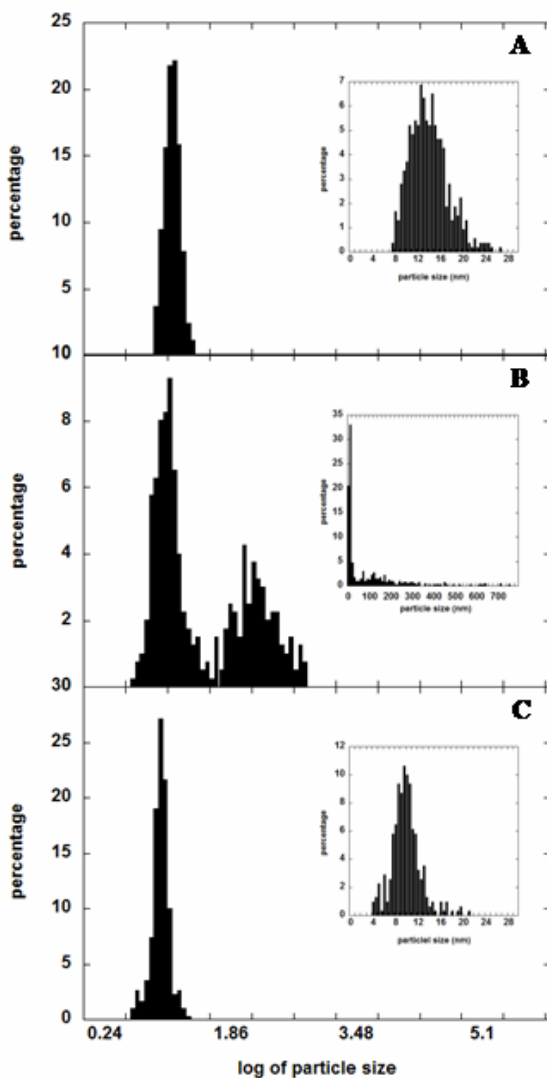


Figure 4.2 Logged particle size histograms for: A) pre-heat-treated sample (N1a), B) sample heated at 600°C (P1a) and C) sample heated at 700°C (P2a). Insets show particle size histograms in nm. Note: The raw data was logged and re-binned to generate the logged particle size histograms.

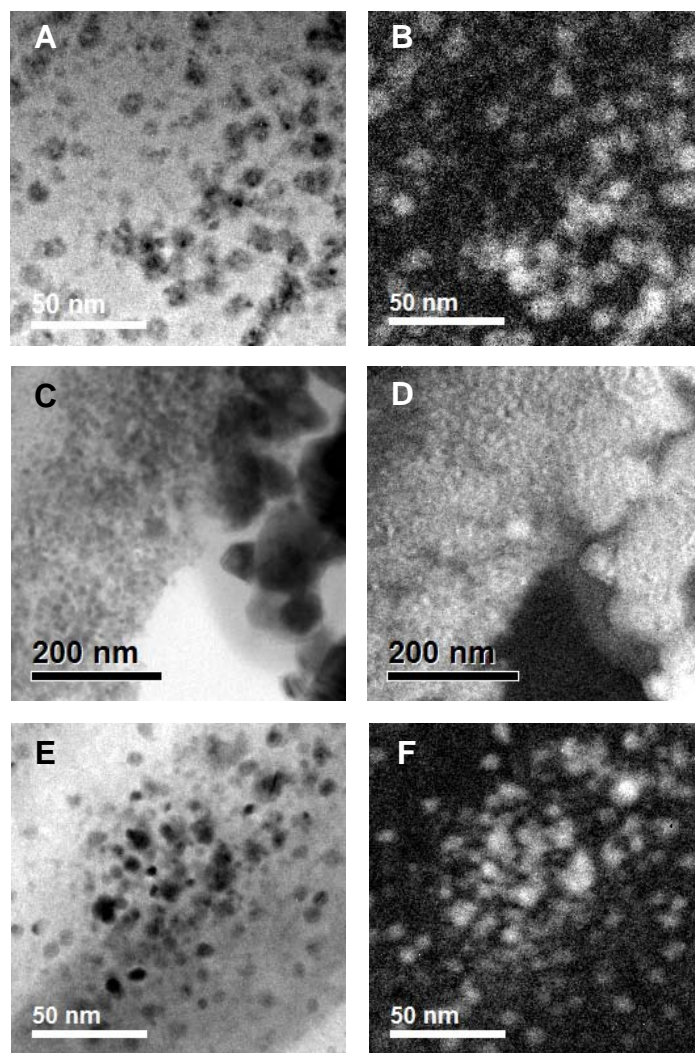


Figure 4.3 A) bright field image of **N1a**, B) corresponding Co elemental map of A, C) bright field image of **P1a**, D) corresponding Co elemental map of C, E) bright field image of **P2a** and F) corresponding Co elemental map of E.

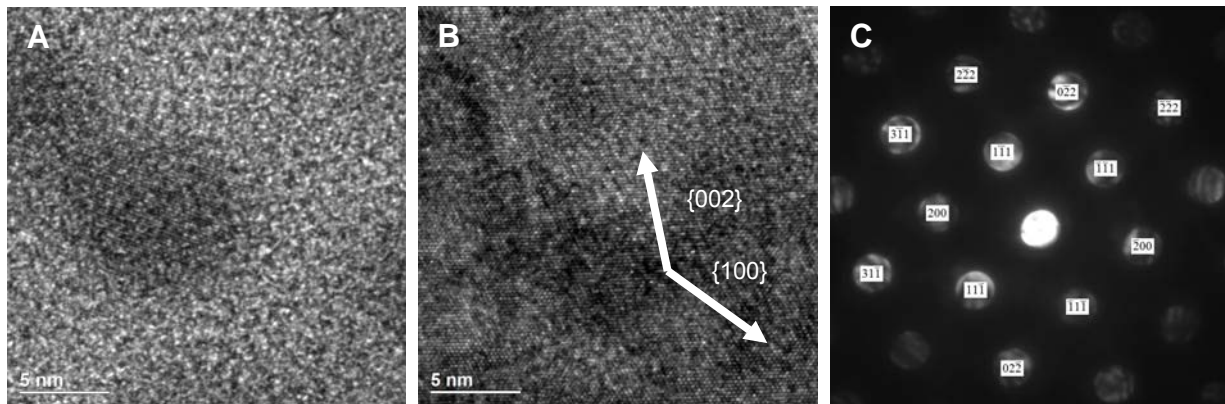


Figure 4.4 A) HRTEM image of pre-heat-treated sample (**N1a**), B) HRTEM image of sample heat-treated at 600°C (**P1a**) showing lattice planes consistent with hcp cobalt structure (arrows normal to denoted lattice planes) and C) nano-beam electron diffraction of **P1a** showing $\langle 011 \rangle$ zone axis of fcc cobalt.

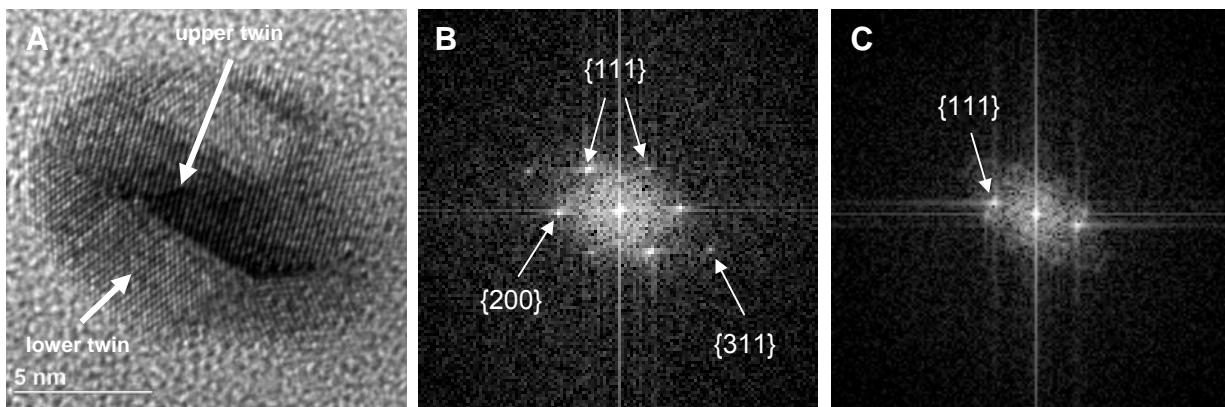


Figure 4.5 A) HRTEM image of multi-twinned **P2a** particle showing lattice planes consistent with fcc cobalt structure, B) Fourier transform of lower twin in image A and C) Fourier transform of upper twin in image A.

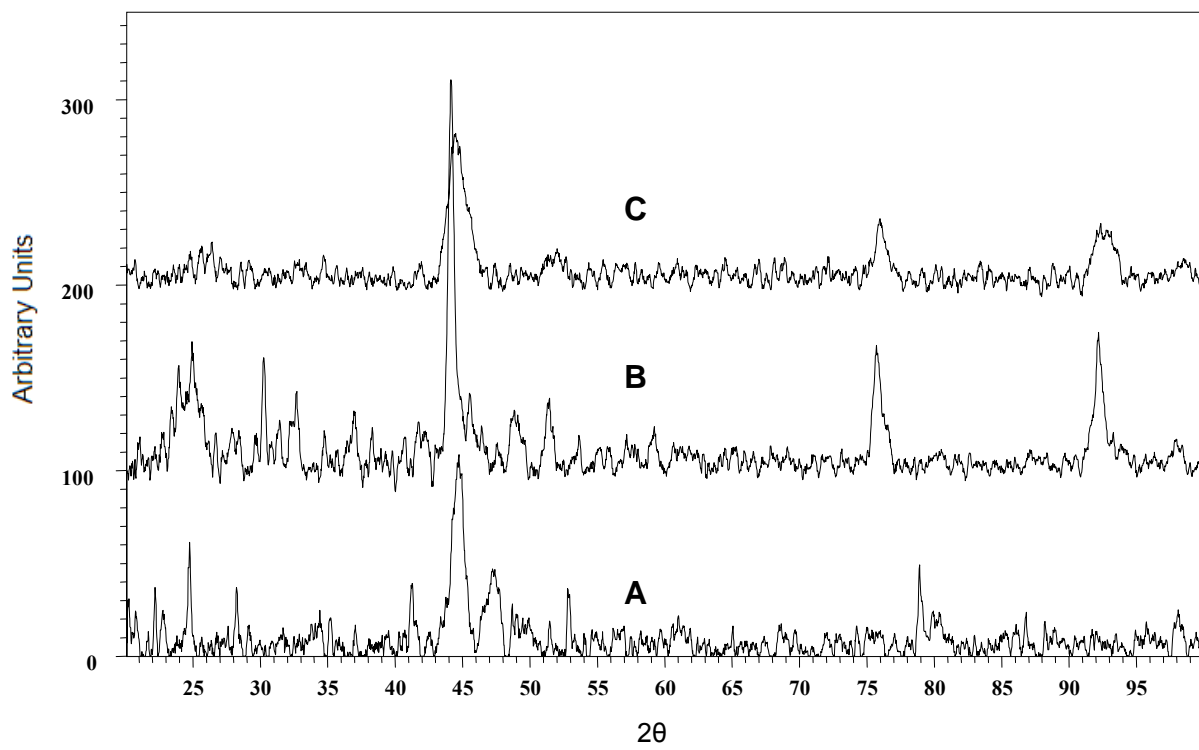


Figure 4.6 X-ray powder diffraction patterns for A) **N1a**, B) **P1a** and C) **P2a**

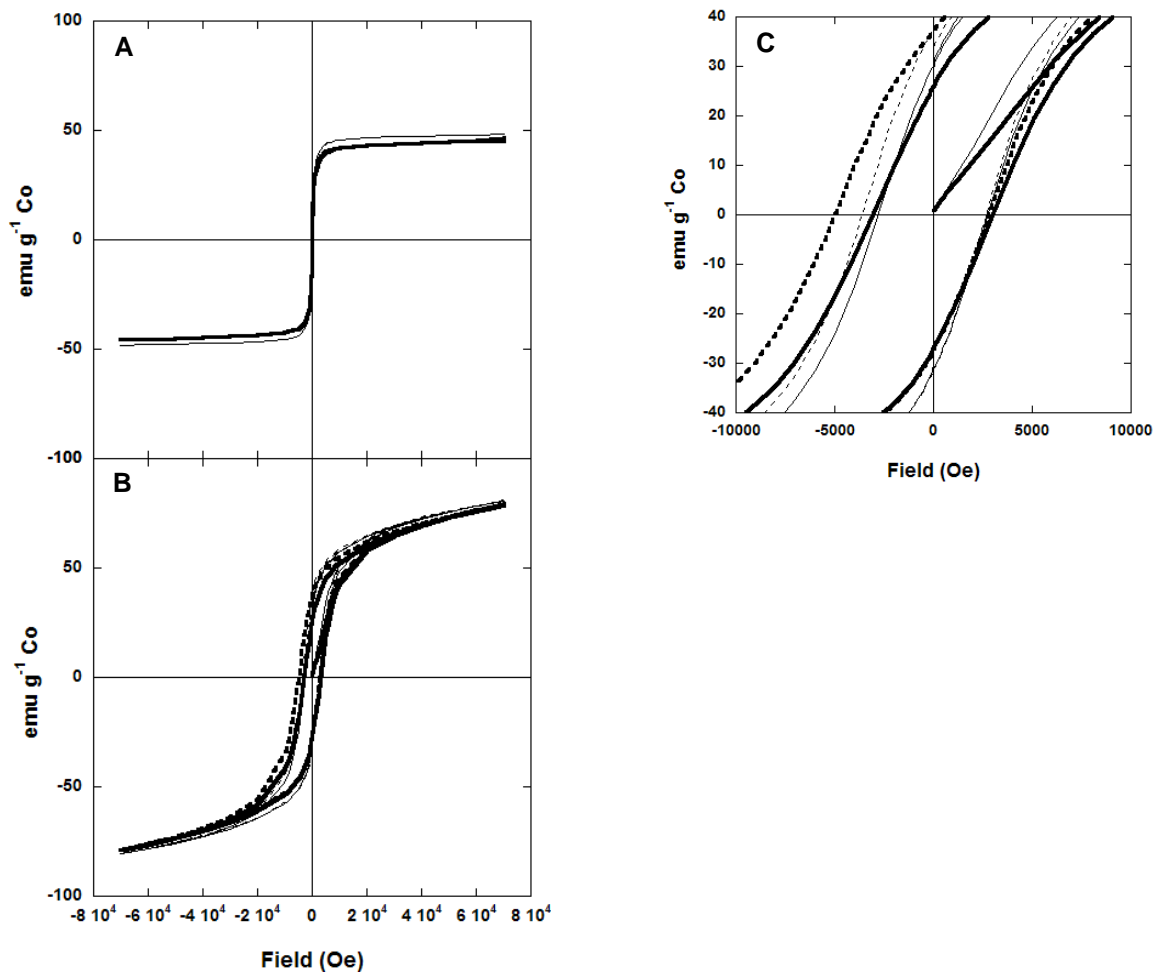


Figure 4.7 σ vs. H measurements conducted on **N1** at A) 300 K (— **N1a**; — **N1b**) and B) 5 K (**N1a**: zero-field cooled hysteresis loop —, field cooled hysteresis loop ---; **N1b**: zero-field cooled hysteresis loop —, field cooled hysteresis loop ---). C) shows enlarged region around the origin for 5K hysteresis loops showing asymmetric field-cooled hysteresis loop shift.

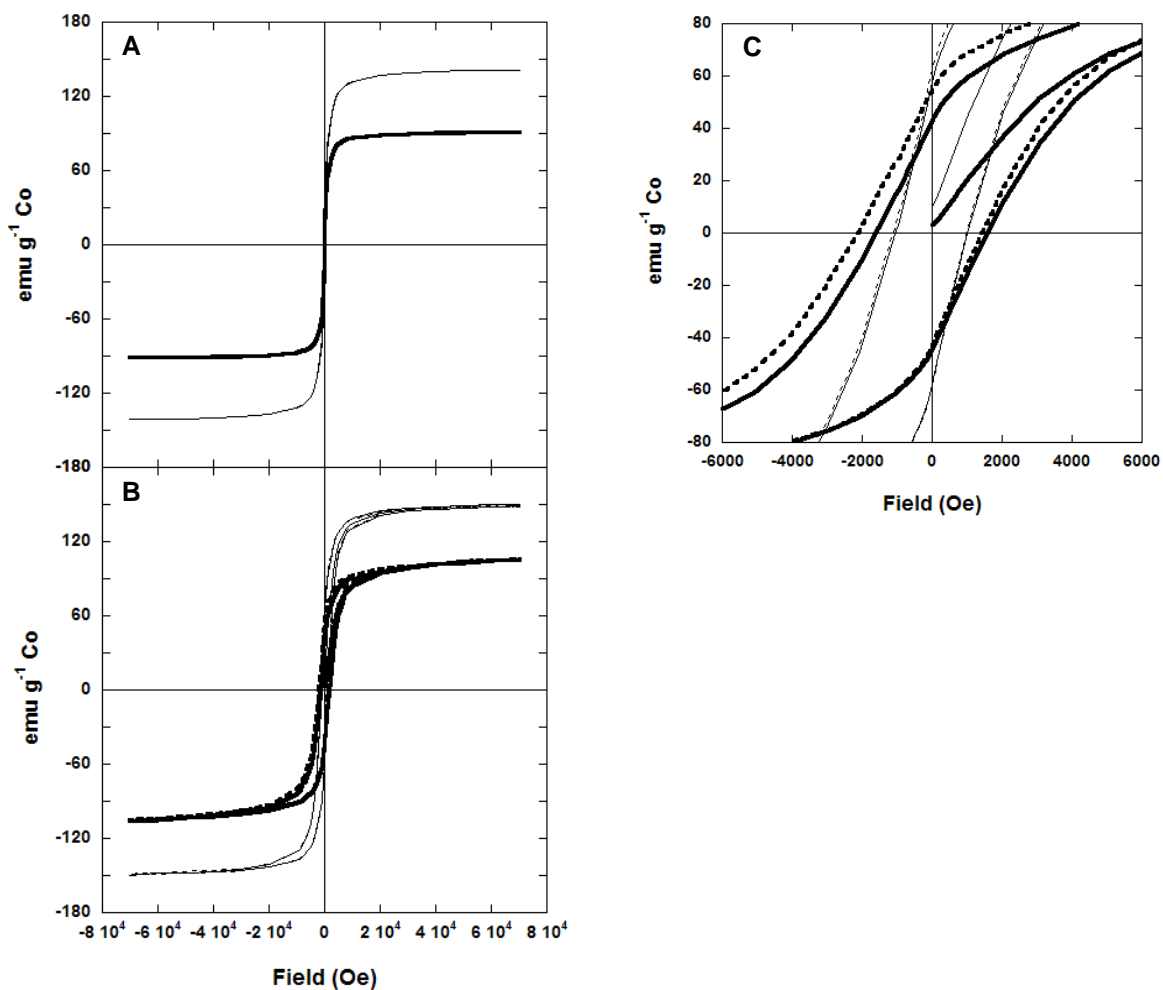


Figure 4.8 σ vs. H measurements conducted on **P1** at A) 300 K (— **P1a**; — **P1b**) and B) 5 K (**P1a**: zero-field cooled hysteresis loop —, field cooled hysteresis loop ---; **P1b**: zero-field cooled hysteresis loop —, field cooled hysteresis loop ---). C) shows enlarged region around the origin for 5K hysteresis loops.

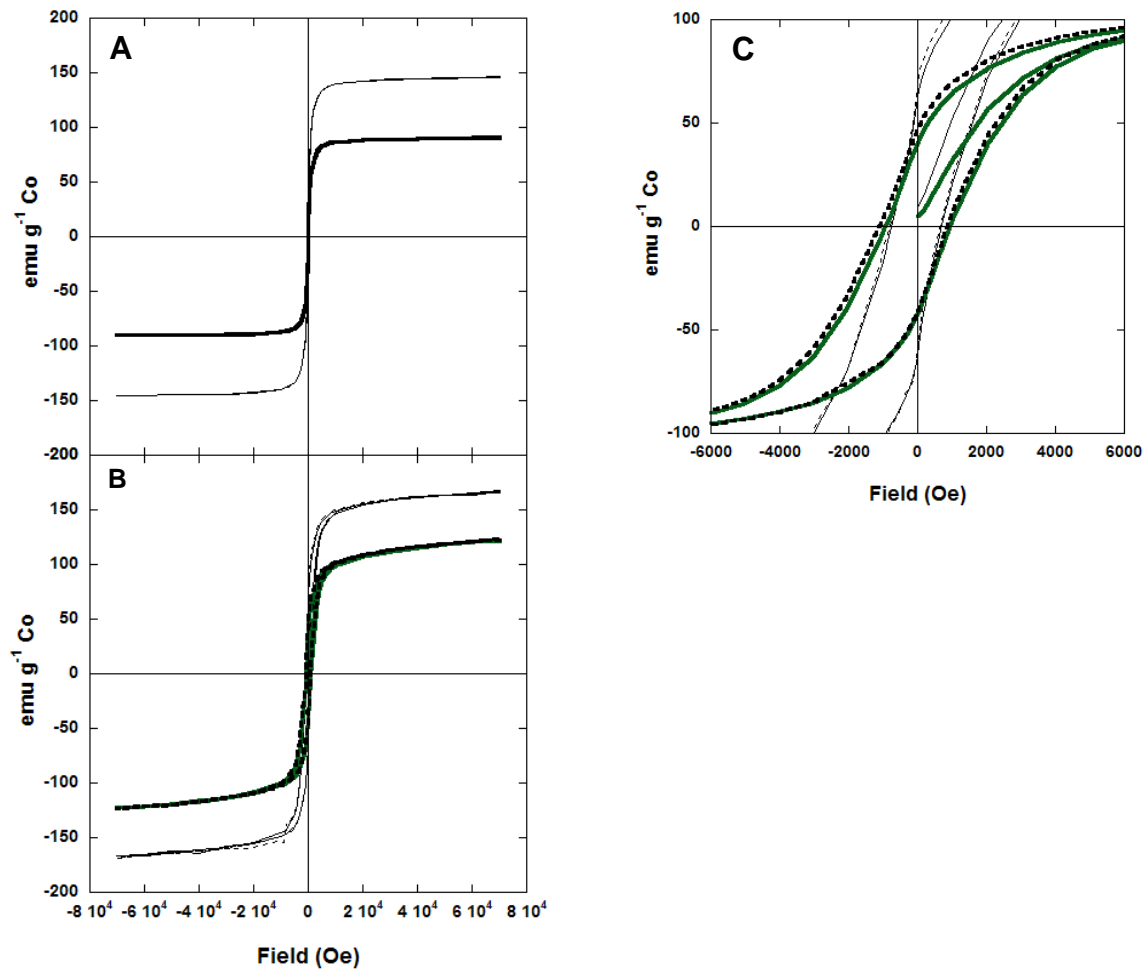


Figure 4.9 σ vs. H measurements conducted on **P2** at A) 300 K (— **P2a**; — **P2b**) and B) 5 K (**P2a**: zero-field cooled hysteresis loop —, field cooled hysteresis loop ---; **P2b**: zero-field cooled hysteresis loop —, field cooled hysteresis loop ---). C) shows enlarged region around the origin for 5K hysteresis loops.

CHAPTER 5. Structural and magnetic properties of anisotropic cobalt ferrite nanoparticles with and without a hydrophilic block copolymer coating

M. A. Zalich,^{a,c} A. Y. Carmichael,^c J. S. Riffle,^c M. Saunders,^b T. G. St. Pierre^a

^aSchool of Physics and ^bCenter for Microscopy and Microanalysis, The University of Western Australia, 35 Stirling Highway, Crawley, WA 6009, Australia

^cDepartment of Chemistry and Macromolecules and Interfaces Institute, Virginia Polytechnic Institute and State University, Blacksburg, VA 24060, USA

5.1 Abstract

Anisotropic ferrite nanoparticles were coated with a triblock copolymer dispersant in an effort to make them dispersible in aqueous media. The magnetic and structural properties of uncoated and coated nanoparticles were compared to determine if there was a difference between the two systems. The samples were structurally similar as they both came from the same starting material and were essentially magnetite with trace amounts of other transition metals. Both the uncoated and coated samples had similar electron and x-ray diffraction patterns; however, the coated sample had additional peaks in the x-ray diffraction pattern. These peaks were attributed to the polymer used to coat the particles and provided evidence for the presence of both the nanoparticles and polymer in the coated sample. Magnetic susceptometry measurements indicated a specific saturation magnetization of 93 emu g^{-1} for the uncoated and 24 emu g^{-1} for the coated sample. This decrease in σ_s for the coated sample also indicates the presence of polymer. Furthermore, the ratio of $\frac{\sigma_R}{\sigma_s}$ for the coated sample is greater, which indicates that the demagnetizing interactions are less than those for the uncoated sample, most likely due to the polymer separating the nanoparticles.

5.2 Introduction

The use of anisotropic particles in biomedicine has been suggested and demonstrated for hyperthermia applications; however, these particles were typically macroscopic with millimeter and even centimeter dimensions.⁹ Particles with dimensions in the nanometer range may have a

better acceptance owing to their comparative ease of insertion into tumor tissues. Furthermore, some preliminary calculations indicate that anisotropic magnetic nanoparticles (nanorods) may have a potential use *in vivo* owing to their increased magnetophoretic mobility over spherical particles when comparing rods with spheres having equal equatorial radii. In the calculations, two assumptions were made: 1) both the rods and spheres are low Reynolds number materials, 2) the rods were considered to be elongated ellipsoids. For a given static magnetic field and medium viscosity, the speed of an object is proportional to its magnetophoretic mobility (ξ). The magnetophoretic mobility is the product of the object volume and the Stokes drag force for that object. Thus, for a sphere, $V_s = \frac{4}{3}\pi r^3$ where r is the radius and for an elongated ellipsoid,

$V_e = \frac{4}{3}\pi a r^2$ where a is the semi-major axis and r is the equatorial radius. The Stokes drag force for a sphere is

$$F_d = 6\pi\mu r v \quad 5.2.1$$

where μ is the dynamic viscosity of the medium and v is the speed of a sphere. The Stokes drag force for an elongated ellipsoid is

$$F_d = \frac{4\pi\mu a v}{\ln\left(\frac{a}{r}\right) + \ln 2 - \frac{1}{2}}. \quad 139 \quad 5.2.2$$

In the case for equal equatorial radii, the ratio of magnetophoretic mobilities is

$$\frac{\xi_{rod}}{\xi_{sphere}} = \frac{3\left[\ln \alpha + \ln 2 - \frac{1}{2}\right]}{2} \quad 5.2.3$$

where the aspect ratio (α) is defined as a/r . In the case for equal volumes, the ratio of magnetophoretic mobilities is

$$\frac{\xi_{rod}}{\xi_{sphere}} = \frac{3\left[\ln \alpha + \ln 2 - \frac{1}{2}\right]}{2\alpha^{\frac{2}{3}}}. \quad 5.2.4$$

Hence, when the rods and spheres have equal equatorial radii, $\frac{\xi_{rod}}{\xi_{sphere}}$ increases with increasing aspect ratio, indicating that rods have a greater magnetophoretic mobility. For the case when

rods and spheres have equal volume, $\frac{\xi_{rod}}{\xi_{sphere}}$ decreases with increasing aspect ratio, indicating that spheres have a greater magnetophoretic mobility. The anisotropic materials under investigation in this research are simple ferrite materials.

Simple ferrite materials are derived from Fe_3O_4 ($\text{FeO}\cdot\text{Fe}_2\text{O}_3$) by replacing the FeO with another divalent transition metal oxide. Simple ferrites are defined by the chemical formula MFe_2O_4 , where M is a divalent transition metal (Mn, Co, Ni, Cu or Zn).³⁷ The ratio of the iron to the other transition metal ion does not need to be 2:1 to see a difference in material properties. Small amounts of transition metals have been used as dopants to alter the properties of pure Fe_3O_4 systems. For example, small percentage of Co in the ferrite structure (e.g. $\text{Co}_{0.04}\text{Fe}_{2.96}\text{O}_4$) is enough to increase the magnetic anisotropy constant (K) to 30 kJ m^{-3} , from -11 kJ m^{-3} for pure Fe_3O_4 , which is useful in magnetic recording media.³⁶ Ngo *et al.* prepared cobalt ferrite nanoparticles with only 3.5 wt% cobalt utilizing Co and Fe dodecylsulfate surfactants to generate $\text{Co}_{0.13}\text{Fe}_{2.58}\text{X}_{0.29}\text{O}_4$ nanoparticles (where X is a cationic vacancy). Nanoparticles with a diameter of $\sim 11 \text{ nm}$ were prepared and it was suggested that the small amount of cobalt in the nanoparticles enhances the magnetocrystalline anisotropy, due to the increased coercivity of the cobalt ‘doped’ system compared with Fe_3O_4 .⁶⁶ Not much research has been conducted on anisotropic ferrite nanoparticles, however, Ji *et al.* reported on the hydrothermal synthesis of CoFe_2O_4 nanorods. A stoichiometric solution of FeCl_3 and CoCl_2 (using cetyltrimethylammonium bromide (CTAB) as a surfactant) was heated at 130°C for 15 hours in an autoclave. The resulting cobalt ferrite nanorods had a mean length of 120 nm and mean diameter of 25 nm.⁶⁸

Herein we report on the structural and magnetic properties of commercially available anisotropic ferrite particles. An attempt was made to coat individual rods, with a triblock copolymer system comprised of poly(ethylene oxide) tail blocks and a carboxylic acid containing urethane central block, to render them dispersible in aqueous media. Structural and magnetic data will be discussed for the uncoated and coated systems. The preliminary data presented in this manuscript will provide the groundwork for future magnetophoretic mobility studies to be conducted on the THALES instrumental setup at the University of Western Australia.

5.3 Experimental

5.3.1 Synthesis of Triblock Copolymer Dispersant.

The synthesis of the triblock copolymer used in this research has been previously reported.³³ Briefly, poly(ethylene oxide) was synthesized by a living anionic polymerization in a high-pressure reactor using potassium *tert*-butoxide as the initiator. The reaction was terminated with acetic acid to afford monofunctional poly(ethylene oxide) (PEO) with the targeted molecular weight of 5,000 g mol⁻¹. Next, the PEO was capped with isophorone diisocyanate and subsequently chain extended with bis(hydroxy methyl)propionic acid in the presence of excess isocyanate. This procedure led to a triblock copolymer comprised of 5,000 g mol⁻¹ PEO end-blocks and a carboxylic acid containing urethane central block, where the average number of carboxylic acids per chain was three.

5.3.2 Preparation of Polymer Coated Nanoparticles.

0.875 g of mixed ferrite nanoparticles (donated by Magnox Inc., Pulaski, Virginia) were added to 40 mL of Milli Q water and agitated with a mechanical stirrer. 3.5 g of the copolymer was dissolved in 10 mL CH₂Cl₂ and subsequently added to the mixed ferrite/water dispersion. The heterogeneous solution was agitated for 16 hours, whereupon the particles were separated by magnetic filtration and rinsed multiple times alternating between water and CH₂Cl₂ to remove excess or unbound polymer. Finally, the material was dried under vacuum for analysis.

5.3.3 Elemental Analysis.

Elemental analyses were performed on the coated and uncoated samples using inductively coupled plasma atomic emission spectroscopy (ICP-AES) at the Marine and Freshwater Research Laboratory at Murdoch University, Perth, Western Australia. The samples were prepared by digestion in a 1:1 mixture of HNO₃:H₂SO₄ for 14 days at 70-100°C. The samples and a blank were diluted and analyzed in triplicate for transition metal concentrations.

5.3.4 Transmission Electron Microscopy.

Transmission electron microscopy (TEM), energy-filtered TEM (EFTEM), electron energy loss spectroscopy (EELS), energy dispersive x-ray spectroscopy (EDX), high-resolution TEM (HRTEM) and selected area electron diffraction (SAD) were conducted with a JEOL

3000F field-emission transmission electron microscope (operated at 300 kV) equipped with a Gatan image filter and digital imaging system. The coated and uncoated samples were dispersed in water by using an ultrasonic bath and subsequently cast onto holey amorphous carbon coated grids for analysis. EFTEM images were acquired at the iron $L_{3,2}$ edge (L_3 edge ~ 707 eV and L_2 edge ~ 720 eV) with a 40 eV slit width and the oxygen K edge (543 eV) with a slit width of 30 eV. Qualitative EELS spectra were collected in image mode with a 4 second acquisition time. Data were collected until a sufficient signal was obtained. Qualitative EDS was conducted with a 50 second acquisition time.

5.3.5 X-ray Powder Diffraction.

A Siemens D-500 x-ray diffractometer (Cu-K α radiation) was used to acquire x-ray diffraction patterns of the 5K-3-5K polymer, the coated sample and the uncoated sample. Powdered samples were placed onto poly(carbonate) sample holders and scanned at a rate of 0.2°/min with a step size of 0.03° from 10-110°.

5.3.6 Magnetic Susceptometry.

A Quantum Design magnetic properties measurement system (MPMS-7) equipped with a superconducting quantum interference device (SQUID)-based sensor was used to make specific magnetization measurements (σ) at varying applied fields (H) from $-70,000$ to $+70,000$ Oe at 300 K and 5K, with 100 Oe spacings between -1000 Oe and 1000 Oe. Low-temperature measurements were conducted both after cooling the sample in zero applied field and in an applied field of 70,000 Oe. The purpose of the different measurements was to study: 1) the saturation magnetization at 300 K, 2) the hysteretic behavior of the sample at 300 K and 3) the magnetic behavior at low temperatures. Henkel plots were generated for the uncoated and coated samples using the method described by Allen *et al.*¹⁴⁰ First, an isothermal remnant magnetization (IRM) curve was measured by applying a constant magnetic field for 700 s, removing the field and measuring the remanent moment 700 s after field removal. This process was conducted up to 20 kOe (in 500 Oe steps), whereupon the procedure was reversed (beginning at -500 Oe) and followed by applying negative fields to -20 kOe to provide the *dc*-demagnetization (DCD) curve. Henkel plots generated from these data were constructed by plotting the normalized IRM remanence vs. DCD remanence magnetizations.

5.4 Results and Discussion

5.4.1 Elemental Analysis

Elemental analysis of the uncoated sample identified transition metals known to be in some mixed ferrite systems (Co, Fe, Mn, Ni, Zn); however, only the Co, Fe and Zn were in significant amounts (2.2, 64 and 1 wt% respectively). Moreover, other trace metals were revealed (Al, Ca, Mg, Na, Ti) albeit below 1 wt%. From the elemental analysis data, the system is referred to as a mixed ferrite system, which is essentially Fe₃O₄ with trace quantities of other transition metals. The coated sample was comprised of 75 wt% polymer and 25 wt% nanoparticles and the elemental analysis values were within 10% of the expected amount calculated from the uncoated sample.

5.4.2 Transmission Electron Microscopy

Transmission electron microscopy (TEM) was used to evaluate the relative size and shape of the anisotropic mixed ferrite nanorods. Figure 5.1 A shows a bright-field image of the uncoated sample, while figure 5.1 B shows a bright-field image of the coated sample. The polymer used in coating the coated sample has a similar electron density to the amorphous carbon film of the TEM grid and is therefore not expected to show significant contrast. The particles range in length from ~200 nm to ~600 nm, with diameters ranging from ~10 to ~50 nm. These values are only approximate, as it is difficult to measure many different particles due to the way that they cluster to minimize their magnetostatic energy. Nevertheless, it is apparent that the nanoparticles under investigation are anisotropic and can be defined as ‘nanorods.’ The aspect ratio for these particles, given the values reported for length and diameter, ranges from approximately 4 to 60.

Energy-filtered TEM (EFTEM), electron energy loss spectroscopy (EELS) and energy dispersive x-ray spectroscopy (EDX) were applied to study the elemental composition and distribution of the nanoparticles. Intense regions of iron and oxygen elemental maps for both the uncoated sample (Figures 5.2 B and 5.2 C) and coated sample (Figures 5.2 E and 5.2 F) correlated well with the electron dense regions of the corresponding bright field images (Figure 5.2 A and 5.2 D respectively). Some EFTEM images of the coated sample showed regions external to the ferrite particles with higher oxygen content than others, which could be due to the polymer used to coat the particles, as it contains oxygen atoms in the PEO block as well as the

acid containing urethane central block. However, the signal intensity is very low and difficult to observe in printed EFTEM images. EELS was used to investigate the presence of other elements detected by elemental analysis and revealed the L-edges of cobalt and nickel in the spectrum, albeit with very weak intensities (Figure 5.3). Elemental maps of Co, Ni or Zn could not be generated due to the low signal of the elements in the sample. EDX also confirmed the presence of other transition metals within the samples (spectra not shown).

High-resolution transmission electron microscopy (HRTEM) was used to probe the crystal structure of the nanorods. Figure 5.4 shows HRTEM images of the uncoated sample (Figure 5.4 A) and coated sample (Figure 5.4 B). The HRTEM image for the uncoated sample shows discrete lattice spacings, which measure ~ 2.92 Å. This spacing is consistent with the 2.97 Å lattice spacing ($\{220\}$ plane) of a ferrite material (inverse spinel). Measurements of the coated sample indicate ~ 2.97 Å for the lattice spacings, also consistent with the $\{220\}$ planes of a ferrite material. Fourier transforms of images 5.4 A and B show the frequency with which the lattice planes in the crystal repeat. Measurements of the repeating frequencies are consistent with the lattice spacings measured from the high-resolution images.

Selected area electron diffraction (SAD) was also employed to study the crystal structure of both the uncoated and coated samples. An exemplary diffraction pattern of the uncoated sample is shown in Figure 5.5 and is similar to the coated sample. Ratios between the diffraction rings are listed in Table 5.1. Rings four and six ($\{222\}$ and $\{331\}$ lattice spacings respectively) are absent, which is expected due to their weak intensities. These data indicate that the ratios of the rings match the ratios of literature d-spacings for magnetite very well, supporting the information obtained from HRTEM analysis.

5.4.3 X-ray Powder Diffraction

X-ray powder diffraction analysis of the uncoated sample revealed reflections at 2θ values that corresponded well with the inverse spinel crystal structure of cobalt ferrite and magnetite (Figure 5.6A, Table 5.2). Cobalt ferrite ($\text{CoO}\cdot\text{Fe}_2\text{O}_3$) has the same crystal structure as magnetite ($\text{FeO}\cdot\text{Fe}_2\text{O}_3$), with the only difference being the divalent ion in the system (Co^{+2} for cobalt ferrite and Fe^{+2} for magnetite). The intensity of x-ray reflections can change owing to the different structure factors for different elements. The x-ray diffraction intensities for the uncoated and coated samples had a better match to magnetite. The diffraction pattern for the

coated sample was identical to the uncoated sample, but contained other reflections at smaller values of 2θ (Figure 5.6B). XRD analysis of the powdered polymer sample revealed intense peaks at 2θ values of 19 and 23.2° and a broad doublet between 25.5 and 27.5° (Figure 5.6C). Poly(ethylene oxide) is a semi-crystalline polymer and these reflections have been reported elsewhere for PEO or PEO based polymer coated nanocomposites.¹⁴¹⁻¹⁴³ The reflections at small values of 2θ for the coated sample matched with the reflections of the polymer, indicating that the coated sample is comprised of polymer and inverse spinel mixed ferrite particles (Table 5.2).

5.4.4 Magnetic Susceptometry

Room temperature specific magnetization (σ) versus applied magnetic field (H) hysteresis loop measurements of the uncoated sample (Figure 5.7) indicated a saturation magnetization value (σ_S) of 93 emu g⁻¹ sample, a remanent specific magnetization value (σ_R) of ~36 emu g⁻¹ sample and a coercivity (H_C) of 650 Oe. Since the uncoated sample is known to be magnetite with trace amounts of Co and Zn, the saturation value compares well with that of pure magnetite (Fe₃O₄) having a literature σ_S of 90 emu g⁻¹ at room temperature.¹²⁹ The magnetic properties displayed by the uncoated sample are similar to those of a magnetically blocked material, owing to the degree of magnetic remanence and coercivity. Magnetization versus temperature measurements indicated a maximum blocking temperature around 300 K. Low temperature (5 K) σ vs. H measurements showed an increase in H_C to ~2000 Oe and σ_R to ~55 emu g⁻¹.

Room temperature σ vs. H measurements on the coated sample (Figure 5.7) revealed a σ_S of 24 emu g⁻¹ sample, σ_R of 10 emu g⁻¹ sample and H_C ~ 610 Oe. The saturation and remanent magnetization values are about 25% of the values reported for the uncoated sample, which is expected as the coated sample contains ~25 wt% mixed ferrite nanoparticles. H_C is independent of the mass fraction of ferrite in the sample and is similar to that reported for the uncoated sample. σ vs. T measurements also indicated a maximum blocking temperature around 300 K. 5 K σ vs. H measurements showed a similar behavior to the uncoated sample, with increased coercivity and σ_R .

Henkel plots were generated for both the uncoated and coated samples to investigate the presence of interparticle interactions. It was postulated that the coated sample would show

weaker interparticle interactions if each particle were individually coated with the block copolymer dispersant. Both Henkel plots indicated a demagnetizing interaction in the samples of the same order of magnitude. These results suggest that either the particles in the coated sample are not individually coated and are interacting, or the coating on individual particles does not provide sufficient distance from neighboring particles to decrease or eliminate interparticle interactions. Note, however, that $\frac{\sigma_R}{\sigma_S}$ for the coated particles is 0.42, while $\frac{\sigma_R}{\sigma_S}$ for the uncoated particles is 0.39. This difference suggests that the demagnetizing interactions for the coated sample are weaker than the demagnetizing interactions for the uncoated sample, most likely owing to the polymer separating the coated particles. Thus, the assumption of having ideal Stoner-Wohlfarth particles (single domain particles with coherent rotation of spins) used for constructing Henkel plots, may not apply to this system, since the particles are of the size where domain walls could be present.

5.5 Conclusions

The mixed ferrite nanoparticles were determined to be comprised primarily of magnetite with other transition metals as dopants (Co, Ni, Zn). Energy-filtered TEM, electron energy loss spectroscopy and energy dispersive x-ray spectroscopy confirmed that the dominant elements present in the sample are iron and oxygen. The length of the nanoparticles ranged from 200 to 600 nm and the width ranged from 10 to 50 nm, indicating that the particles are anisotropic in shape (nanorods). High-resolution TEM, selected area electron diffraction and x-ray diffraction indicated that the particles had an inverse spinel crystal structure, similar to magnetite. Magnetic susceptibility measurements indicated that the uncoated sample had a saturation magnetization (92 emu g^{-1}) similar to bulk magnetite (90 emu g^{-1}), while the saturation magnetization of the coated sample was proportional to the amount of mixed ferrite material charged during the stabilization procedure. The demagnetizing interactions were greater in the uncoated sample, suggesting that the polymer coating in the coated sample may be decreasing the interparticle interactions.

Future research will be conducted to individually coat the particles with block copolymer dispersants. Experiments will be performed to evaluate their magnetophoretic mobility using THALES, an instrument constructed at the University of Western Australia for measuring

magnetophoretic mobilities. Ultimately, individually coated particles will be studied *in vivo* for potential biomedical applications.

5.6 Acknowledgements

The authors of this paper acknowledge the support of NSF under contract DMR-0312046, DARPA-AFOSR (contracts #F49620-02-1-0408 and F49620-03-1-0332), OMNOVA Solutions and the Australian Research Council (grant # DP0559333) for funding. M. A. Zalich thanks the Australian-American Fulbright Commission for a Fulbright Postgraduate Fellowship to conduct research in Australia.

Table 5.1 Ratios of experimental electron diffraction rings compared to literature values for magnetite ²

Ring Ratios	Ratios for Uncoated	Ratios for Coated	Literature Ratios
1/2	1.63	1.63	1.63
2/3	1.18	1.17	1.17
3/5	1.20	1.20	1.21
5/7	1.23	1.22	1.23
7/8	1.07	1.07	1.06
8/9	1.08	1.09	1.09

Table 5.2 Peak comparisons for experimental uncoated and coated samples with literature values for magnetite and pure polymer

Peak #	Exp. d-spacing uncoated	Exp. d-spacing coated	Lit. d-spacing Fe ₃ O ₄ ²	Exp. d-spacing polymer
1	4.86	4.82	4.85	
2	2.97	2.97	2.97	
3	2.53	2.53	2.53	
4	2.43	2.42	2.42	
5	2.1	2.1	2.1	
6	1.93	1.92	1.93	
7	1.72	1.71	1.71	
8	1.62	1.61	1.62	
9	1.48	1.48	1.48	
10	1.42	1.42	1.42	
11	1.33	1.33	1.33	
12	1.28	1.28	1.28	
13	1.27	1.26	1.27	
14	1.21	1.21	1.21	
15	1.17	1.17	1.18	
15	1.12	1.12	1.12	
17	1.09	1.09	1.09	
18	1.05	1.05	1.05	
A		4.63		4.66
B		3.81		3.83
C		3.4		3.41
D		3.3		3.32

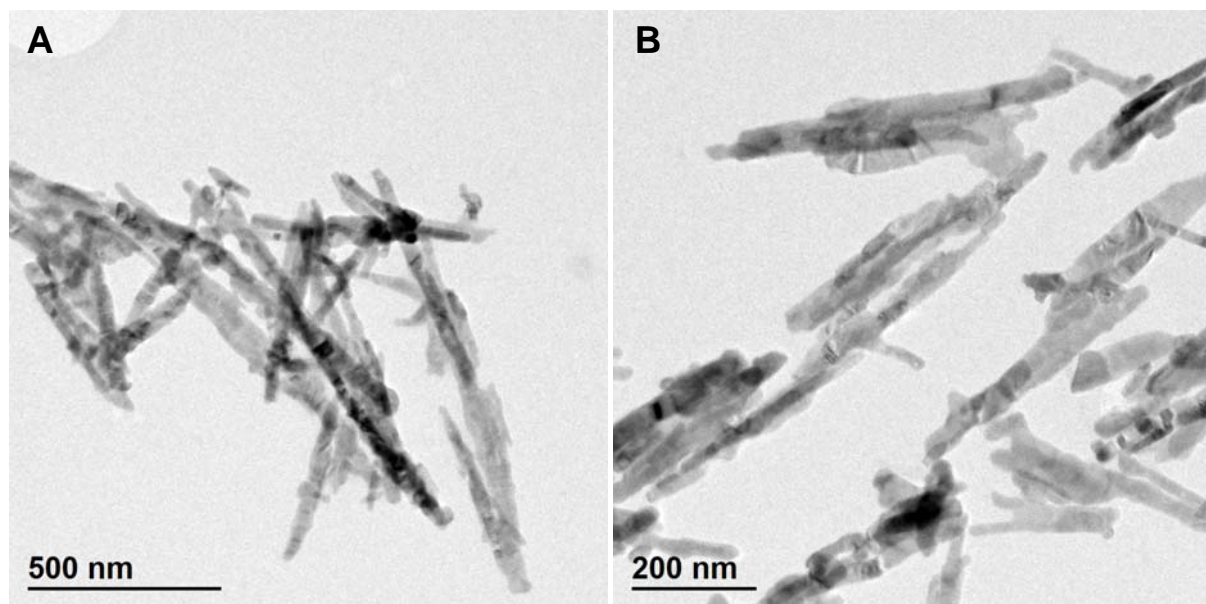


Figure 5.1 TEM images of: A) uncoated nanoparticles and B) coated nanoparticles.

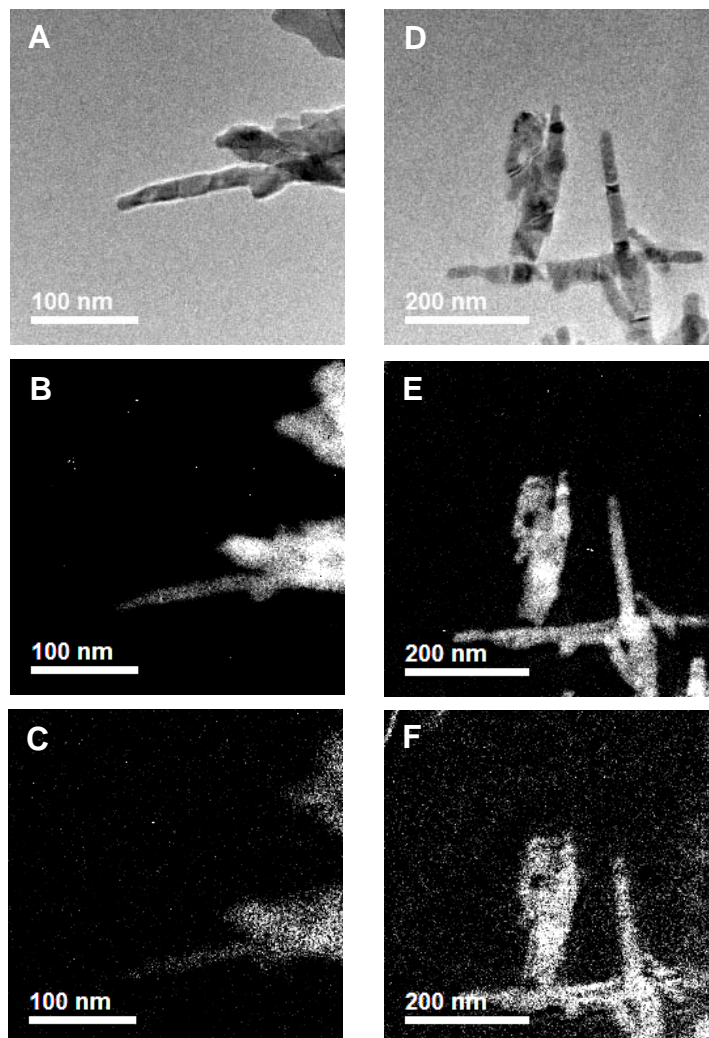


Figure 5.2 A) bright field image of uncoated sample, B) corresponding iron elemental map of A, C) corresponding oxygen elemental map of A, D) bright field image of coated sample, E) corresponding iron elemental map of D and F) corresponding oxygen elemental map of D.

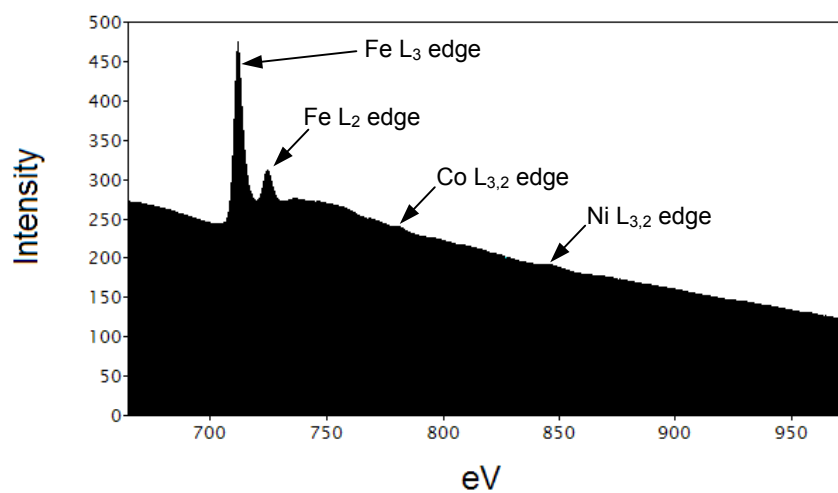


Figure 5.3 EELS spectrum from uncoated sample with edges labeled..

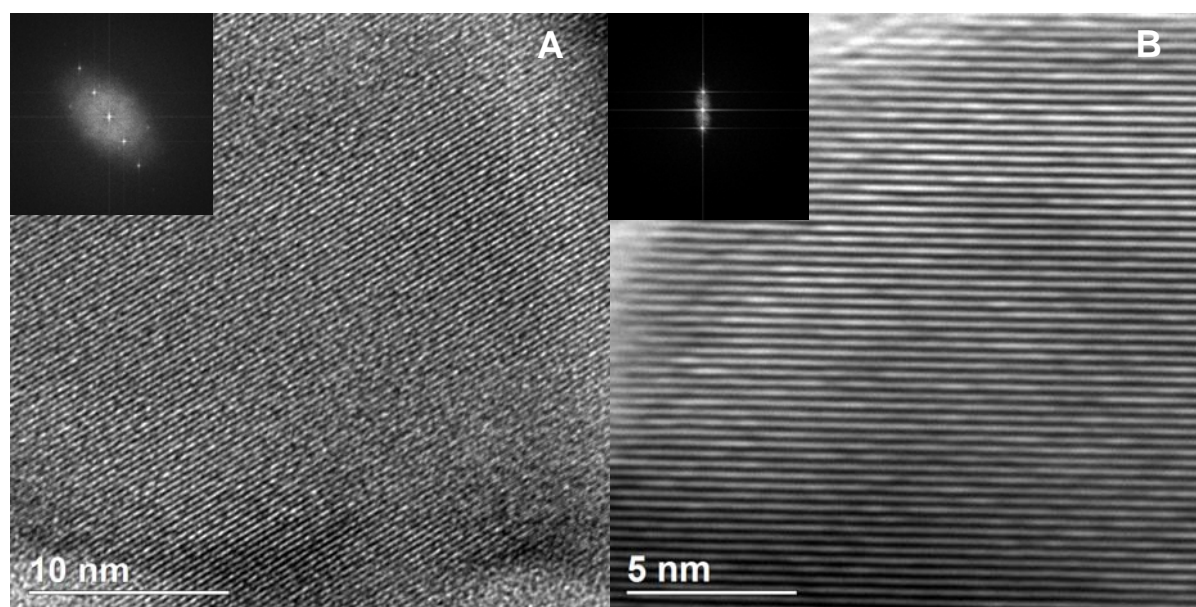


Figure 5.4 High-resolution transmission electron micrographs of: A) uncoated sample and B) coated sample. Insets are Fourier transforms of respective images.

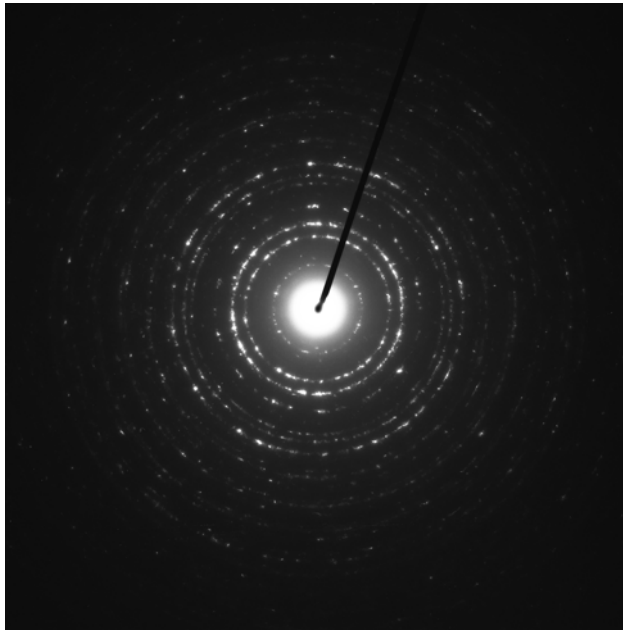


Figure 5.5 Exemplary selected area diffraction pattern for uncoated sample.

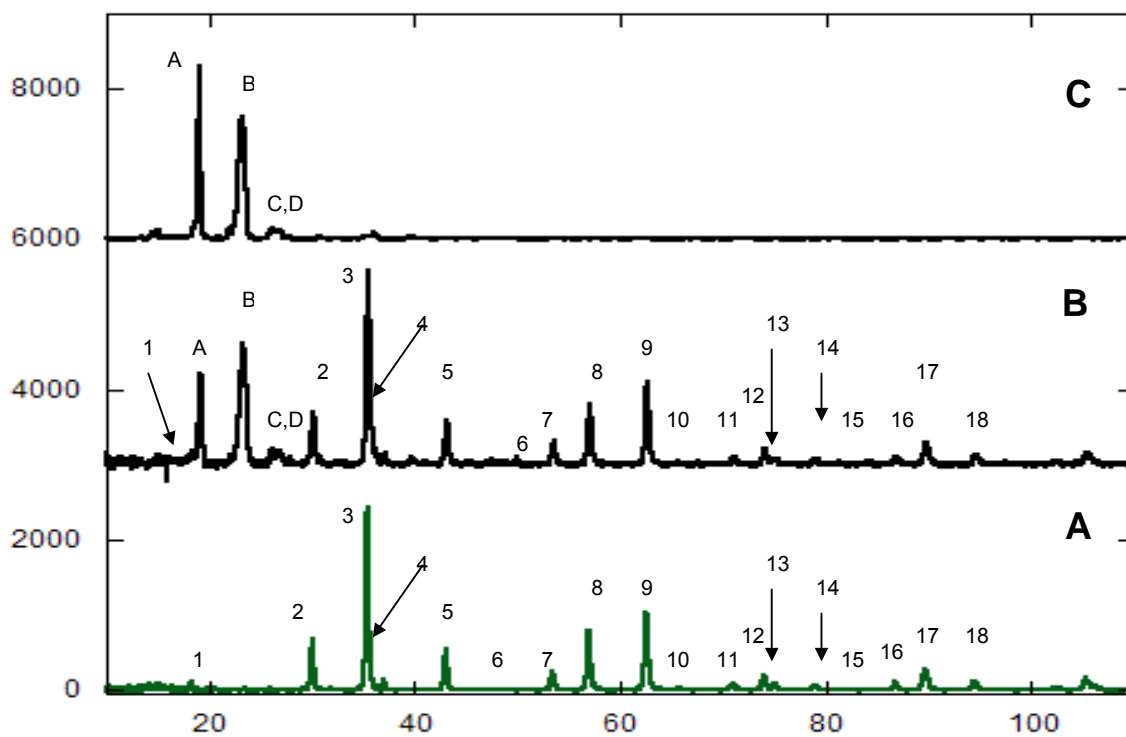


Figure 5.6 X-ray diffraction patterns for: A) uncoated sample, B) coated sample and C) pure polymer

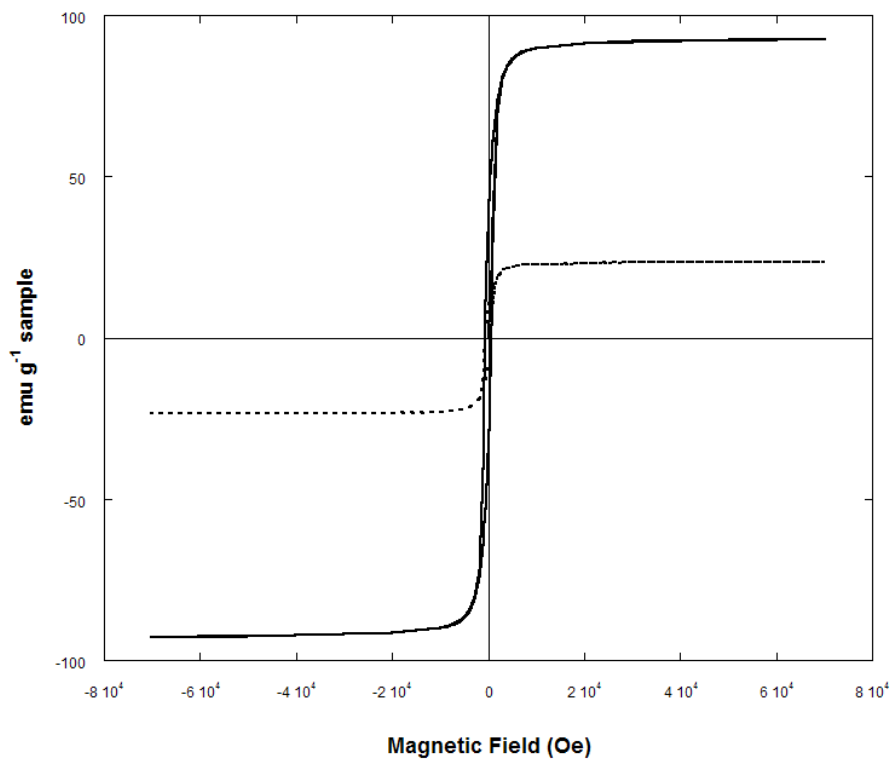


Figure 5.7 Room temperature σ vs. H curves for uncoated (—) and coated (---) samples.

CHAPTER 6. Conclusions

The thermal decomposition of dicobalt octacarbonyl in the presence of poly(styrene-*b*-4-vinylphenoxyphthanolonitile) afforded discrete cobalt nanoparticles with a mean particle size of 18.5 nm. Upon thermal treatment, the polymer coating pyrolyzed to generate a graphitic coating around the cobalt nanoparticles. In addition, thermal treatment led to nanoparticle sintering and an increase in mean particle size (36.1 nm) and size distribution breadth. X-ray diffraction (XRD) confirmed that the dominant crystal phase of the cobalt in the pre-heat-treated and heat-treated samples was fcc; however, high-resolution transmission electron microscopy (HRTEM) provided evidence that at least some hcp cobalt was present in the heat-treated sample. Magnetic susceptibility measurements indicated that the pre-heat-treated sample oxidized upon exposure to air as evidenced by a noticeable asymmetric field-cooled hysteresis loop shift, while the heat-treated sample was oxidatively stable for over one year owing to the graphitic sheaths around the cobalt nanoparticles.

Thermally decomposing dicobalt octacarbonyl in the presence of poly(dimethylsiloxane-*b*-(methylvinylsiloxane-*co*-methyl(2-trimethoxysilyl)ethyl)siloxane)) led to cobalt nanoparticles with a mean particle size of 14.1 nm. Thermal treatment of this system at 600°C generated two distinct populations of particles (modes at ~10 and 120 nm) with a mean particle size of 91 nm. This bimodal distribution was attributed to some cobalt nanoparticle sintering at 600°C. Thermal treatment at 700°C led to cobalt nanoparticles with a mean particle size of 10.1 nm. It is hypothesized that thermal treatment at 700°C pyrolyzes the polymer coating faster than thermal treatment at 600°C, which effectively locks the cobalt nanoparticles in a silica-type matrix preventing them from coming into contact with one another and sintering. XRD confirmed that the dominant crystal phase of the thermally treated samples was fcc cobalt; however, the presence of hcp cobalt was demonstrated by HRTEM analysis. The pre-heat-treated sample was weakly crystalline as evidenced by the weak diffraction peaks in x-ray diffraction pattern. Magnetic susceptibility measurements indicated that thermal treatment caused an increase in the cobalt specific saturation magnetization, most likely owing to the pyrolysis of the polymer coating and an increase in cobalt nanoparticle crystallinity. The pre-heat-treated sample seemed to be more susceptible to oxidation, probably owing to the weak crystallinity and lack of oxidative protection. The heat-treated samples oxidized more slowly, possibly owing to their increased crystallinity and silica coating.

The mixed ferrite nanoparticles were determined to be comprised primarily of magnetite with other transition metals as dopants (Co, Ni, Zn). Energy-filtered TEM, electron energy loss spectroscopy and energy dispersive x-ray spectroscopy confirmed that the dominant elements present in the sample are iron and oxygen. The length of the nanoparticles ranged from 200 to 600 nm and the width ranged from 10 to 50 nm, indicating that the particles are anisotropic in shape (nanorods). HRTEM, selected area electron diffraction and XRD indicated that the particles had an inverse spinel crystal structure, similar to magnetite. Magnetic susceptibility measurements indicated that the uncoated sample had a saturation magnetization (92 emu g^{-1}) similar to bulk magnetite (90 emu g^{-1}), while the saturation magnetization of the coated sample was proportional to the amount of mixed ferrite material charged during the stabilization procedure. The ratio of $\frac{\sigma_R}{\sigma_S}$ for the coated sample was greater than the ratio of $\frac{\sigma_R}{\sigma_S}$ for the uncoated sample, which implies that the demagnetizing interactions between the particles are greater in the uncoated sample. This information suggests that the polymer coating is separating the nanoparticles and preventing them from interacting to a certain extent.

CHAPTER 7. Recommendations for Future Work

It would be advantageous to learn more about the thermal treatment of cobalt nanoparticles stabilized by the polymeric dispersant systems described in Chapters 3 and 4. A designed experiment with time and temperature as variables may provide information on the degree of particle sintering and particle crystallinity, so that the thermal treatment procedure can be tailored to generate discrete and highly-crystalline cobalt nanoparticles for each block copolymer system. From a synthetic front, block copolymers comprised of a 4-vinylphenoxyphthalonitrile anchor block and siloxane-containing stabilizing block would be interesting candidates for dispersing nanoparticles. The 4-vinylphenoxyphthalonitrile block interacts strongly with cobalt nanoparticle surfaces and shows evidence for forming an oxidatively stable graphitic coating around the cobalt nanoparticles after thermal treatment. PDMS and other siloxane-based polymers sterically stabilize cobalt nanoparticles in a variety of solvents and the pyrolysis of a siloxane polymer leads to silica. Silica is highly functional and can be decorated with numerous functional groups. Different polymers can be grown from the functional groups leading to oxidatively stable nanoparticles with steric stabilizers tailored for desired solvents.

Anisotropic ferrite nanoparticles need to be coated individually to realize their potential in biomedical applications. One problem with these particles is that they have remanent magnetization, which leads to interparticle interactions and clustering. It is unclear as to whether mechanical stirring separates the particles enough to individually coat them. More than likely, clusters of particles were coated in Chapter 5. One way to remove the remanent magnetization is by heating the particles above the blocking temperature; however, this may lead to a change in the particle structure and/or size. Another possibility is to mechanically agitate a solution of the particles in an ultrasonic bath and then add the polymeric dispersant. This dual-agitation procedure may lead to particles that are less aggregated and may afford individually coated ferrite nanorods. Once individually coated nanorods are prepared, their magnetophoretic mobility can be studied using an instrument (THALES) in the School of Physics at the University of Western Australia, specifically designed for studying the behavior of magnetic particulate media in fluids.

Analytically, it would be interesting to study any magnetic nanoparticle system using off-axis electron holography. In electron holography, one can study the magnetic behavior of

individual magnetic nanoparticles *in situ*. The specimen is oriented such that the incident electron beam in half of the column interacts with the specimen (object beam) and the electron beam on the other half of the column does not interact with anything (reference beam). Electron holography is conducted in a TEM equipped with an electronic biprism (small conductive filament) located in an image lens. The filament is normal to the electron beam and when a voltage is applied to the filament the electrons on either side of the filament (object and reference beams) are bent towards the center causing them to overlap and interfere. The resulting hologram contains information relating to the magnetic field and magnetic flux density of a sample.¹⁴⁴ Dunin-Borkowski *et al.* have used electron holography to study the magnetic behavior of cobalt nanoparticles undergoing *in situ* hysteresis loops. The strength of the objective lens in the microscope was changed to change the magnetic field and holograms for each field strength were recorded to learn about remanent states at varying applied field strengths.¹⁴⁵

References

1. F. C. C. Cobalt, in *JCPDS-International Centre for Diffraction Data*, card 15-0806, **1996**.
2. Magnetite, in *JCPDS-International Centre for Diffraction Data*, card 75-33, **1996**.
3. I. Safarik, M. Safarikova, "Magnetic Nanoparticles and Biosciences," *Monatshefte für Chemie*, *133*, 737-759 (2002).
4. I. Penninga, H. deWaard, B. M. Moskowitz, D. A. Bazylinski, R. B. Frankel, "Remanence measurements on individual magnetotactic bacteria using a pulsed magnetic field," *J. Magn. Magn. Mater.*, *149*, 279-286 (1995).
5. C. E. Diebel, R. Proksch, C. R. Green, P. Neilson, M. M. Walker, "Magnetite defines a vertebrate magnetoreceptor," *Nature*, *406*, 299-302 (2000).
6. C. V. Mora, M. Davison, J. M. Wild, M. M. Walker, "Magnetoreception and its trigeminal mediation in the homing pigeon," *Nature*, *432*, 508-511 (2004).
7. P. P. Grassi-Schultheiss, F. Heller, J. Dobson, "Analysis of magnetic material in the human heart, spleen and liver," *BioMetals*, *10*, 351-355 (1997).
8. P. P. Schultheiss-Grassi, J. Dobson, "Magnetic analysis of human brain tissue," *BioMetals*, *12*, 67-72 (1999).
9. S. Mornet, S. Vasseur, F. Grasset, E. Duguet, "Magnetic nanoparticle design for medical diagnosis and therapy," *J. Mater. Chem.*, *14*, 2161-2175 (2004).
10. A. Jordan, R. Scholz, P. Wust, H. Faehling, R. Felix, "Magnetic fluid hyperthermia (MFH): Cancer treatment with AC magnetic field induced excitation of biocompatible superparamagnetic nanoparticles," *J. Magn. Magn. Mater.*, *201*, 413-419 (1999).
11. A. Jordan, R. Scholz, K. Maier-Hauff, M. Johannsen, P. Wust, J. Nadobny, H. Schirra, H. Schmidt, S. Deger, S. Loening, W. Lanksch, R. Felix, "Presentation of new magnetic field therapy system for the treatment of human solid tumors with magnetic fluid hyperthermia," *J. Magn. Magn. Mater.*, *225*, 118-126 (2001).
12. J. P. Dailey, J. P. Phillips, C. Li, J. S. Riffle, "Synthesis of silicone magnetic fluid for use in eye surgery," *J. Magn. Magn. Mater.*, *194*, 140-148 (1999).
13. Q. A. Pankhurst, J. Connolly, S. K. Jones, J. Dobson, "Applications of magnetic nanoparticles in biomedicine," *J. Phys. D: Appl. Phys.*, *36*, R167-R181 (2003).
14. P. Tartaj, M. del-Puerto-Morales, S. Veintemillas-Verdaguer, T. Gonzalez-Carreno, C. J. Serna, "The preparation of magnetic nanoparticles for applications in biomedicine," *J. Phys. D: Appl. Phys.*, *36*, R182-R197 (2003).
15. X. Su, H. Zheng, Z. Yang, Y. Zhu, A. Pan, "Preparation of nanosized particles of FeNi and FeCo alloy in solution," *J. Mater. Chem.*, *38*, 4581-4585 (2003).
16. S. Sun, C. B. Murray, D. Weller, L. Folks, A. Moser, "Monodisperse FePt nanoparticles and ferromagnetic FePt nanocrystal superlattices," *Science*, *287*, 1989-1992 (2000).
17. Y. Huang, Y. Zhang, G. C. Hadjipanayis, A. Simopoulos, D. Weller, "Hysteresis Behavior of CoPt Nanoparticles," *IEEE Trans. Mag.*, *38*, 2604-2606 (2002).
18. D. Mercier, J.-C. S. Levy, G. Viau, F. Fievet-Vincent, F. Fievet, P. Toneguzzo, O. Acher, "Magnetic resonance in spherical Co-Ni and Fe-Co-Ni particles," *Phys. Rev. B*, *62*, 532-544 (2000).
19. P. Toneguzzo, G. Viau, O. Acher, F. Guillet, E. Bruneton, F. Fievet-Vincent, F. Fievet, "CoNi and FeCoNi fine particles prepared by the polyol process: Physico-chemical characterization and dynamic magnetic properties," *J. Mater. Sci.*, *35*, 3767-3784 (2000).

20. D. J. Shaw, *Introduction to Colloid and Surface Chemistry*, 4th ed., Butterworth-Heinemann Ltd., Boston, **1992**.
21. B. Jirgensons, M. E. Straumanis, *A Short Textbook of Colloid Chemistry*, Pergamon Press Limited, London, **1954**.
22. S. R. Hoon, B. K. Tanner, "Magnetic Fluids-Part 1," *Phys. Educ.*, *20*, 61-65 (1985).
23. R. E. Rosensweig, "Magnetic Fluids," *Sci. Amer.*, *247*, 124-132 (1982).
24. D. H. Napper, *Polymeric Stabilization of Colloidal Dispersions*, Academic Press, New York, **1983**.
25. R. Tadmor, R. E. Rosensweig, J. Frey, J. Klein, "Resolving the Puzzle of Ferrofluid Dispersants," *Langmuir*, *16*, 9117-9120 (2000).
26. R. W. Chantrell, A. Bradbury, J. Popplewell, S. W. Charles, "Agglomerate formation in a magnetic fluid," *J. Appl. Phys.*, *53*, 2742-2744 (1982).
27. J. J. M. Janssen, J. J. M. Baltussen, A. P. v. Gelder, J. A. A. J. Perenboom, "Kinetics of magnetic flocculation. I: Flocculation of colloidal particles," *J. Phys. D: Appl. Phys.*, *23*, 1447-1454 (1990).
28. J. Svoboda, "Magnetic Flocculation and Treatment of Fine Weakly Magnetic Minerals," *IEEE Trans. Mag.*, *18*, 796-801 (1982).
29. R. Massart, "Preparation of Aqueous Magnetic Liquids in Alkaline and Acidic Media," *IEEE Trans. Mag.*, *17*, 1247-1248 (1981).
30. D. F. Evans, H. Wennerstrom, *The Colloidal Domain*, 2nd ed., Wiley-VCH, New York, **1999**.
31. J. Israelachvili, *Intermolecular and Surface Forces*, 2nd ed., Academic Press, New York, **2002**.
32. R. M. Cornell, U. Schwertmann, *The Iron Oxides: Structure, Properties, Reactions, Occurrences and Uses*, 2nd ed., Wiley-VCH GmbH & Co. KGaA, Weinheim, **2003**.
33. L. A. Harris, J. D. Goff, A. Y. Carmichael, J. S. Riffle, J. J. Harburn, T. G. St.Pierre, M. Saunders, "Magnetite Nanoparticle Dispersions Stabilized with Triblock Copolymers," *Chem. Mater.*, *15*, 1367-1377 (2003).
34. J. R. Thomas, "Preparation and Magnetic Properties of Colloidal Cobalt Particles," *J. Appl. Phys.*, *37*, 2914-2915 (1966).
35. J. P. Wilcoxon, P. P. Provencio, "Use of Surfactant Micelles to Control the Structural Phase of Nanosize Iron Clusters," *J. Phys. Chem. B*, *103*, 9809-9812 (1999).
36. D. Craik, *Magnetism: Principles and Applications*, John Wiley & Sons, Inc., New York, **1995**.
37. J. P. Jakubovics, *Magnetism and Magnetic Materials*, 2nd ed., The Institute of Materials, Cambridge, **1994**.
38. G. D. Mendenhall, Y. Geng, J. Hwang, "Optimization of Long-Term Stability of Magnetic Fluids from Magnetite and Synthetic Polyelectrolytes," *J. Colloid Interface Sci.*, *184*, 519-526 (1996).
39. J. Lee, T. Isobe, M. Senna, "Preparation of Ultrafine Fe₃O₄ Particles by Precipitation in the Presence of PVA at High pH," *J. Colloid Interface Sci.*, *177*, 490-494 (1996).
40. K. M. Lee, C. M. Sorensen, K. J. Klabunde, G. C. Hadjipanayis, "Synthesis and Characterization of Stable Colloidal Fe₃O₄ Particles in Water-in-Oil Microemulsions," *IEEE Trans. Mag.*, *28*, 3180-3182 (1992).
41. K. Wormuth, "Superparamagnetic Latex via Inverse Emulsion Polymerization," *J. Colloid Interface Sci.*, *241*, 366-377 (2001).

42. J. A. Lopez-Perez, M. A. L. Quintela, J. Mira, J. Rivas, S. W. Charles, "Advances in the Preparation of Magnetic Nanoparticles by the Microemulsion Method," *J. Phys. Chem. B*, *101*, 8045-8047 (1997).
43. T. Hyeon, S. S. Lee, J. Park, Y. Chung, H. B. Na, "Synthesis of Highly Crystalline and Monodisperse Maghemite Nanocrystallites without a Size-Selection Process," *J. Am. Chem. Soc.*, *123*, 12798-12801 (2001).
44. X. Teng, H. Yang, "Effects of surfactants and synthetic conditions on the sizes and self-assembly of monodisperse iron oxide nanoparticles," *J. Mater. Chem.*, *14*, 774-779 (2004).
45. L. E. Euliss, S. G. Grancharov, S. O'Brien, T. J. Deming, G. D. Stucky, C. B. Murray, G. A. Held, "Cooperative Assembly of Magnetic Nanoparticles and Block Copolypeptides in Aqueous Media," *Nanoletters*, *3*, 1489-1493 (2003).
46. R. S. Underhill, G. Liu, "Triblock Nanospheres and Their Use as Templates for Inorganic Nanoparticle Preparation," *Chem. Mater.*, *12*, 2082-2091 (2000).
47. D. P. Dinenga, M. G. Bawendi, "A Solution-Phase Chemical Approach to a New Crystal Structure of Cobalt," *Angew. Chem. Int. Ed.*, *38*, 1788-1791 (1999).
48. V. F. Puentes, K. M. Krishnan, A. P. Alivisatos, "Colloidal Nanocrystal Shape and Size Control: The Case of Cobalt," *Science*, *291*, 2115-2117 (2001).
49. X. Nie, J. C. Jiang, E. I. Meletis, L. D. Tung, L. Spinu, "Synthesis, structure and magnetic properties of ϵ -Co nanocrystalline thin films and annealing affects," *J. Appl. Phys.*, *93*, 4750-4755 (2003).
50. S. Sun, C. B. Murray, "Synthesis of monodisperse cobalt nanocrystals and their assembly into magnetic superlattices (invited)," *J. Appl. Phys.*, *85*, 4325-4330 (1999).
51. C. B. Murray, S. Sun, W. Gaschler, H. Doyle, T. A. Betley, C. R. Kagan, "Colloidal synthesis of nanocrystals and nanocrystal superlattices," *IBM J. Res. & Dev.*, *45*, 47-55 (2001).
52. A. Huettner, D. Sudfeld, I. Ennen, G. Reiss, W. Hachmann, U. Heinzmann, K. Wojczykowski, P. Jutzi, W. Saikaly, G. Thomas, "New magnetic nanoparticles for biotechnology," *J. Biotechnology*, *112*, 47-63 (2004).
53. I. Lisiecki, P.-A. Albouy, M. P. Pileni, "Face-Centered Cubic "Supracrystals" of Cobalt Nanocrystals," *Adv. Mater.*, *15*, 712-716 (2003).
54. C. Petit, A. Taleb, M. P. Pileni, "Cobalt Nanosized Particles Organized in a 2D Superlattice: Synthesis, Characterization and Magnetic Properties," *J. Phys. Chem. B*, *103*, 1805-1810 (1999).
55. C. Petit, M. P. Pileni, "Physical properties of self-assembled nanosized cobalt particles," *Appl. Surf. Sci.*, *162-163*, 519-528 (2000).
56. J.-I. Park, N.-J. Kang, Y.-W. Jun, S. J. Oh, H.-C. Ri, J. Cheon, "Superlattice and Magnetism Directed by the Size and Shape of Nanocrystals," *Chem. Phys. Chem.*, *6*, 543-547 (2002).
57. J. P. Chen, C. M. Sorensen, K. J. Klabunde, G. C. Hadjipanayis, "Enhanced magnetization of nanoscale colloidal cobalt particles," *Phys. Rev. B*, *51*, 11 527-511 532 (1995).
58. J. Osuna, D. deCaro, C. Amiens, B. Chaudret, E. Snoeck, M. Respaud, J.-M. Broto, A. Fert, "Synthesis, characterization and magnetic properties of cobalt nanoparticles from an organometallic precursor," *J. Phys. Chem.*, *100*, 14571-14574 (1996).
59. M. Respaud, J. M. Broto, H. Rakoto, A. R. Fert, L. Thomas, B. Barbara, M. Verelst, E. Snoeck, P. Lecante, A. Mosset, J. Osuna, T. O. Ely, C. Amiens, B. Chaudret, "Surface

- effects on the magnetic properties of ultrafine cobalt particles," *Phys. Rev. B*, *57*, 2925-2935 (1998).
60. E. H. Tadd, J. Bradley, R. Tannenbaum, "Spatial distribution of Cobalt nanoclusters in block copolymers," *Langmuir*, *18*, 2378-2384 (2002).
 61. J. P. Stevenson, M. Rutnakornpituk, M. Vadala, A. R. Esker, S. W. Charles, S. Wells, J. P. Dailey, J. S. Riffle, "Magnetic cobalt dispersions in poly(dimethylsiloxane) fluids," *J. Magn. Magn. Mater.*, *225*, 47-58 (2001).
 62. M. Rutnakornpituk, M. S. Thompson, L. A. Harris, K. E. Farmer, A. R. Esker, J. S. Riffle, J. Connolly, T. G. St.Pierre, "Formation of cobalt nanoparticle dispersions in the presence of polysiloxane block copolymers," *Polymer*, *43*, 2337-2348 (2002).
 63. J. Connolly, T. G. St.Pierre, M. Rutnakornpituk, J. S. Riffle, "Cobalt nanoparticles formed in polysiloxane copolymer micelles: effect of production methods on magnetic properties," *J. Phys. D: Appl. Phys.*, *37*, 2475-2482 (2004).
 64. Q. Song, Z. J. Zhang, "Shape Control and Associated Magnetic Properties of Spinel Cobalt Ferrite Nanocrystals," *J. Am. Chem. Soc.*, *126*, 6164-6168 (2004).
 65. N. Moumen, M. P. Pileni, "New Synthesis of Cobalt Ferrite Particles in the Range 2-5 nm: Comparison of the Magnetic Properties of the Nanosized Particles in Dispersed Fluid or in Powder Form," *Chem. Mater.*, *8*, 1128-1134 (1996).
 66. A.-T. Ngo, M. P. Pileni, "Nanoparticles of Cobalt Ferrite: Influence of the Applied Field on the Organization of the Nanocrystals on a Substrate and on Their Magnetic Properties," *Adv. Mater.*, *12*, 276-279 (2000).
 67. M. Bonini, A. Wiedenmann, P. Baglioni, "Synthesis and characterization of surfactant and silica-coated cobalt ferrite nanoparticles," *Physica A*, *339*, 86-91 (2004).
 68. G. B. Ji, S. L. Tang, S. K. Ren, F. M. Zhang, B. X. Gu, Y. W. Du, "Simplified synthesis of single-crystalline magnetic CoFe_2O_4 nanorods by a surfactant-assisted hydrothermal process," *J. Cryst. Growth*, *270*, 156-161 (2004).
 69. D. Halliday, R. Resnick, J. Walker, *Fundamentals of Physics: Extended*, 5th ed., John Wiley & Sons, Inc., New York, **1997**.
 70. C. Kittel, *Introduction to Solid State Physics*, 6th ed., John Wiley & Sons, Inc., New York, **1986**.
 71. R. B. Frankel, B. M. Moskowitz, "Biogenic Magnets," in *Magnetism: Molecules to Materials, Vol. 4* (Eds.: J. S. Miller, M. Drillon), Wiley-VCH Verlag GmbH & Co. KGaA, Weinheim, **2003**, p. 485.
 72. A. H. Morrish, *The Physical Principles of Magnetism*, IEEE Press, New York, **2001**.
 73. D. Jiles, *Introduction to Magnetism and Magnetic Materials*, Chapman and Hall, New York, **1991**.
 74. P. C. Fannin, "Investigating magnetic fluids by means of complex susceptibility measurements," *J. Magn. Magn. Mater.*, *258-259*, 446-451 (2003).
 75. P. J. Goodhew, J. Humphreys, R. Beanland, *Electron Microscopy and Analysis*, 3rd ed., Taylor & Francis, New York, **2001**.
 76. D. B. Williams, C. B. Carter, *Transmission Electron Microscopy: A Textbook for Materials Science, Vol. 1*, Plenum Press, New York, **1996**.
 77. L. Reimer, *Transmission Electron Microscopy: Physics of Image Formation and Microanalysis, Vol. 36*, 4th ed., Springer, New York, **1997**.

78. R. H. Geiss, A. D. Romig, "Introductory Electron Optics," in *Principles of Analytical Electron Microscopy* (Eds.: D. C. Joy, A. D. Romig, J. I. Goldstein), Plenum Press, New York, **1986**, pp. 29-76.
79. D. B. Williams, C. B. Carter, *Transmission Electron Microscopy: A Textbook for Materials Science, Vol. 3*, Plenum Press, New York, **1996**.
80. P. Buseck, J. Cowley, L. Eyring, "High-Resolution Transmission Electron Microscopy and Associated Techniques," Oxford University Press, New York, **1988**, p. 645.
81. J. C. H. Spence, *Experimental High-Resolution Electron Microscopy*, Oxford University Press, New York, **1981**.
82. Z. L. Wang, *Elastic and Inelastic Scattering in Electron Diffraction and Imaging*, Plenum Press, New York, **1995**.
83. D. B. Williams, C. B. Carter, *Transmission Electron Microscopy: A Textbook for Materials Science, Vol. 4*, Plenum Press, New York, **1996**.
84. D. Shindo, T. Oikawa, *Analytical Electron Microscopy for Materials Science*, Springer, New York, **2002**.
85. J. W. Edington, *Electron Diffraction in the Electron Microscope, Vol. 2*, The Macmillan Press Ltd., New York, **1975**.
86. D. B. Williams, C. B. Carter, *Transmission Electron Microscopy: A Textbook for Materials Science, Vol. 2*, Plenum Press, New York, **1996**.
87. M. Saunders, in *CBED: Introduction and Theory*, The University of Western Australia; Center for Microscopy and Microanalysis, Perth, WA, **2003**.
88. J. M. Cowley, *Diffraction Physics*, North Holland Publishing Company, LTD., Oxford, **1975**.
89. J. M. Cowley, "Coherent convergent beam electron diffraction," in *Electron Diffraction Techniques, Vol. 1* (Ed.: J. M. Cowley), Oxford University Press, New York, **1992**.
90. E. W. Nuffield, *X-ray Diffraction Methods*, John Wiley & Sons, Inc., New York, **1966**.
91. "Technical Data of D-500," in *Technical University Muenchen*, http://www1.physik.tu-muenchen.de/lehrstuehle/E21/x_ray_lab/D500/parameters.html, **April 02, 2005**.
92. A. Guinier, *X-ray Diffraction: In Crystals, Imperfect Crystals and Amorphous Bodies*, W. H. Freeman and Company, San Francisco, **1963**.
93. M. G. Castellano, "Macroscopic quantum behavior of superconducting quantum interference devices," *Fortschr. Phys.*, *51*, 288-294 (2003).
94. H. Ibach, H. Luth, *Solid-State Physics: An Introduction to Principles of Materials Science*, 2nd ed., Springer, New York, **1995**.
95. T. VanDuzer, C. W. Turner, *Principles of Superconductive Devices and Circuits*, 2nd ed., Prentice Hall PTR, Upper Saddle River, **1999**.
96. P. D. Allen, T. G. St. Pierre, R. Street, "Interactions in native horse spleen ferritin below the superparamagnetic blocking temperature," *J. Magn. Magn. Mater.*, *177-181*, 1459-1460 (1998).
97. G. Bertotti, *Hysteresis in Magnetism: For Physicists, Materials Scientists and Engineers*, Academic Press, New York, **1998**.
98. E. DellaTorre, *Magnetic Hysteresis*, IEEE Press, New York, **1999**.
99. L. A. Feigin, D. I. Svergun, *Structure Analysis by Small-Angle X-ray and Neutron Scattering*, Plenum Press, New York, **1987**.
100. NIST, *SANS Analysis with Igor Pro*, http://www.ncnr.nist.gov/programs/sans/manuals/data_anal.html, **February 28 2005**.

101. N. Kohler, C. Sun, J. Wang, G. Fryxell, M. Zhang, in *Fifth International Conference on the Scientific and Clinical Applications of Magnetic Carriers*, The Cleveland Clinic Foundation, Lyon, France, **2004**, p. 32.
102. A. D. Ebner, A. L. Stanley, M. D. Kaminski, A. J. Rosengart, J. A. Ritter, in *Fifth International Conference on the Scientific and Clinical Applications of Magnetic Carriers*, The Cleveland Clinic Foundation, Lyon, France, **2004**, p. 39.
103. B. Schopf, T. Neuberger, K. Schulze, A. Petri, M. Chastellain, B. Steitz, M. Hofmann, H. Hofmann, B. v. Rechenberg, in *Fifth International Conference on the Scientific and Clinical Applications of Magnetic Carriers*, The Cleveland Clinic Foundation, Lyon, France, **2004**, p. 26.
104. M. D. Kaminski, A. J. Rosengart, C. J. Mertz, S. G. Guy, Y. Xie, H. Chen, M. R. Finck, V. Balasubramanian, P. L. Caviness, in *Fifth International Conference on the Scientific and Clinical Applications of Magnetic Carriers*, The Cleveland Clinic Foundation, Lyon, France, **2004**, p. 83.
105. A. J. Rosengart, M. D. Kaminski, C. J. Mertz, S. G. Guy, Y. Xie, H. Chen, M. R. Finck, P. L. Caviness, in *Fifth International Conference on the Scientific and Clinical Applications of Magnetic Carriers*, The Cleveland Clinic Foundation, Lyon, France, **2004**, p. 82.
106. C. Plank, U. Schillinger, T. Brill, C. Rudolph, S. Huth, S. Gersting, F. Kroetz, J. Hirschberger, C. Bergemann, in *Fifth International Conference on the Scientific and Clinical Applications of Magnetic Carriers*, The Cleveland Clinic Foundation, Lyon, France, **2004**, p. 43.
107. R. C. Reszka, M. Martens, D. Schueller, in *Fifth International Conference on the Scientific and Clinical Applications of Magnetic Carriers*, The Cleveland Clinic Foundation, Lyon, France, **2004**, p. 44.
108. A. Jordan, in *Fifth International Conference on the Scientific and Clinical Applications of Magnetic Carriers*, The Cleveland Clinic Foundation, Lyon, France, **2004**, p. 45.
109. J. J. Host, J. A. Block, K. Parvin, V. P. Dravid, J. L. Alpers, T. Sezen, R. LaDuca, "Effect of annealing on the structure and magnetic properties of graphite encapsulated nickel and cobalt nanocrystals," *J. Appl. Phys.*, *83*, 793-801 (1998).
110. J. Jiao, S. Seraphin, X. Wang, J. C. Withers, "Preparation and properties of ferromagnetic carbon-coated Fe, Co and Ni nanoparticles," *J. Appl. Phys.*, *80*, 103-108 (1996).
111. M. E. McHenry, S. A. Majetich, J. O. Artman, M. DeGraef, S. W. Staley, "Superparamagnetism in carbon-coated Co particles produced by the Kratschmer carbon arc process," *Phys. Rev. B*, *49*, 11 358-311 363 (1994).
112. C. P. Chen, T. H. Chang, T. F. Wang, "Synthesis of magnetic nano-composite particles," *Ceramics International*, *27*, 925-930 (2001).
113. S. Seraphin, D. Zhou, J. Jiao, "Filling the carbon nanocages," *J. Appl. Phys.*, *80*, 2097-2104 (1996).
114. Y. Saito, M. Masuda, "Crystallographic Structure and Magnetic Properties of Co Fine Particles Encaged in Carbon Nanocapsules," *Jpn. J. Appl. Phys.*, *34*, 5594-5598 (1995).
115. Y. Saito, "Nanoparticles and Filled Nanocapsules," *Carbon*, *33*, 979-988 (1995).
116. P. J. F. Harris, S. C. Tsang, "A simple technique for the synthesis of filled carbon nanoparticles," *Chem. Phys. Lett.*, *293*, 53-58 (1998).
117. S. Tomita, M. Hikita, M. Fujii, S. Hayashi, K. Yamamoto, "A new and simple method for thin graphitic coating of magnetic-metal nanoparticles," *Chem. Phys. Lett.*, *316*, 361-364 (2000).

118. M. Yudasaka, K. Tasaka, R. Kikuchi, Y. Ohki, S. Yoshimura, "Influence of chemical bond of carbon on Ni catalyzed graphitization," *J. Appl. Phys.*, *81*, 7623-7629 (1997).
119. V. V. Baranauskas, M. A. Zalich, M. Saunders, T. G. St. Pierre, J. S. Riffle, "Poly(styrene-*b*-4-vinylphenoxyphthalonitrile)-Cobalt Complexes and their Conversion to Oxidatively-Stable Cobalt Nanoparticles," *Chem. Mater.*, *Submitted* (2004).
120. S. P. Gubin, Y. I. Spichkin, Y. A. Koksharov, G. Y. Yurkov, A. V. Kozinkin, T. I. Nedoseikina, M. S. Korobov, A. M. Tishin, "Magnetic and structural properties of Co nanoparticles in a polymeric matrix," *J. Magn. Magn. Mater.*, *265*, 234-242 (2003).
121. V. F. Puentes, K. M. Krishnan, P. Alivisatos, "Synthesis, self-assembly and magnetic behavior of a two-dimensional superlattice of single-crystal epsilon-Co nanoparticles," *App. Phys. Lett.*, *78*, 2187-2189 (2001).
122. H. C. P. Cobalt, in *JCPDS-International Centre for Diffraction Data*, card 05-0727, **1996**.
123. J. Wang, M. Tian, T. E. Mallouk, M. H. W. Chan, "Microtwinning in Template-Synthesized Single-Crystal Metal Nanowires," *J. Phys. Chem. B*, *108*, 841-845 (2004).
124. C. H. Kiang, M. Endo, P. M. Ajayan, G. Dresselhaus, M. S. Dresselhaus, "Size Effects in Carbon Nanotubes," *Phys. Rev. Lett.*, *81*, 1869-1872 (1998).
125. A. E. Berkowitz, K. Takano, "Exchange anisotropy - a review," *J. Magn. Magn. Mater.*, *200*, 552-570 (1999).
126. M. Kiwi, "Exchange Bias Theory," *J. Magn. Magn. Mater.*, *234*, 584-595 (2001).
127. J. Nogues, I. K. Schuller, "Exchange Bias," *J. Magn. Magn. Mater.*, *192*, 203-232 (1999).
128. J. J. Host, M. H. Teng, B. R. Elliot, J. Hwang, T. O. Mason, D. L. Johnson, V. P. Dravid, "Graphite encapsulated nanocrystals produced using a low carbon:metal ratio," *J. Mater. Res.*, *12*, 1268-1273 (1997).
129. R. M. Bozorth, *Ferromagnetism*, 5th ed., D. Van Nostrand Company, Inc., New York, **1959**.
130. A. K. Boal, "Synthesis and Applications of Magnetic Nanoparticles," in *Nanoparticles: Building Blocks for Nanotechnology* (Ed.: V. Rotello), Kluwer Academic/Plenum Publishers, New York, **2004**.
131. J. Giri, P. Pradhan, N. Tyagi, R. Banerjee, D. Datta, D. Bahadur, in *Fifth International Conference on the Scientific and Clinical Applications of Magnetic Carriers*, The Cleveland Clinic Foundation, Lyon, France, **2004**, p. 55.
132. I. Hilger, W. Andra, R. Hergt, R. Hiergeist, W. A. Kaiser, in *Fifth International Conference on the Scientific and Clinical Applications of Magnetic Carriers*, The Cleveland Clinic Foundation, Lyon, France, **2004**, p. 52.
133. M. L. Vadala, M. Rutnakornpituk, M. A. Zalich, T. G. St. Pierre, J. S. Riffle, "Block copolysiloxanes and their complexation with cobalt nanoparticles," *Polymer*, *45*, 7449-7461 (2004).
134. T. M. Keller, "Oxidative protection of carbon fibers with poly(carborane-siloxane-acetylene)," *Carbon*, *40*, 225-229 (2002).
135. T. Michalet, M. Parlier, F. Beclin, R. Duclos, J. Crampon, "Elaboration of low shrinkage mullite by active filler controlled pyrolysis of siloxanes," *J. Eur. Ceram. Soc.*, *22*, 143-152 (2002).
136. M. Scheffler, R. Bordia, N. Travitzky, P. Greil, "Development of a rapid crosslinking preceramic polymer system," *J. Eur. Ceram. Soc.*, *25*, 175-180 (2005).

137. L. G. Jacobsohn, M. E. Hawley, D. W. Cooke, M. F. Hundley, J. D. Thompson, R. K. Schulze, M. Nastasi, "Synthesis of cobalt nanoparticles by ion implantation and effects of postimplantation annealing," *J. Appl. Phys.*, *96*, 4444-4450 (2004).
138. M. L. Vadala, M. A. Zalich, D. B. Fulks, T. G. St.Pierre, J. P. Dailey, J. S. Riffle, "Cobalt-Silica Magnetic Nanoparticles with Functional Surfaces," *J. Magn. Magn. Mater.*, *submitted* (2004).
139. J. Happel, H. Brenner, *Low Reynolds number hydrodynamics*, Prentice-Hall, Inc., New Jersey, **1965**.
140. P. D. Allen, T. G. St.Pierre, R. Street, "Magnetic interactions in native horse spleen ferritin below the superparamagnetic blocking temperature," *J. Magn. Magn. Mater.*, *177-181*, 1459-1460 (1998).
141. P. Aranda, Y. Mosqueda, E. Perez-Cappe, E. Ruiz-Hitzky, "Electrical characterization of Poly(ethylene oxide)-clay nanocomposites prepared by microwave irradiation," *J. Polym. Sci. Part B: Polym. Phys.*, *41*, 3249-3263 (2003).
142. K. Ratanarat, M. Nithitanakul, D. C. Martin, R. Magaraphan, "Polymer-layer silicate nanocomposites: linear PEO and highly branched dendrimer for organic wastewater treatment," *Rev. Adv. Mater. Sci.*, *5*, 187-192 (2003).
143. H. Y. Zhu, J. D. Riches, J. C. Barry, "Alumina nanofibers prepared from aluminum hydrate with poly(ethylene oxide) surfactant," *Chem. Mater.*, *14*, 2086-2093 (2002).
144. T. Tanji, T. Hirayama, "Differential Microscopy in Off-Axis Transmission Electron Microscope Holography," *Scanning Microscopy*, *11*, 417-425 (1997).
145. R. E. Dunin-Borkowski, M. R. McCartney, B. Kardynal, D. J. Smith, "Magnetic interactions within patterned cobalt nanostructures using off-axis electron holography," *J. Appl. Phys.*, *84*, 374-378 (1998).

VITAE

Michael Andrew Zalich grew up in Latrobe, Pennsylvania where he attended St. Vincent College and received his Bachelor's Degree in Chemistry-Environmental Science with High Honors in 1997. After college, Michael was employed by PPG Industries, at the Coatings and Resins Research and Engineering Facility in Allison Park, Pennsylvania, where he was a formulation chemist and technical liaison for waterborne primer technology between Allison Park and Ingersheim, Germany. Motivated by an interest in research, Michael left PPG to pursue a Ph. D. in polymer chemistry at Virginia Polytechnic Institute and State University in Blacksburg, Virginia. While at Virginia Tech, Michael worked under the supervision of Dr. Judy Riffle to prepare biodegradable polymeric microspheres loaded with stabilized magnetic nanoparticles. In 2003, Michael was awarded a Fulbright Post-Baccalaureate Fellowship to conduct research at the University of Western Australia (UWA) under the co-supervision of Dr. Judy Riffle (professor of chemistry at Virginia Tech) and Dr. Tim St. Pierre (Associate Professor of physics at the University of Western Australia). During his tenure at UWA (August 2003 – March 2005), Michael worked closely with Dr. St. Pierre of the Biophysics group and Dr. Martin Saunders from the Center for Microscopy and Microanalysis to study the structural and magnetic properties of macromolecule-metal and macromolecule-metal oxide nanoparticles. Upon his return to Virginia Tech, Michael successfully defended his Ph.D. on April 29, 2005.